

# Sterile neutrinos as a dark matter candidate

Signe Riemer-Sørensen

signe@dark-cosmology.dk

*Dark Cosmology Centre*

August 25, 2006



Master Thesis in Physics

*Niels Bohr Institute*

Supervised by:

Kristian Pedersen  
*Dark Cosmology Centre*

Steen H. Hansen  
*University of Zurich*



## Contents

<b>1</b>	<b>Basic Cosmology</b>	<b>3</b>
1.1	The Benchmark model . . . . .	3
1.2	Redshift and distances . . . . .	4
1.3	Values of cosmological parameters . . . . .	6
1.4	Dark matter . . . . .	6
1.5	Cold, hot, and warm dark matter . . . . .	7
1.6	The sterile neutrino of cosmology . . . . .	9
<b>2</b>	<b>Theory of Sterile Neutrinos</b>	<b>10</b>
2.1	The standard model of particle physics . . . . .	10
2.2	Standard model neutrino physics . . . . .	11
2.3	Sterile neutrinos of particle physics . . . . .	13
2.4	Two-type neutrino oscillation . . . . .	14
2.5	Radiative decay . . . . .	15
2.6	Constraining the decay rate from the emitted photons . . . . .	16
2.7	Is the flux measurable . . . . .	17
<b>3</b>	<b>The Early Universe</b>	<b>18</b>
3.1	The distribution function . . . . .	18
3.2	The Boltzmann equation . . . . .	20
3.3	The simple physical approximation . . . . .	21
3.4	Integration of the Boltzmann equation . . . . .	22
3.5	Analytical collision integral . . . . .	24
3.6	Numerical solutions of the Boltzmann equation . . . . .	25
<b>4</b>	<b>X-ray Observations</b>	<b>27</b>
4.1	X-ray observatories . . . . .	27
4.2	Chandra details . . . . .	28
4.3	Gratings . . . . .	30
<b>5</b>	<b>Analysis of X-ray Data</b>	<b>32</b>
5.1	The raw data . . . . .	32
5.2	CIAO and Sherpa . . . . .	32
5.3	Bad pixels, good time intervals and point source removal . . . . .	33
5.4	Instrumental response . . . . .	34
5.5	Extracting spectra and instrumental response files . . . . .	35
5.6	Background subtraction . . . . .	36
5.7	Determining the flux from spectral model comparison . . . . .	37

<b>6</b>	<b>Where to Look for Decaying Dark Matter</b>	<b>38</b>
6.1	Clusters of galaxies . . . . .	38
6.2	The Milky Way halo . . . . .	38
6.3	Dark matter blobs in clusters of galaxies . . . . .	40
6.4	Improving the resolution . . . . .	40
<b>7</b>	<b>A383, A Cluster of Galaxies</b>	<b>42</b>
7.1	Clusters of galaxies and their properties . . . . .	42
7.2	Why A383 is a good cluster to observe . . . . .	42
7.3	Intra-cluster gas and the $\beta$ -model . . . . .	43
7.4	The NFW-profile . . . . .	44
7.5	Optimising the observational field of view . . . . .	45
7.6	The optimised field of view for A383 . . . . .	47
7.7	Uncertainty in optimal radius and mass of the annulus . . . . .	48
7.8	Remark: Comparison to a modified $\beta$ -model . . . . .	49
7.9	Extracting spectrum of A383 . . . . .	49
<b>8</b>	<b>The Milky Way Dark Matter Halo</b>	<b>51</b>
8.1	Blank sky data . . . . .	51
8.2	Observed halo mass and mean distance . . . . .	52
<b>9</b>	<b>The Dark Matter Blob of A520</b>	<b>54</b>
9.1	Extracting the spectrum of A520 . . . . .	54
9.2	The mass of the blob . . . . .	55
<b>10</b>	<b>Grating Spectrum of A1835</b>	<b>57</b>
10.1	The advantages of A1835 . . . . .	57
10.2	Data treatment of A1835 . . . . .	58
10.3	The zero order spectrum . . . . .	59
<b>11</b>	<b>X-Ray Constraints on Sterile Neutrinos</b>	<b>60</b>
11.1	Distinguishing between emission lines and spectral features . . . . .	60
11.2	A conservative upper mass limit from the total flux . . . . .	61
11.3	Determining the emission line flux . . . . .	62
11.4	A more model dependent limit on the flux . . . . .	63
11.5	Constraining the decay rate of a dark matter particle . . . . .	66
11.6	Lifetime constraints and model confrontation . . . . .	68
11.7	Constraining S . . . . .	70
11.8	The $\sin^2(2\theta) - m_s$ parameter space . . . . .	70
11.9	Improving the results . . . . .	71

<b>12 Comparison to Other Constraints</b>	<b>73</b>
12.1 The Tremaine-Gunn bound . . . . .	73
12.2 Diffuse X-ray background . . . . .	73
12.3 The Lyman- $\alpha$ forest . . . . .	75
12.4 All constraints . . . . .	77
12.5 Pulsar kicks and early star synthesizing . . . . .	78
<b>13 Other Dark Matter Candidates</b>	<b>79</b>
13.1 Higgs-like bosons and axions . . . . .	79
13.2 Super-symmetric particles . . . . .	79
<b>14 Summary</b>	<b>80</b>
<b>A Appendix</b>	<b>i</b>
A.1 Abbreviations and Acronyms . . . . .	i
A.2 Rewriting the Boltzmann equation . . . . .	iii
A.3 Sterile neutrinos in the Milky Way: Observational constraints . . . . .	iv



## Introduction

The mass of the visible stars and gas in the Universe is not enough to explain the observed gravitational effects. The missing non-luminous matter is called dark matter and there are many candidates, among which the sterile neutrinos belong to the better ones. Originally the sterile neutrinos were proposed as a dark matter candidate to solve the structure formation problems of the cold dark matter scenario predicting an over abundance of small structures, such as dwarf galaxies, in the Universe. It is a warm dark matter particle with a mass in the keV-range, which apart from being a dark matter candidate also has provided solutions to other problems: the masses of the active neutrinos, the baryon asymmetry of the Universe, observed peculiar velocities of pulsars, synthesizing the early star formation, reionisation, etc. Sterile, or non-weakly interacting right handed neutrinos, are a natural part of a minimally extended standard model of particle physics. If the active neutrinos have a non-zero mass, as indicated by several atmospheric and solar neutrino oscillation experiments, the sterile neutrinos will take part in the neutrino oscillations, which allow for a radiative decay under emission of an X-ray photon with energy of half the sterile neutrino mass. This renders it a testable dark matter candidate. The probability of a decay is related to the amount of oscillation with the active neutrinos, which is described by the mixing angle.

*Chandra* X-ray spectra of the flux received from dark matter dense regions such as the outskirts of galaxy clusters and the halo of the Milky Way can be used in a search for sterile neutrinos as dark matter. From these spectra the decay rate of any dark matter particle with a radiative decay in X-ray can be constrained. By comparison with theoretical models for sterile neutrinos more specific constraints on the lifetime, mass and mixing angle of sterile neutrinos and a possible additional entropy release after the production of the sterile neutrinos can be determined.

The structure of this report is as follows: In Sec. 1 a short introduction is given to basic cosmology and its notation together with an introduction to the problem of missing non-luminous gravitational sources called dark matter. In Sec. 2 the standard model of particle physics is explained with focus on the neutrino sector in order to present the sterile neutrino in the context of particle physics. To be able to constrain the sterile neutrino we need to know how it behaved in the early Universe which is the purpose of Sec. 3. At this point the theoretical stage is set, and we are ready to look at X-ray observations in Sec. 4 and X-ray data analysis in Sec. 5. Then in Sec. 6 several possibilities of where to point our X-ray telescopes are considered to get the best view of the dark matter in order to find or constrain the sterile neutrinos. The next four sections, Sec. 7 to Sec. 10, are a presentation of the obtained spectra of the regions selected in Sec. 6. The resulting constraints are presented in Sec. 11 and compared to other constraints on the sterile neutrinos in Sec. 12. Just before the end a short comment on the future of sterile neutrinos and

other dark matter candidates is given in Sec. 13. Finally the report is concluded by a short summary in Sec. 14.

In the technical language of X-ray observations abbreviations and acronyms are extensively used. They are explained when introduced, and can furthermore be found in App. A.1.

A part of this work has been published in [1] which can be found in App. A.3.

Throughout the report I have used natural units where  $c = \hbar = k_B = 1$ . They are all universal constants, i. e. they have the same value in all reference systems. In the natural units velocity is not given in  $m/sec$  but as a fraction of  $c$ . This means that velocity becomes a pure number, momentum, mass and temperature all take the unit of energy, and length has the same unit inverted [2].

This report constitutes my masters thesis and I would like to thank everybody at the Dark Cosmology Centre and especially my supervisors Kristian Pedersen and Steen H. Hansen for letting me do a very interesting and instructive project in the overlapping fields of particle physics and cosmology.

Signe Riemer-Sørensen, Copenhagen, June 23, 2006

# 1 Basic Cosmology

Cosmology is the description of the Universe on a large scale. This section contains a short introduction to the standard model of cosmology and its most important parameters<sup>1</sup>. The notations of redshift and distance measurements are presented for later use before the concept of dark matter and the challenges to be solved by a dark matter candidate are introduced.

## 1.1 The Benchmark model

The Benchmark model is the “standard Big Bang model of cosmology” where the Universe is assumed to be nearly flat and at the present time dominated by a cosmological constant (also called dark energy) which is responsible for the accelerating expansion of the Universe. The acceleration was concluded from super nova observations in 1998 [3].

The Universe is described in space-time coordinates  $(t, r, \theta, \phi)$  and the shortest distance between two points, called a geodesic, is given by the Robertson–Walker metric, which has the properties that the Universe is spatially homogeneous and isotropic at all times and distances are allowed to expand (or contract) as a function of time [4]:

$$ds^2 = dt^2 - a^2(t) \left[ \frac{dr^2}{1 - kr^2} + r^2(d\theta + \sin^2(\theta)d\phi) \right]. \quad (1)$$

$k = 0, \pm 1$  determines the curvature of the Universe. The Universe can either be positively curved ( $k = +1$ ), which in two dimensions would correspond to the surface of a sphere, or it can be negatively curved ( $k = -1$ ) corresponding to the “seat” of a saddle. For a flat Universe,  $k$  is equal to zero, and the two dimensional analogy is a plane.  $a(t)$  is the scale factor that independent of location tells us how the expansion of the Universe depends on time. The spatial coordinates  $(r, \theta, \phi)$  are called co-moving coordinates and can be regarded as the non-changing coordinates in a coordinate system that expands with the scale factor,  $a(t)$ . The isotropy and homogeneity on large scales ( $\approx 100$  Mpc) are observational facts from large scale structure surveys.

The time evolution of the Universe is described by two independent key equations. The first one is the Friedmann equation that can be derived from the Robertson–Walker metric [4]:

$$H^2(t) = \frac{\dot{a}(t)}{a(t)} = \frac{8\pi G\rho(t)}{3} - \frac{\kappa}{R_0 a^2(t)}. \quad (2)$$

---

<sup>1</sup>An extended introduction to cosmology can be found in [4] or [5].

$H(t) = \dot{a}(t)/a(t)$  is called the Hubble parameter and specifies the expansion velocity of the Universe. At the present time it is usually given in units of  $h$  defined as  $h = H_0/(100 \text{ km/sec/Mpc})$ .  $\rho_0$  is the energy density at the present time and  $\kappa$  determines the sign of the curvature of the Universe with a present time radius of curvature given by  $R_0$ . The density parameter is defined as  $\Omega(t) = \rho(t)/\rho_c$  where  $\rho_c = (3H^2(t))/(8\pi G)$  is the critical energy density needed for the Universe to be flat. With  $\Omega(t)$  the Friedmann equation can then be rewritten as:

$$1 = \Omega(t) - \frac{\kappa}{R_0^2 a^2(t) H^2(t)}, \quad (3)$$

where it is seen that for a flat Universe, as in the Benchmark model ( $\kappa = 0$ ), the last term disappears and  $\Omega(t) = 1$ . The flatness of the Universe is given by observations (Sec. 1.3). The Universe consist of three components of importance: radiation, matter and a cosmological constant. They are assumed not to be in thermal equilibrium (since shortly after Big Bang) and therefore they evolve independently and  $\Omega(t)$  becomes a sum over the  $\Omega$ s of the different components.

The second key equation is the fluid equation which corresponds to the first law of thermodynamics for an expanding universe [4]:

$$\dot{\rho}(t) + 3\frac{\dot{a}(t)}{a(t)}(\rho(t) + P) = 0 \quad (4)$$

where  $P$  is the pressure. It is given by  $P = \omega\rho$ , where  $\omega$  is a dimensionless number which takes the values  $\omega \approx 0$  for non-relativistic matter,  $\omega = 1/3$  for relativistic matter including radiation and  $\omega < -1/3$  for a cosmological constant. The Friedmann equation (Eqn. 2), the fluid equation (Eqn. 4) and  $P = \omega\rho$  can be combined to give:

$$\frac{\ddot{a}(t)}{a(t)} = -\frac{4\pi G}{3}\rho(t)(1 + \omega). \quad (5)$$

We see that the time evolution of the scale factor depends on the value of  $\omega$  and therefore on the dominating component of the Universe at a given time. The very early Universe was radiation dominated ( $a(t) \propto t^{1/2}$ ), then matter took over ( $a(t) \propto t^{2/3}$ ), and at the present time it seems like a cosmological constant is taking over ( $a(t) \propto e^{Ht}$ ) [4]. The  $t$ -dependence of  $a(t)$  is shown in Fig. 1.

## 1.2 Redshift and distances

A direct consequence of the Hubble expansion is the cosmological redshift of observed photons. A local observer observing a distant light source will see a redshift of the wavelength,  $\lambda_{obs}$ , compared to that of the emitted light,  $\lambda_{em}$  [4]:

$$z = \frac{\lambda_{obs} - \lambda_{em}}{\lambda_{em}}. \quad (6)$$

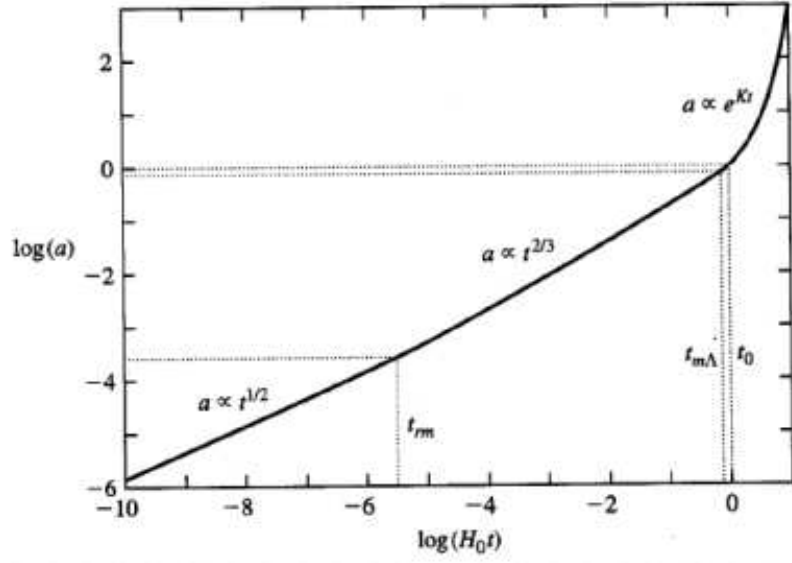


**Figure 1:**  $a(t)$  depends differently on  $t$  depending on the component dominating the Universe. The early Universe was radiation dominated, then matter took over, and finally the Universe is dominated by a cosmological constant [4].

The definition of the scale factor gives a useful relation between redshift and scale factor for small peculiar velocities [4]:

$$z + 1 = \frac{a(t_{obs})}{a(t_{em})}, \quad (7)$$

which in the near universe, where the expansion is taken to be linear, reduces to Hubbles law for proper distances,  $r$  [4]:

$$z = H_0 r. \quad (8)$$

Unfortunately the expansion of the Universe makes it impossible to measure the proper distance to a cosmological object in practice. One thing we can measure instead is the flux,  $F$ , i. e. the energy emitted per area per time from a given source. If the luminosity (the total energy emitted per time) of a celestial object is known, the measured flux can be used to define a distance, called the “luminosity distance” [4]:

$$D_L = \left( \frac{L}{4\pi F} \right)^{1/2}. \quad (9)$$

In a static Euclidean Universe the flux received from a source at a given proper distance,  $r$ , is  $F = L/(4\pi r^2)$  so the luminosity distance is equal to the proper

distance,  $D_L = r$ . For a flat Universe described by the Robertson–Walker metric (Eqn. 1), the relation becomes [4]:

$$D_L = r(1 + z). \quad (10)$$

The problem is that we need to know the total luminosity of at least one celestial object in order to calibrate the method (and we would still have a problem with extinction in dust etc.). With the Robertson–Walker metric for a flat Universe, the angular extension of an object of proper length,  $l$ , is given by [4]:

$$\Delta\theta = \frac{l(1 + z)^2}{D_L}. \quad (11)$$

For very distant objects, the redshift is usually given as a measure of distance to avoid the problems of determining proper distances.

### 1.3 Values of cosmological parameters

The values of the cosmological parameters in the Friedmann equation (Eqn. 2), can be determined from different observations. In Fig. 2 is shown the constraints on the values of the matter density,  $\Omega_M$ , and the density of the cosmological constant,  $\Omega_\Lambda$ , at the present time, determined from observations of super novae, the Cosmic Microwave Background (CMB) from the satellite observatory WMAP, and from clusters of galaxies.

The best fitting present day values from the combined data sets are [6]:  $\Omega_{tot} = 1.00 \pm 0.02$  giving a flat universe,  $\Omega_M = 0.26 \pm 0.03$ ,  $\Omega_\Lambda = 0.76 \pm 0.03$ , and  $h = 0.73 \pm 0.03$ . These values have been used throughout the report except for  $h$  where all earlier results are based on an older value of  $h = 0.71$  which I have kept in order to make the results directly comparable.

### 1.4 Dark matter

The amount of visible matter in the Universe is not enough for the Universe to be flat as observed from the CMB [7]. It turns out that of the matter density of  $\Omega_M = 0.26$  only about one tenth is in the form of stars, dust, gas, etc. i. e. in the form we call baryonic matter [6]. The rest does not emit light but is only observed through its gravitational effects and is therefore called dark matter. In the 1930's the astronomer, Fritz Zwicky, studied the velocity dispersion as a function of radius of the Coma Cluster of galaxies shown in the right part of Fig. 3. What he found was that the dispersion of radial velocities was very large - around 1000 km/sec. The mass of the visible stars and gas inside the cluster does not provide a gravitational potential large enough to hold together a cluster with such

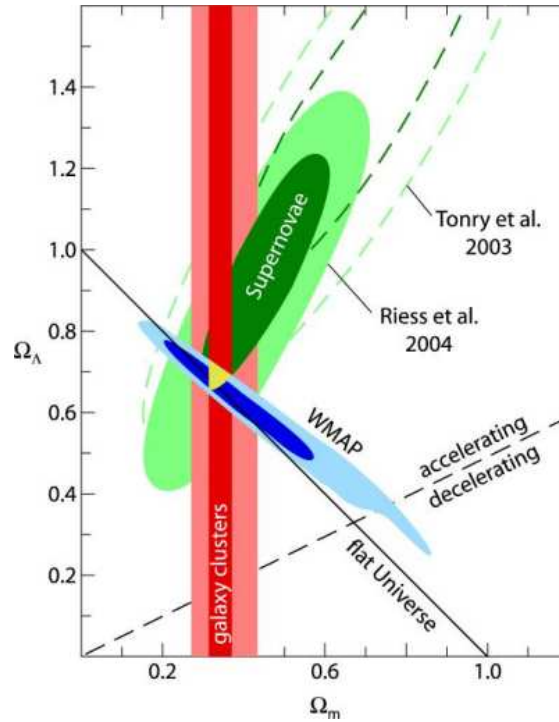


**Figure 2:** The constraints on the values of  $\Omega_M$  and  $\Omega_\Lambda$  at the present time. The constraints are determined from observations of super novae, the CMB from the satellite observatory WMAP, and from clusters of galaxies [7].

velocity dispersions, so he came to the conclusion that the cluster must contain a lot of “dunkle Materie” later translated to “Dark Matter.” Today we know that clusters are dominated by dark matter and therefore they are matter dominated and their formation and evolution are driven by gravity [8]. The rotation curves of spiral galaxies do also indicate the presence of a galactic dark matter halo.

No one knows what the dark matter is and there are many proposed candidates, mostly in the form of exotic new types of particles. There could also be more than one type of particle contributing to the dark matter, but unless otherwise stated I have assumed all of the dark matter to be one particle specie with a present day density of  $\Omega_{DM} = 0.26$ .

## 1.5 Cold, hot, and warm dark matter

The Universe was matter-dominated at the time when structures formed. As dark matter is the dominant matter component a dark matter particle would have printed its signature in the structures observed today. There are several scenarios for different energy scales of the dark matter particle.

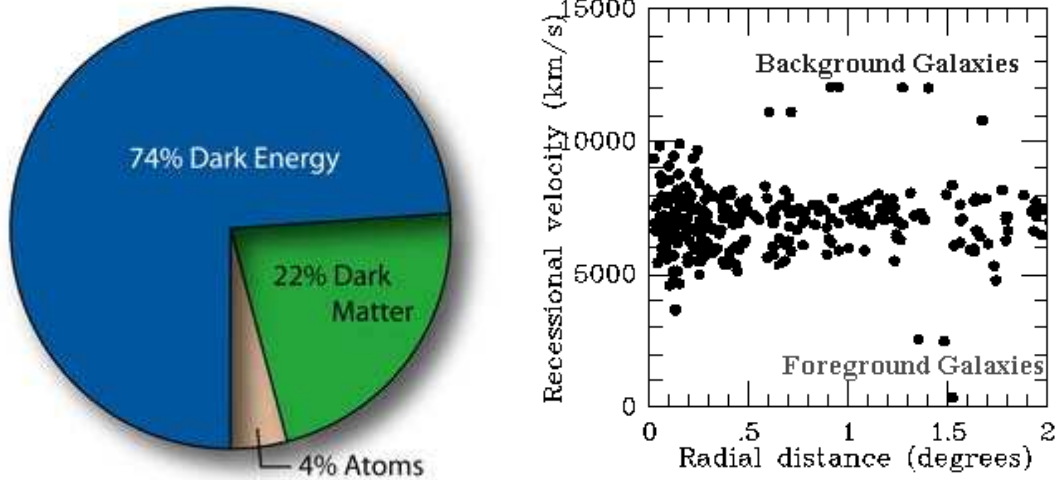


**Figure 3:** *Left:* The energy distribution of the Universe with  $\approx 70\%$  in the form of dark energy (given by a cosmological constant),  $\approx 26\%$  in the form of dark matter, and only  $\approx 4\%$  in the form of ordinary (baryonic) matter as we see it on the Earth [7]. *Right:* The velocity dispersions of the Coma cluster galaxies is of the order of 1000 km/sec [9].

The classical dark matter scenario is one with a cold dark matter particle (CDM). Cold means the particles were non-relativistic ( $T^2 \approx E^2 \ll m^2$ ) at the time when the expansion rate of the Universe became larger than the interaction rate (production and annihilation) called the time of decoupling. The particles interacted and started to form clustering at small scales (stars and galaxies), which later combined to form larger structures (galaxies and clusters). However there are several problems with this “bottom-up” CDM scenario. One problem is that numerical simulations of the structure formation based on simple physical interactions of CDM particles predicts an over-abundance of small halos, e. g. dwarf galaxies, near a Milky Way-like halo [10]. In the case of the Milky Way around 500 sub-halos are predicted by simulations but only of the order of 10 dwarf galaxies have been found [11]. Either there is something wrong with the observations or the physics applied by the model, or more likely, there is something wrong with the model. Another problem is that the density profile of galaxies and clusters of galaxies predicted by the simulations increase the density monotonically towards the centre of the halo and thereby leading to a cuspy density profile which has not yet been observationally verified [12].

An alternative possibility is a hot dark matter particle (HDM) which was relativistic ( $T^2 \approx E^2 \gg m^2$ ) at the time of decoupling. HDM particles moving freely in all directions with velocities close to the speed of light tends to wipe out density fluctuations. Therefore structures on scales below a characteristic length

are erased, so at the time when the particles become non-relativistic, there are no structures at small scales. Instead the structure formation will be “top-down” with the larger structures (galaxies and clusters) forming first and then the smaller structures (stars and galaxies) forming inside the larger structures. In the HDM scenario there will be very little structure on small scales which does not correspond very well with the observations of galaxies, halos, etc. as seen in the Hubble Space Telescope image in Fig. 4.

Between the bottom-up scenario of CDM and the HDM top-down scenario lies the intermediate region of a warm dark matter particle (WDM) with dark matter particles of a typical rest mass of the order of  $\approx 1$  keV, which allows for both small and large scale structures and the right amount of sub-halos [11].



*Figure 4:* The Hubble Deep Field images show a lot of structures in the Universe [13].

## 1.6 The sterile neutrino of cosmology

The sterile neutrino was originally proposed as a dark matter candidate by Dodelson and Widrow in 1993 [14] to solve the discrepancies between the CDM predicted structure formation and observations. It is a WDM dark matter candidate, with a mass in the keV-range and its interactions are dominated by gravity, as preferred by the structure formation [11]. In Sec. 2 it is discussed how the sterile neutrinos are highly motivated by particle physics, but as they are invented as a dark matter candidate, they cannot be constrained very much from particle physics.

Apart from being a dark matter candidate other uses have also been found for the sterile neutrinos e. g. as an explanation for the peculiar velocities of pulsars by allowing for asymmetric neutrino emission [15, 16], for synthesizing early star formation [17], and as an explanation for the fact that we have more baryons than anti-baryons in the Universe [18].

## 2 Theory of Sterile Neutrinos

The sterile neutrinos can be highly motivated by particle physics. In this section the standard model of particle physics is introduced with the focus on the neutrino sector leading to a presentation of the sterile neutrinos and their characteristics. The section is concluded by some remarks on possible decay signatures of the sterile neutrinos.

### 2.1 The standard model of particle physics

Developed primarily in the 1960's the standard model is a group-theoretical extension of quantum mechanics derived from fundamental symmetries found in nature. Basically the standard model describes the elementary particles and the forces between these particles. The elementary particles summarized in Tab. 1 are split into two categories: quarks and leptons. Both categories are again split into three generations shown experimentally at the now closed LEP-experiment (Large Electron Positron Collider) at CERN [19]. For the leptons the three generations are composed of an electron-like particle and its corresponding neutrino:  $(e, \nu_e)$ ,  $(\mu, \nu_\mu)$ , and  $(\tau, \nu_\tau)$ .

Quarks (spin 1/2)			Leptons (spin 1/2)		
Particle	Mass	Charge	Particle	Mass	Charge
up(u)	$3 \cdot 10^3$	2/3	electron (e)	511	-1
down(d)	$6 \cdot 10^3$	-1/3	e-neutrino( $\nu_e$ )	$< 3 \cdot 10^{-2}$	0
charm(c)	1.3	2/3	muon ( $\mu$ )	$1.06 \cdot 10^5$	-1
strange(s)	$1 \cdot 10^5$	-1/3	$\mu$ -neutrino ( $\nu_\mu$ )	< 200	0
top(t)	$1.75 \cdot 10^8$	2/3	tau ( $\tau$ )	$1.7771 \cdot 10^6$	-1
bottom(b)	$4.3 \cdot 10^6$	-1/3	$\tau$ -neutrino ( $\nu_\tau$ )	$< 2 \cdot 10^4$	0

**Table 1:** The particles of the standard model. The force carrying particle for gravity, the graviton, has not yet been observed experimentally. The unit of charge is the electron charge and the masses are given in keV [19, 20].

The standard model particles interacts through the four fundamental forces via their proper force carriers: The photon for the electromagnetic interaction, the  $Z^0$  and  $W^\pm$  bosons for the weak interaction, the eight gluons for the strong interaction and perhaps a graviton for the gravity. The description of two of these, the electromagnetic and the weak interactions have been unified into the so called electro-weak interaction. So far, the gravity has not yet been mathematically incorporated in the standard model with any success. All the particles in the standard model have antiparticles associated with them, except for the photon which is its own anti-particle. These antiparticles have the same mass and spin as

their counterparts, but all other quantum numbers are reversed. All the particles of the standard model are summarized in Fig. 5.

Matter, in the form that we know it, consists of protons and neutrons which again are made of three quarks (two up and a down quark for the proton and two down and an up quark for the neutron) together with a number of gluons. All particles composed of three quarks are called baryons and the fact that we observe more matter than anti-matter in the Universe is called baryon asymmetry. Particles composed of two quarks (a quark and anti-quark) are called mesons.

On top of all this comes the Higgs boson which provide the link between the quantum field description of the particles and their masses [21]. Its existence has not yet been experimentally verified, but one of the purposes of the upcoming Large Hadron Collider (LHC) at CERN is to look for the Higgs boson. The standard model does not predict any masses for the neutrinos but there are compelling experimental evidence for flavour neutrino oscillations (described in Sec. 2.2) which requires the neutrinos to have non-zero masses and implies particle physics beyond the standard model [22]. Another problem with the standard model is that it does not provide any good candidates for the dark matter and the cosmological constant (dark energy). The cosmological constant has been proposed to be some kind of vacuum energy, but so far no one has been able to come up with the right order of magnitude from a standard model vacuum energy.

## 2.2 Standard model neutrino physics

The number of neutrinos in the standard model is known experimentally from LEP where the decay width of the Z-boson was analysed. The conclusion was that there exist  $N_\nu = 2.994 \pm 0.012$  neutrinos that are sensitive only to weak interactions [19]. They are called flavour eigenstates or active neutrinos,  $\nu_e$ ,  $\nu_\mu$ ,  $\nu_\tau$ , and are linear combinations of states with definitive mass,  $\nu_i$ , where  $i$  is the number of the massive neutrinos, which in the standard model is taken to be equal to the number of flavour eigenstates i. e.  $i = 3$ . The non-standard model phenomenon of the difference between flavour and eigenstates is called neutrino oscillations.

In a three-neutrino scenario flavour and mass eigenstates are related by a  $3 \times 3$  mixing matrix called  $U$  which can be parametrized by three mixing angles and a phase describing the experimentally verified non-conservation of charge and parity in weak interactions (CP-violation). So in total there are seven mixing parameters (if we include the three neutrino masses) to be determined experimentally. One way is through the neutrino oscillation experiments, where the (dis)appearance of a given type of neutrinos in a pure one-type neutrino beam is measured. Unfortunately the oscillation experiments are not sensitive to the absolute mass scale but only to the differences of squared neutrino masses  $\Delta m_{21} = m_2^2 - m_1^2$  (solar neutrinos),  $|\Delta m_{31}| = m_3^2 - m_1^2$  (atmospheric neutrinos). The absolute mass scale can

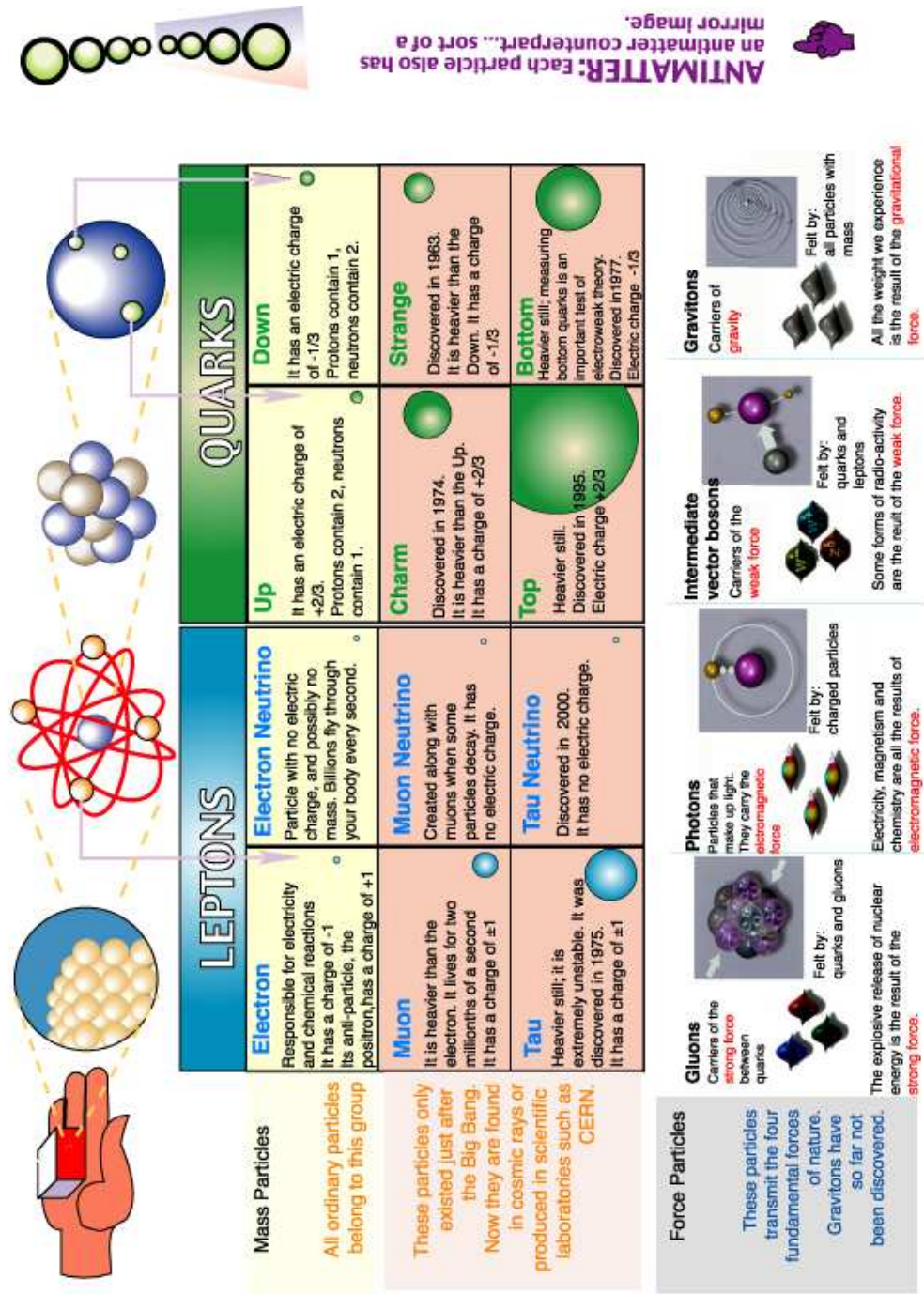


Figure 5: The standard model of particle physics [23].

however be constrained otherwise e. g. through measurements of the time-of-flight dispersion of super novae to be  $\Sigma_i m_i \lesssim 6 \text{ eV}$  [22].

### 2.3 Sterile neutrinos of particle physics

Of all the particles in the standard model, the neutrinos are some of the least understood and the least theoretically incorporated. In the standard model, all of the leptons are said to be Dirac particles and, except for the neutrinos, they all have two polarisation states. We say that they exist as left-handed and right-handed. The neutrinos are different because when measured from weak interaction experiments, they are always left-handed and the anti-neutrinos are always right-handed. This effect is called parity violation<sup>2</sup> [21]. If the neutrinos are pure Dirac particles, there should also exist right-handed neutrinos (and their left-handed anti-neutrinos). They are called sterile neutrinos, as they do not participate in any standard model electro-weak interactions (they are singlets of the  $SU(2)_L \times U(1)_\gamma$  gauge group) [2]. Also the right-handed eigenstates are “shiftet” from their mass eigenstates, so the total number of mass eigenstates accesible by neutrino oscillations is larger than the number of active flavour eigenstates.

The neutrinos can also be of another type called Majorana particles, which by definition are their own anti-particles. If the neutrinos are pure Majorana particles they can be described as entirely left-handed, but then the lepton number conservation in electro-weak interactions involving neutrinos is violated. It is very difficult to distinguish experimentally between the two types of particles. To make it even more complicated there is also the possibility that the neutrinos are a mixture between Dirac and Majorana particles achieving characteristics from both types.

As mentioned in Sec. 2.1 the standard model does not predict any masses for the active neutrinos, but the masses are required by the experimentally verified neutrino oscillations. A simple way to incorporate the neutrino masses is to extend the model with the right-handed neutrinos (as a mixture of Dirac and Majorana particles) just as for the other leptons. It is possible to add an arbitrary number of sterile neutrinos, but at least three sterile neutrinos are needed to explain the neutrino oscillations, the baryon asymmetry, and the dark matter [18]. Interestingly this is the same number as the number of leptonic families. The successful “three sterile neutrino extension” of the standard model is called the  $\nu$ MSM (neutrino Minimal Standard Model) [18, 24, 25, 26, 27, 28]. It is renormalisable and in agreement with most particle physics experiments [18]. In the  $\nu$ MSM the lightest of the sterile neutrinos plays the role as the dark matter.

---

<sup>2</sup>Parity means “mirror image”.

## 2.4 Two-type neutrino oscillation

How is it possible to measure a sterile neutrino that does not interact at all? The answer lies in the neutrino oscillations. Two-type neutrino oscillation is a good approximation to the active-sterile neutrino oscillation because it will be dominated by mixing with only one type of the active neutrinos since the mass-eigenstates of the neutrinos are not fully degenerate (the active neutrinos have different masses) [22]. In the following a short introduction to two-type neutrino oscillation is given which of course can be generalized to three or more types of neutrinos<sup>3</sup>.

With two types of neutrinos, here chosen as an active and a sterile neutrino (without loss of generality), the neutrino mixing can be described with only one mixing angle in vacuum,  $\theta$  [29]:

$$\begin{pmatrix} \nu_\alpha \\ \nu_s \end{pmatrix} = \begin{pmatrix} \cos(\theta) & \sin(\theta) \\ -\sin(\theta) & \cos(\theta) \end{pmatrix} \begin{pmatrix} \nu_1 \\ \nu_2 \end{pmatrix}, \quad (12)$$

where  $\nu_\alpha$  and  $\nu_s$  are flavour eigenstates, and  $\nu_1$  and  $\nu_2$  are a light and a heavy mass eigenstate.  $\theta$  is called the mixing angle and describes the amount of mixing between two states in vacuum. If  $\theta = 0$  there is no mixing and the flavour eigenstates are identical to the mass eigenstates. For the active neutrinos,  $\theta$  is very small, and the flavour eigenstates are almost identical to the mass eigenstates but with a slight shift. If you try to measure the mass of  $\nu_\alpha$  many times by a weak interaction experiment, most of the outcome will be the mass of  $\nu_1$ , but a few times you will get  $\nu_2$  as shown in the left part of Fig. 6. The effective mass of the neutrino is a weighted average. In matter the mixing angle is suppressed by quantum mechanical effects [29].

The phenomenon is called neutrino oscillations, because the probability of measuring a given flavour oscillates with distance (time) and energy [29]:

$$P(\nu_s \rightarrow \nu_\alpha) = \frac{1}{2} \sin^2(2\theta) \left( 1 - \cos\left(\frac{L \cdot \Delta m^2}{2E_\nu}\right) \right), \quad (13)$$

where  $L$  is the propagated length,  $E_\nu$  is the neutrino energy and  $\Delta m^2$  is the difference of the masses squared. The probability of detecting an  $\bar{\nu}_e$  in an originally pure  $\bar{\nu}_\mu$  beam as a function of distance is shown in the right part of Fig. 6. Often the expression “mixing angle” denotes  $\sin^2(2\theta)$ .

By regarding all decay branches possible through oscillations, the mean lifetime of a sterile Dirac neutrino of mass,  $m_s$ , has been determined to be [30, 31]:

$$\tau = \frac{1}{\Gamma_{tot}} = \frac{f(m_s) \cdot 10^{20}}{(m_s/\text{keV})^5 \sin^2(2\theta)} \text{sec}^{-1}, \quad (14)$$

---

<sup>3</sup>A deeper treatment can be found in the literature e.g. [29].

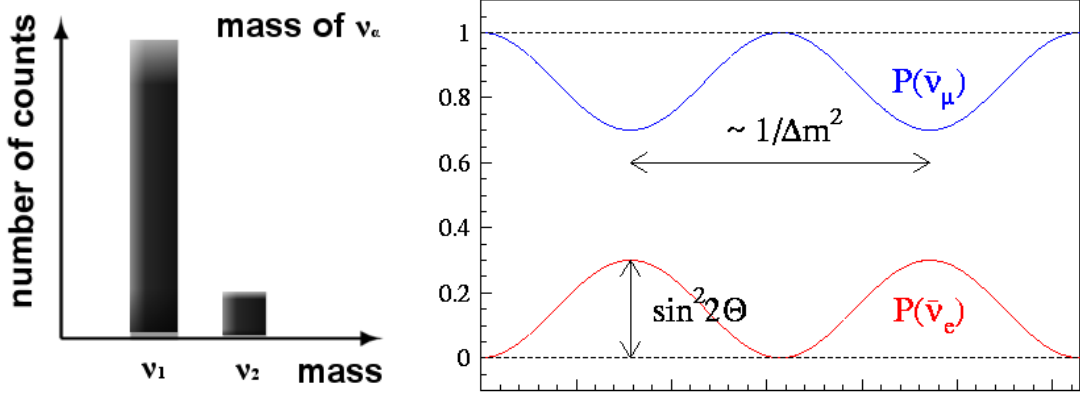


**Figure 6:** *Left:* An interaction dependent measurement of the mass of  $\nu_\alpha$  in a two-type mixing scenario, with mass eigenstates  $\nu_1$  and  $\nu_2$ . *Right:* The probability of detecting an  $\bar{\nu}_e$  in an originally pure  $\bar{\nu}_\mu$  beam as a function of distance.

where  $\Gamma_{tot}$  is the total decay rate.  $f(m_s)$  takes into account the open decay channels so that for  $m_s < 1$  MeV, where only the neutrino channel is open,  $f(m_s) = 0.86$ , but for  $m_s > 2m_e \approx 1$  MeV also the  $e^+e^-$ -channel is open and  $f(m_s) = 1$ . Only the case where  $m_s < 1$  MeV ( $f(m_s) = 0.86$ ) has been considered here.

Unless otherwise stated, throughout the report I have assumed the active-sterile neutrino mixing to be a two-type mixing between a Dirac type sterile neutrino and the electron neutrino. If the sterile neutrino is a Majorana particle, it is by definition its own anti-particle and the interaction probability will double and hence its theoretically predicted decay rate is twice as large ( $\Gamma_{\gamma, Majorana} = 2\Gamma_{\gamma, Dirac}$ ). Because of this difference, any constraints derived from the decay rate for a Dirac particles is more conservative than the corresponding constraints derived for a Majorana particle.

## 2.5 Radiative decay

The most dominant decay of the sterile neutrinos is  $\nu_s \rightarrow \nu_\alpha \nu_\alpha \nu_\alpha$ , where the sterile neutrino decays into three active neutrinos,  $\nu_\alpha$  [30]. Unfortunately it is a very challenging signature to detect experimentally. Active neutrinos are detected in huge underground experiments and even though it is possible to determine the original direction of a detected neutrino, the resolution is not very good and many detected neutrinos originate in processes in the atmosphere or inside the Earth. It makes it difficult to tell whether a given detected neutrino is a decay product of dark matter.

If  $m_s > m_\alpha$  the radiative decay  $\nu_s \rightarrow \nu_\alpha + \gamma$  shown in Fig. 7 becomes allowed.

The decay is achieved by  $\nu_s$  virtually transforming itself into two charged particles. This is possible if the mass eigenstate of the sterile neutrino couples to a  $W$  boson and transforms it into a charged lepton ( $e, \mu, \tau$ ) [29, 32]. One of the charged particles can emit a photon and hereafter the two charged particles recombine to form a  $\nu_\alpha$ .

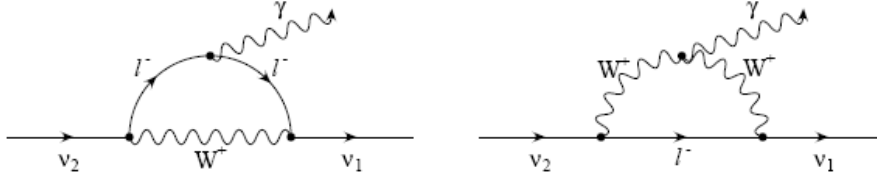


**Figure 7:** The Feynman diagrams for a  $\nu_s$  virtually transforming itself into two charged particles by the coupling of the mass eigenstate to a  $W$  boson and thereby decaying radiatively [32, 33].

The kinematics of the reaction give that the photon must be mono-energetic and the energy in the  $\nu_s$  rest frame can be determined from energy and momentum conservation (two-body decay) [19]:

$$E_\gamma = \frac{1}{2}m_s \left( 1 - \frac{m_\alpha^2}{m_s^2} \right). \quad (15)$$

If  $m_s \gg m_\alpha$ , which is likely since  $\sum_\alpha m_\alpha \lesssim 5eV$  [22] and  $m_s$  is of the order of keV, then  $E_\gamma \approx m_s/2$ . The branching ratio for the radiative decay has been derived to be [30]:

$$\frac{\Gamma_\gamma}{\Gamma_{tot}} = \frac{27\alpha}{8\pi} \approx \frac{1}{128}. \quad (16)$$

The radiative decay is a testable signature of the sterile neutrinos as dark matter<sup>4</sup>. A mass of  $m_s \approx 0.5 - 100$  keV is preferred by structure formation [11] leading to X-ray photon emission. X-ray observatories usually have a sensitivity range of  $E_\gamma = 0.3 - 10$  keV corresponding to a mass search range of  $m_s = 0.6 - 20$  keV.

## 2.6 Constraining the decay rate from the emitted photons

For a dark matter particle decaying radiatively with  $E_\gamma = m/2$  the upper limit on the detected flux originating from a given clump of matter can be converted into a constraint on the decay rate.

<sup>4</sup>A wide range of effects from neutrinos decaying into photons have been discussed for many years e. g. by Sciama [34].

The number of dark matter particles of mass  $m$  in a clump of matter is given by:

$$N = M_{tot}/m, \quad (17)$$

where  $M_{tot}$  is the total mass of dark matter, which is taken to be the total mass of the clump. The luminosity from dark matter particles decaying to photons is:

$$\mathcal{L} = E_\gamma N \Gamma_\gamma, \quad (18)$$

where  $E_\gamma$  is the photon energy and  $\Gamma_\gamma$  is the decay rate of the radiative decay. Then the flux at a luminosity distance,  $D_L$ , is:

$$F = \frac{\mathcal{L}}{4\pi D_L^2} = \frac{E_\gamma N \Gamma_\gamma}{4\pi D_L^2} \quad (19)$$

The observed flux,  $F_{det}$ , gives an upper limit for the flux from decaying dark matter so Eqn. 19 can be rewritten as:

$$\begin{aligned} \Gamma_{\gamma,max} &\leq \frac{8\pi F_{det} D_L^2}{M_{tot}} \\ &= 1.34 \cdot 10^{-4} \text{ sec}^{-1} \left( \frac{F_{det}}{\text{erg/cm}^2/\text{sec}} \right) \left( \frac{D_L}{\text{Mpc}} \right)^2 \left( \frac{M_{tot}}{M_\odot} \right)^{-1}. \end{aligned} \quad (20)$$

Fluxes are additive so if there are  $i$  dark matter sources of different masses at different distances, the last two terms of Eqn. 20 become  $\left[ \sum_i \frac{M_{tot}^i/M_\odot}{(D_L^i/\text{Mpc})^2} \right]^{-1}$ .

## 2.7 Is the flux measurable

If the dark matter particles are to be around today, as we can observe them, their lifetime has to be of the same order of magnitude as the age of the Universe i. e.  $\tau \gtrsim 4 \cdot 10^{17}$  sec giving a decay rate of  $\Gamma_{tot} \lesssim 2.5 \cdot 10^{-16} \text{ sec}^{-1}$  [4]. With the branching ratio given by Eqn. 16, a first estimate of the flux from decaying dark matter particles is:

$$F \lesssim 1.865 \cdot 10^{-14} \text{ erg/cm}^2/\text{sec} \left( \frac{M_{tot}}{M_\odot} \right) \left( \frac{D_L}{\text{Mpc}} \right)^{-2}. \quad (21)$$

As an example let us look at a typical cluster of galaxies where  $M_{tot} \approx 10^{14} M_\odot$  and  $D_L \approx 1000$  Mpc. This gives a flux of  $F \lesssim 2 \cdot 10^{-6} \text{ erg/cm}^2/\text{sec}$ . This order of magnitude is measurable by the X-ray observatories *Chandra* and *XMM* that both have a point source sensitivity of the order of  $F \gtrsim 10^{-15} \text{ erg/cm}^2/\text{sec}$  in a 100 ksec observation [35].

### 3 The Early Universe

The mass and mixing angle of the sterile neutrinos can be constrained from their interactions in the early universe. Before going into the specific case of the sterile neutrinos, the concept of distribution functions is introduced to describe the thermal evolution of the early Universe.

#### 3.1 The distribution function

In the early Universe (before decoupling) the number densities of radiation and matter were so high that the photons and the particles did not propagate very far before encountering another photon or particle to interact with. The particles are said to be in thermal equilibrium, if the interaction rates are fast compared to the expansion of the Universe,  $\Gamma(t) \gg H(t)$ , and standard thermodynamics can be used to describe the evolution. The interaction rate depends on the particle density, which decreases as the Universe expands with time, so at a given time, when  $\Gamma(t) \approx H(t)$ , the particles decouple and essentially stop interacting.

The distribution function describes the number of particles of specie “ $i$ ” with a given momentum at a given temperature,  $T_i$ . For a dilute, weakly interacting gas, it is given either by Fermi-Dirac statistics for spin- $\frac{1}{2}$  particles called fermions (“+” in Eqn. 22) or by Bose-Einstein statistics for particles with even valued spin called bosons (“-” in Eqn. 22) [36]:

$$f_i(p) = \frac{1}{e^{(E_i - \mu_i)/T_i} \pm 1}, \quad (22)$$

where  $E_i^2 = m_i^2 + p^2$  is the particle energy and  $\mu_i$  is the chemical potential related to the numerical difference between particles and anti-particles. Normally the number densities of particles and anti-particles are taken to be equal in the early Universe and  $\mu_i$  is neglected [37].

An important quantity is the number of internal degrees of freedom,  $g_i$ , of the  $i^{\text{th}}$  particle specie, since the species contribute differently to the number density, the energy density, the pressure etc. The number of internal degrees of freedom is given by the number of polarization states e. i.  $g_\gamma = 2$ ,  $g_{e,\mu,\tau} = 2$ ,  $g_\nu = 1$  (there exist only left-handed neutrinos and right-handed anti-neutrinos according to the standard model), etc.

The number density and the energy density is calculated by integrating over the full momentum phase space [37]:

$$n_i = \frac{g_i}{(2\pi)^3} \int f_i(p) d^3p = \frac{g_i}{(2\pi^2)^3} \int f_i(p) \sqrt{E_i^2 - m_i^2} E_i dE, \quad (23)$$

$$\rho_i = \frac{g_i}{(2\pi)^3} \int f_i(p) E_i(p) d^3p = \frac{g_i}{(2\pi^2)^3} \int f_i(p) \sqrt{E_i^2 - m_i^2} E_i^2 dE, \quad (24)$$

where the last equality in both equations is for an isotropic distribution function, in which the momentum,  $p$ , does not depend on the position so  $d^3p = 4\pi p^2 dp$  and  $E_i^2 = m_i^2 + p^2$  as usual.

In the ultra-relativistic limit where  $T_i^2 \approx E_i^2 \gg m_i^2$ , it is possible to solve the integrals analytically [37]:

$$n_i^{rel} = \begin{cases} 1.202 g_i T_i^3 & \text{Bose - Einstein} \\ \frac{3}{4} (1.202 g_i T_i^3) & \text{Fermi - Dirac} \end{cases}, \quad (25)$$

$$\rho_i^{rel} = \frac{g_i}{6\pi^2} \int_0^\infty \frac{E_i^3}{e^{E_i/T_i} \pm 1} = \begin{cases} \frac{\pi^2}{30} g_i T_i^4 & \text{Bose - Einstein} \\ \frac{7}{8} \left( \frac{\pi^2}{30} g_i T_i^4 \right) & \text{Fermi - Dirac} \end{cases}. \quad (26)$$

If we want to calculate the total contribution to  $\rho$  (and  $n$ ) from all species in the early Universe, it is a good approximation to include only the relativistic species since the non-relativistic species pick up an exponential suppression, when integrating Eqn. 24 in the non-relativistic limit. For a mean plasma temperature,  $T$ , the energy density becomes [37]:

$$\rho_{tot}^{rel} = \frac{\pi^2}{30} g_*(T) T^4, \quad (27)$$

where  $g_*$  is the effective number of degrees of freedom of the particles including the 7/8 in Eqn. 26 for the fermions (3/4 if calculating the total number density) and accounting for varying temperatures of the different particle species [37]:

$$g_* = \sum_{i=\text{bosons}} g_i \left( \frac{T_i}{T} \right)^4 + \frac{7}{8} \sum_{j=\text{fermions}} g_j \left( \frac{T_j}{T} \right)^4. \quad (28)$$

The production peak of the sterile neutrinos takes place close to the quark-hadron phase transition (the quarks freeze out from a quark gluon plasma and form composite particles)<sup>5</sup>. This phase transition changes  $g_*$  drastically around  $T \approx 200$  MeV as seen in Fig. 8. The value of  $g_*$  for sterile neutrinos is usually considered to be between 10.75 as for the active neutrinos [37] and 20, depending on the details of the phase transition described by the strong interaction in a theory called Quantum Chromo<sup>6</sup> Dynamics (QCD), which is not fully understood yet.

<sup>5</sup>For an introduction to quark gluon plasmas see [39].

<sup>6</sup>Chromo means colour and refers to the colour charge of the quarks, not to be taken too literally.

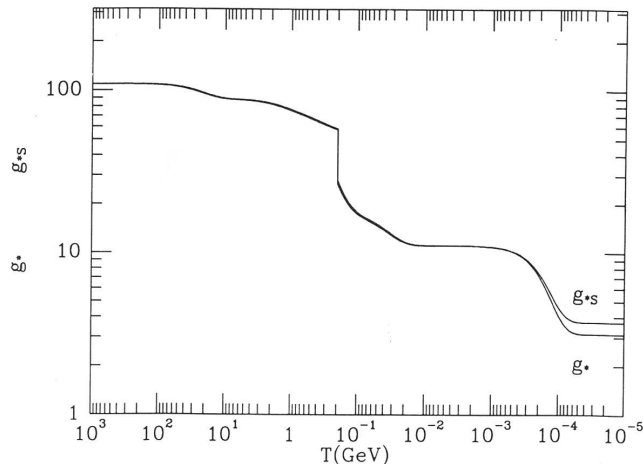


**Figure 8:** The evolution of  $g_*(T)$  as a function of temperature,  $T$ . The sharp edge at  $T \approx 170$  keV is the quark-hadron phase transition [38].

Throughout the report the value  $g_*(T_{produced}) = 15$  has been used as a reference value, corresponding to a production peak of the sterile neutrinos at  $T = 170$  MeV [40].

In the early Universe the curvature can be neglected (at least if the Universe was either radiation or mass dominated) and the Friedmann equation (Eqn. 2) can be rewritten as:

$$H^2(t) = \frac{\dot{a}(t)}{a(t)} = \frac{8\pi G \rho_{tot}^{rel}(t)}{3} = 2.76 g_* \frac{T^4}{m_{Pl}^2}, \quad (29)$$

by demanding the Universe to be flat ( $\kappa = 0$ ,  $\rho_0 = \rho_c$ ) and using the definition of  $\Omega = \rho(t)/\rho_c$ . The typical mass scale related to  $G$  is the Planck mass,  $m_{Pl}$ . By simple dimensional analysis  $G = \hbar c/m_{Pl}^2$  that in natural units ( $\hbar = c = k_B = 1$ ) reduces to  $G = 1/m_{Pl}^2$ , which gives  $m_{Pl}$  a value of  $m_{Pl} = 1.221 \cdot 10^{25}$  keV [37]. In the last equality of Eqn. 29 the expression of Eqn. 27 has been inserted for  $\rho_{tot}^{rel}$ .

### 3.2 The Boltzmann equation

The sterile neutrinos are assumed to be produced through collisions processes between leptons

$$l_1 + l_2 \rightarrow \nu_s + l_3. \quad (30)$$

When the particles are involved in interactions, such as production, their distribution function changes. The time evolution of the distribution function is given by the Boltzmann transport equation [36]. For the sterile neutrinos it can be written

as [37]:

$$\left(\frac{\partial}{\partial t} - pH(t)\frac{\partial}{\partial p}\right) f_s(p) = I_{coll}, \quad (31)$$

where the first term on the left hand side describes the time evolution, the second term describes the Hubble expansion and the right hand side describes the interactions in the form of collisions.  $I_{coll}$  is called the collision integral. It can either be determined analytically [41] or it can be determined from a simple physical approximation of which the resulting estimated number density  $n_s$  lies within a factor of 2 of the one from the analytical approach. In both cases the sterile neutrinos are assumed to be initially absent and only produced through neutrino oscillations in leptonic collision processes as the one in Eqn. 30. It is possible that there are other creation processes such as coupling to the scalar field of inflation [26] or through hadronic interactions [28]. Nonetheless the dominant production is through the leptonic collisions and alternative production processes can be neglected. Here the physical approximation is described in detail and only short comments on the analytical solution and more complicated numerical solutions including other production methods, are given in Sec. 3.5 and Sec. 3.6.

### 3.3 The simple physical approximation

The sterile neutrinos do only interact through oscillations with the active neutrinos. Therefore the collision integral on the right hand side of Eqn. 31 can be approximated as the rate of weak interactions of the active neutrinos suppressed by the mixing angle of the sterile neutrinos in matter.

The interaction rate for a given type of particles depends on their number density,  $n$ , their velocity,  $v$ , and their ‘‘probability of interaction’’ given by the cross-section,  $\sigma$ :  $\Gamma = nv\sigma$ . The number density of relativistic fermions evolves with time as  $n \propto a^{-3} \propto T^3$  (Eqn. 26). Neutrinos (including the sterile) are very light particles ( $m^2 \ll E^2 \approx T^2$ ) so they are ultra-relativistic in the early Universe and  $v \approx c = 1$ . The cross-section for the weak interactions goes like [37]:

$$\sigma_W \sim 1.202 \frac{\alpha^2 T^2}{m_W^4}, \quad (32)$$

where  $\alpha$  is the fine structure constant,  $\alpha \approx 1/128$  [19], and  $m_W$  is the characteristic mass of the weak interactions namely the mass of the W-boson,  $m_W \approx 81$  GeV [19]. The interaction rate of the weak interactions then becomes:

$$\Gamma_W = n \frac{\alpha^2 T^2}{m_W^4} \approx \frac{\alpha^2 T^5}{m_W^4}. \quad (33)$$

The interaction of the sterile neutrinos are suppressed by the mixing angle. The relevant suppression factor of the cross-section is  $\sin^2(2\theta_M)/4$  [21] so the approximated Boltzmann equation becomes:

$$\left(\frac{\partial}{\partial t} - pH(t)\frac{\partial}{\partial p}\right) f_s(p) = \frac{\sin^2(2\theta_M)}{4} \Gamma_W f_\nu(p). \quad (34)$$

The mixing angle of the sterile neutrinos described in Sec. 2.4 is influenced by matter effects and suppressed at large temperatures [42, 43]:

$$\sin^2(2\theta_M) = \frac{\sin^2(2\theta)}{1 + 3.73 \cdot 10^{-16} C(m_s/\text{keV})^{-2} (y^2/x^6)}, \quad (35)$$

where  $C$  is a numerical constant which for mixing with  $\nu_e$  takes the value  $C_e = 0.61$ , and for mixing with  $\nu_{\mu,\tau}$  takes the value  $C_{\mu,\tau} = 0.17$  (however for temperatures near the mass of  $\nu_\mu$ ,  $C$  becomes equal for  $\nu_e$  and  $\nu_\mu$ ).  $x$  and  $y$  are unit-less variables defined as  $x = a(t)$  MeV and  $y = E \cdot a(t) = p \cdot a(t)$ .

### 3.4 Integration of the Boltzmann equation

To isolate  $f_s(p)$  we start by rewriting the right-hand side of the Boltzmann equation (Eqn. 31) as a function of  $x$  and  $y$ , using the notations  $f_s = f_s(x, y)$ ,  $a = a(t)$ ,  $H = \dot{a}/a = \dot{x}/x = H(t)$  (the details of the calculations can be found in App. A.2) [31]:

$$xH \frac{\partial}{\partial x} f_s = \frac{\sin^2(2\theta_M)}{4} \Gamma_W f_\nu. \quad (36)$$

What we are looking for is the distribution function,  $f_s$ , which can be found by integrating Eqn. 36 over  $x$ :

$$f_s = \int_0^\infty \frac{\sin^2(2\theta_M)}{4} \frac{\Gamma_W}{xH} f_\nu dx. \quad (37)$$

$\Gamma_W/H$  can be expressed from the rewritten Friedmann equation (Eqn. 29) and the decay rate of the weak interactions (Eqn. 33):

$$\frac{\Gamma_W}{H} = \frac{1.202 \frac{\alpha^2 T^2}{m_W^4}}{\sqrt{2.76 g_* \frac{T^2}{m_{Pl}^2}}} = 0.72 \frac{\alpha^2}{\sqrt{g_*}} \frac{m_{Pl}}{m_W^4}. \quad (38)$$

With Eqn. 38, the expression for  $\sin^2(2\theta_M)$  given by Eqn. 35 and  $x = a(t) \cdot \text{MeV} = \text{MeV}/T$ , the integral in Eqn. 37 can be written as:

$$f_s = K_1 f_\nu \int_0^\infty \frac{1}{x^4} \frac{1}{1 + K_2^2/x^6} dx, \quad (39)$$

where  $f_\nu$  has been extracted from the integral since the active neutrinos are taken to be in thermal equilibrium and therefore their distribution function does not depend on  $x$ .  $K_1$  and  $K_2$  are constants defined as:

$$\begin{aligned} K_1 &= 0.72 \frac{\sin^2(2\theta)}{4} \frac{\alpha^2}{\sqrt{g_*}} \frac{m_{Pl}}{m_W^4} MeV^3, \\ K_2 &= \sqrt{2.27 \times 10^{-20} y^2} \frac{MeV}{m_s}. \end{aligned} \quad (40)$$

The integral can be performed by a change of variable by using [44]:

$$\int_0^\infty \frac{dx}{c^2 + x^2} = \frac{\pi}{2c}, \quad (41)$$

to become:

$$f_s = K_1 \frac{\pi}{2} \frac{1}{3K_2} f_\nu = C f_\nu, \quad (42)$$

where it is seen that the distribution function of the sterile neutrinos,  $f_s$ , is directly proportional to that of the active neutrinos,  $f_\nu$ . Also the number densities are then proportional:

$$n_s = \int f_s d^3p = C \int f_\nu d^3p = C n_\nu. \quad (43)$$

If the sterile neutrinos are assumed to account for all dark matter in the Universe, the density parameter,  $\Omega_{DM}$ , can be expressed as :

$$\begin{aligned} \Omega_{DM} h^2 &= \frac{n_s m_s}{\rho_c} = \frac{C n_\nu m_s}{\rho_c} \\ &= \left( \frac{0.72\pi}{\sqrt{2.27 \cdot 10^{-20} y}} \frac{\sin^2(2\theta)}{24} \frac{\alpha^2}{\sqrt{g_*}} \frac{m_{pl}}{m_W^4} MeV^2 \frac{n_\nu}{\rho_c} \right) m_s^2 \\ &= B \cdot \sin^2(2\theta) m_s^2 \\ &\Leftrightarrow \\ \sin^2(2\theta) &= \frac{\Omega_{DM} h^2}{B m_s^2}, \end{aligned} \quad (44)$$

where  $B$  does not depend on the mass or on  $\sin^2(2\theta)$ . Note that for the sterile neutrinos  $\Omega_{DM} h^2 \propto m_s^2$  which is different from the case of the active neutrinos where  $\Omega_{DM} \propto m_\alpha$  [37]. If the sterile neutrinos are produced by some other mechanism than leptonic collisions (Eqn. 30), Eqn. 45 is no longer viable and no constraints have been derived from the conditions of the early Universe [25].

### 3.5 Analytical collision integral

The difference between the simple approach and the analytical solution of the Boltzmann equation (by Dolgov and Hansen [41]) is that instead of approximating the collision integral in Eqn. 36 by the order of magnitude of the electroweak interaction, all possible interactions including a sterile neutrino are considered and all the interaction matrix elements contributing to the cross-section are computed. The result is given by Eqn. 209 and Eqn. 210 in [45]:

$$\begin{aligned} \sin^2(2\theta) \approx & 1.14 \cdot 10^{-7} \left( \frac{A}{6.7 \cdot 10^{-8}} \right) \left( \frac{g_*(T_{produced})}{15} \right)^{3/2} \\ & \times \left( \frac{S}{1} \right) \left( \frac{\Omega_{DM}}{0.26} \right) \left( \frac{h}{0.71} \right)^2 \left( \frac{m_s}{\text{keV}} \right)^{-2}, \end{aligned} \quad (46)$$

where  $A$  is a constant depending on the type of active neutrino, the sterile neutrinos are assumed to mix with. It takes the values  $A_{se} = 6.7 \cdot 10^{-8}$  for  $\nu_s$  mixing with  $\nu_e$  and  $A_{s\mu} = 4.8 \cdot 10^{-8}$  for  $\nu_{\mu,\tau}$ .  $g_*(T_{produced})$  is the number of relativistic degrees of freedom at the temperature, where the sterile neutrinos are produced (discussed in Sec. 3.1).  $S$  is a free parameter taking into account a possible additional entropy production after the sterile neutrinos have been created. This entropy production could be from decays of the heavier sterile neutrino mass eigenstates, leading to a dilution of the momentum distribution of the sterile neutrinos. The characteristic size of structure formation must remain the same even with the additional entropy production and we have [25]:

$$m_s S^{1/3} \propto \text{constant}. \quad (47)$$

Also the temperature of the sterile neutrinos will be diluted by a factor of  $S^{1/3}$ .  $S$  was originally suggested to be in the range between 1 and 100 [25] and later proposed to be between 1 and 2 [25, 26].

If there is a difference between the number density of particles and anti-particles, the chemical potential in the distribution function (Eqn. 22) cannot be neglected. As the sterile neutrinos are produced through leptonic collisions (Eqn. 30), only the difference between leptons and anti-leptons is important. A measure of the possible asymmetry is the cosmological lepton number defined as [31]:

$$L = \frac{n_\nu - n_{\bar{\nu}}}{n_\gamma}, \quad (48)$$

The value of  $L$  is constrained experimentally from the primordial helium abundance and from the mixing angle of the active neutrinos to be:  $|L_e| < 0.05$  and  $|L_\mu + L_\tau| < 0.4$  [46]. Usually it is assumed to be of the same order of magnitude as the equally defined cosmological baryon number,  $B \approx 10^{-5}$ , so it is negligible and

$L \approx 0$ . A negative value of  $L$  describes a Universe with more anti-leptons than leptons in contradiction with observations, namely a Universe with more matter than anti-matter. A positive value of  $L$  allows for a resonant production of the sterile neutrinos which gives an overproduction [47]. Eqn. 46 is derived for  $L \approx 0$ , in which case it gives an upper limit on the mixing angle. However this limit is not very robust. The details of the quark-hadron phase transition are not very well known and the exact value of  $g_*(T_{produced})$  might change the constraint significantly. Additional production mechanism will add extra terms in the Boltzmann (Eqn. 31) and will also change Eqn. 46.

### 3.6 Numerical solutions of the Boltzmann equation

Numerical solutions of the Boltzmann equation have been done including the effects of the quark-hadron phase transition taking place at temperatures comparable to the temperature at which the sterile neutrinos are produced [40]. The hadrons and leptons produced in the transition, will annihilate and reheat the plasma and the coupled active neutrinos relative to the decoupled sterile neutrinos which are diluted and spectrally distorted. However in the 0.5 – 10 keV mass range, the distribution function of the sterile neutrino does not change more than a factor of five compared to that of the active neutrinos [40].

The numerical calculations are well fitted by the expression [40]:

$$m_s = 3.40 \text{ keV} \left( \frac{\sin^2(2\theta)}{10^{-8}} \right)^{-0.615} \left( \frac{\Omega_{DM}}{0.26} \right)^{0.5} \times \left( 0.527 \text{erfc} \left[ -1.15 \left( \frac{T_{QCD}}{170 \text{ MeV}} \right)^{2.15} \right] \right), \quad (49)$$

where  $T_{QCD}$  is the temperature of the quark-hadron phase transition, and the quantity inside the last set of brackets including the error-function is unity for  $T_{QCD} = 170 \text{ keV}$ .

In Sec. 11 it will be clear that the results obtained from the analytical and numerical solutions are almost identical for  $m_s \approx 0.5 - 20 \text{ keV}$  if  $T_{QCD}$  is taken to be  $T_{QCD} = 170 \text{ keV}$ . However, the details of the QCD phase transition are not yet very well understood, and they may affect the production of the sterile neutrinos and change it by a factor of a few [48, 49].

The numerical solution including the phase transition has also been carried out for  $L > 0$  allowing for other production mechanisms than the leptonic collisions (Eqn. 30) such as resonant productions [50]. Fig. 9 shows how the relation between  $\sin^2(2\theta)$  and  $m_s$  changes for different values of  $L$ . As  $L$  augments, smaller and smaller mixing angles are needed (allowed).

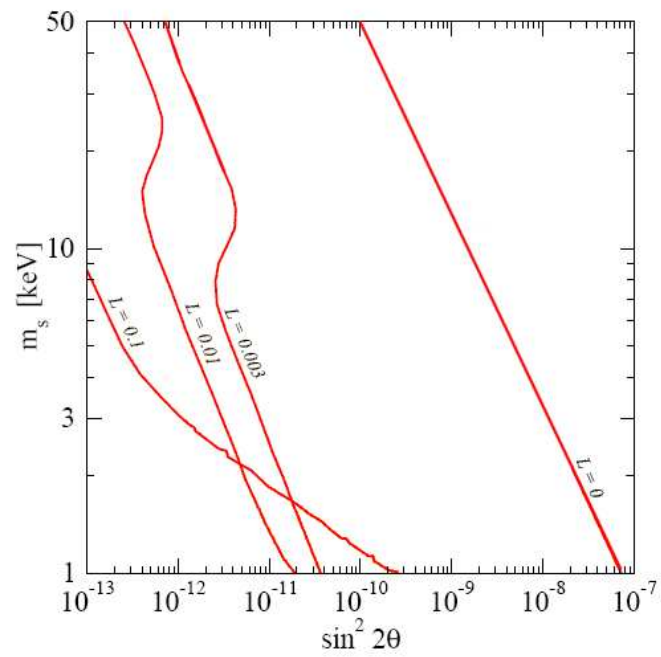


**Figure 9:** The relation between  $\sin^2(2\theta)$  and  $m_s$  changes for different values of  $L$  (for  $\Omega_s = 0.24$ ) [50].

## 4 X-ray Observations

At this point we have learned that the sterile neutrino is a keV-mass particle that only interacts through mixing with the active neutrinos. A small fraction of the decays are radiative and the signature of sterile neutrinos is a mono-energetic emission line with  $E_\gamma = m_s/2$  in the X-ray range. In this section X-ray observations and observatories are presented.

### 4.1 X-ray observatories

X-rays are absorbed by the Earth's atmosphere and therefore X-ray observations have to be carried out from space. For the time being there are two X-ray observatories operating onboard satellites: *XMM-Newton* (ESA) and *Chandra* (NASA).

The concept behind the two observatories is the same. The incoming X-ray photons are collected and focused by grazing incidence telescopes as seen in Fig. 10. The focal planes are equipped with CCD cameras allowing for measurements of the energy and the position of each incoming photon individually. This permits spatially resolved spectroscopy with medium resolution ( $\Delta E_\gamma \approx 0.1$  keV) in the energy range  $E_\gamma = 0.3 - 10$  keV [8]. Higher resolution spectroscopy of point-like objects can be performed by using gratings inserted between the mirrors and the CCDs.

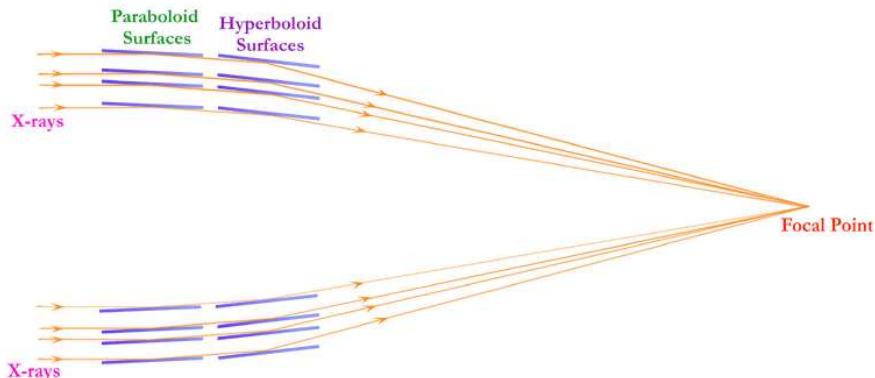


**Figure 10:** The Chandra mirrors [52].

*Chandra* has a good spatial resolution ( $\Delta\theta_{Chandra} \approx 0.5$  arcsec where  $\Delta\theta_{XMM} \approx 8$  arcsec), but as it is only equipped with one telescope, where *XMM* has three telescopes operating in parallel, its effective area is 3 to 5 times smaller than for *XMM*. The total on-orbit background level of *Chandra* is a bit lower than that of *XMM* [35, 51]. In this work only *Chandra* data has been analysed but when it

has been possible, the obtained results have been compared to published *XMM* results.

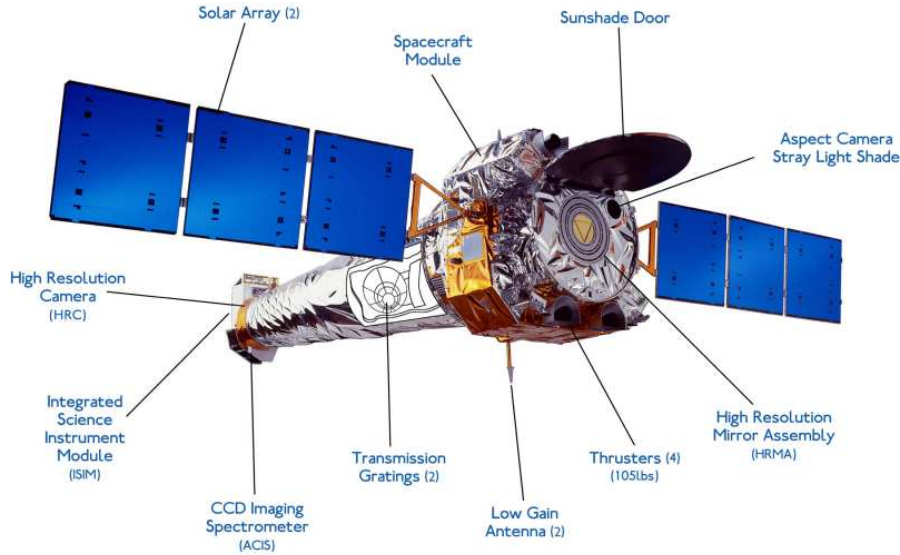


*Figure 11:* Chandra [52].

## 4.2 Chandra details

*Chandra* is approximately 10 m long and was launched by NASA in 1999 to an orbit of 139,000 km, which is about a third of the distance to the moon [52]. It has only one telescope with Ir-coated mirrors, called the High-Resolution Mirror Assembly (HRMA), but in the focal plane it is possible to change between two detector arrays; the High Resolution Camera (HRC) with a very high spatial resolution and the Advanced CCD Imaging Spectrometer (ACIS) with a good spectral resolution. The spectral resolution can be improved by a factor of approximately 50 by applying one of the two transmission gratings, LETG and HETG, which are described in Sec. 4.3. *Chandra* provides calibrated data for the energy interval 0.3 – 10.0 keV. In this report only data from observations with the ACIS camera has been analysed because of its better spectral resolution.

The ACIS camera consists of two CCD arrays, ACIS-I with 4 chips and ACIS-S with 6 chips, arranged as shown in Fig. 12. The ten chips covers each a field of approximately  $(8.1 \text{ arcmin})^2$  but during observations only six of the ten chips can be active (due to telemetry constraints). Two of the ten chips (ACIS-S1 and S3) have been treated specially and are back-illuminated thereby extending their sensitivity to lower energies than the rest of the chips which are front-illuminated.

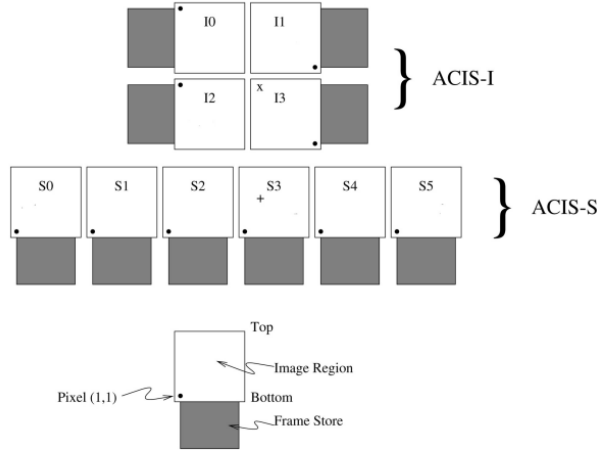


**Figure 12:** A schematic view of the *Chandra* ACIS focal plane layout. The “x” at the I3 chip and the “+” at the S3 chip represents the aiming points for observations with ACIS-I and ACIS-S respectively [52].

The spectral resolution of the ACIS chips given as Full Width Half Maximum is shown in Fig. 13. For ACIS-S3 the resolution expressed as the standard deviation for a Gaussian distribution ( $FWHM \approx 2.35\sigma$ ), is approximated by a linear function of photon energy,  $E_\gamma$ :

$$\sigma_{S3} = 0.005E_\gamma + 0.05 \text{ keV} \quad (50)$$

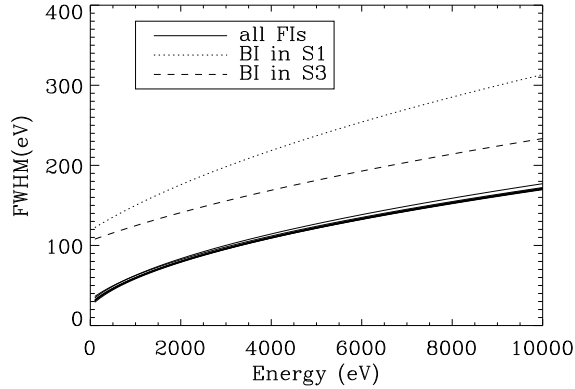


**Figure 13:** The resolution of the *Chandra* ACIS chips given as the full width half maximum ( $FWHM = 2.35\sigma$ ) [35].

The optical components of a galactic or cluster halo have velocity dispersions of the order of  $v/c \approx 10^{-5}$  to  $10^{-4}$  [53]. The dark matter is assumed to have the same

velocity dispersion. Therefore it can be taken to be at rest and the line broadening due to motion can be neglected since it is of the order of  $E_{obs}/E_{em} = 1.0001$ , which is the same as a broadening of 0.1 eV at 1 keV. This is much smaller than the energy resolution of *Chandra* (and *XMM*) observations even with a grating. In Fig. 14 is shown the spectrum of the cluster of galaxies A1835 and three Gaussians representing three hypothetical mono-energetic emission lines at 1.0 keV, 5.0 keV, and 9.0 keV respectively with a width corresponding to the instrumental resolution at the given energy. The normalisation of the Gaussians are arbitrarily chosen so they are clearly visible on the plot.

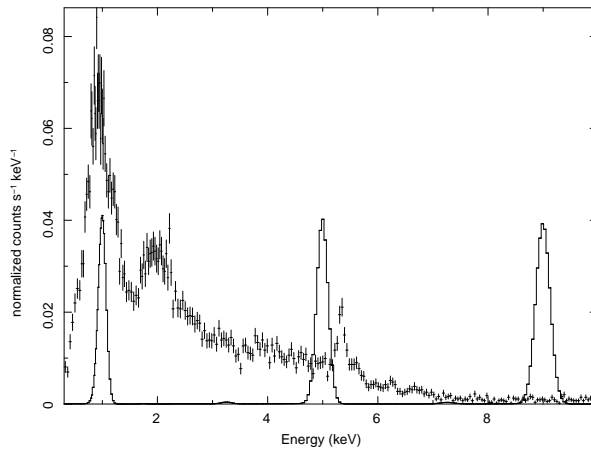


**Figure 14:** Spectrum of the cluster of galaxies A1835 with three Gaussians representing three hypothetical mono-energetic emission lines at 1.0 keV, 5.0 keV, and 9.0 keV respectively with arbitrary normalisations.

More information of *Chandra* can be found in the Proposers Guide [35] or in Jesper Rasmussens PhD Thesis [54]. Details on data analysis can be found in the CIAO data analysis guide [55].

### 4.3 Gratings

The X-rays arriving from a point source can be deflected in a grating allowing for a very high spectral resolution. The High Energy Transmission Grating, HETG, onboard *Chandra*, intercepts the X-rays reflected from the mirrors, changing their direction by amounts that depend sensitively on the energy of the incoming photons. One of the focal plane detectors (HRC or as in our case the ACIS-S) records the location of the diffracted X-rays, enabling a precise determination of their energies with an accuracy better than  $E_{\gamma}/\sigma_E \approx 1000$  [56].

The HETG consists of 336 gold grating facets mounted on a multiple ring formed assembly that can be swung into position between the *Chandra* mirrors and the CCDs. The inner two rings are High Energy Grating, HEG, facets, and the outer two rings are Medium Energy Grating, MEG, facets. The HETG facets are made of gold bars, which are spaced closer together than the wavelength of visible light. The bars are supported by plastic membranes, which are as thin as a soap bubble ( $\approx 10^{-7}$  m), yet they can withstand the trauma of a shuttle launch. The gratings take advantage of the fact that the gold bars are partially transparent to X-rays, so that the diffraction is more efficient, and more X-rays are captured by the CCDs.

The HETG gratings are designed to cover an energy range from 0.4 keV to 10 keV with HEG covering the interval  $E_\gamma = 0.8 - 10.0$  keV and MEG covering  $E_\gamma = 0.4 - 5.0$  keV. The very high spectral resolution is used in the study of detailed energy spectra, distinguishing individual X-ray lines from specific atomic transitions or as in our case from decaying dark matter. The exact resolutions of the HEG and MEG spectrometers are given in Tab. 2.

Grating part	Resolution, FWHM [ $\text{\AA}$ ]	Default Bin Size [ $\text{\AA}$ ]
HEG	0.012	0.0025
MEG	0.023	0.005

**Table 2:** Resolutions and default bin sizes for HEG and MEG [57].

The default pipe line bin size of HEG and MEG is oversampled by a factor of 4–5 so the binning is finer than the actual instrumental resolution. To account for this and to improve statistics, the data can be rebinned by a factor of “ $x$ ”. The data in Tab. 2 can be converted to an expression for the resolution as a function of energy. For HEG this converts to:

$$\frac{\lambda}{\Delta\lambda_{FWHM}} = \frac{\lambda}{x \cdot 0.0025\text{\AA}}. \quad (51)$$

where the value  $x = 4.8$  corresponds to the instrumental resolution. This gives an energy resolution of:

$$\Delta E_{FWHM} = \frac{x(E_\gamma/\text{keV})^2}{4972} \text{keV} \Rightarrow \sigma_{HEG} = \frac{x(E_\gamma/\text{keV})^2}{11684} \text{keV} \quad (52)$$

And for MEG:

$$\frac{\lambda}{\Delta\lambda_{FWHM}} = \frac{\lambda}{x \cdot 0.005\text{\AA}}, \quad (53)$$

$$\Delta E_{FWHM} = \frac{x(E_\gamma/\text{keV})^2}{2486} \text{keV} \Rightarrow \sigma_{MEG} = \frac{x(E_\gamma/\text{keV})^2}{5842} \text{keV}. \quad (54)$$

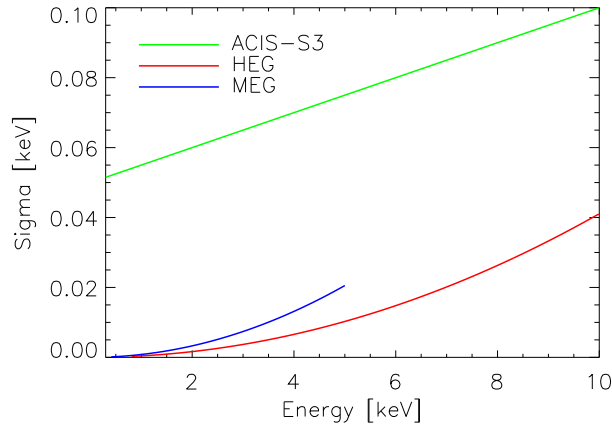


**Figure 15:** The resolution of HEG (red) and MEG (blue) compared to the resolution of ACIS-S3 (green).

## 5 Analysis of X-ray Data

In this section the X-ray data analysis procedure and the needed software tools are described.

### 5.1 The raw data

A year after observation all *Chandra* observations become public and can be accessed through NASA’s High Energy Astrophysics Science Archive Research Centre, HEASARC [58]. From there it is possible to download available data for any given object. All observations are denoted with a number called the “observation identification”.

For *Chandra*, the obtained data consist of the “raw” data files called secondary files, and the default pipe-line processed data files called primary files, which are “level2” files to be used straight away for data analysis. I have analysed the level2 data files adhering to Jesper Rasmussens “analysis guide” [59].

### 5.2 CIAO and Sherpa

*Chandra* observation data are analysed with the Chandra Interactive Analysis of Observations, called CIAO<sup>7</sup>. It is a mission independent command-line based data analysis system, which is designed to handle N-dimensional data files [55]. The modelling and fitting tool “Sherpa” is central to the CIAO system. Sherpa

<sup>7</sup>CIAO comes from “s’sciavo” meaning “I am your servant” in Venetian

performs forward fitting of models to data in N dimensions. Sherpa includes the “S-Lang” [60] language which can be used for scripting and data manipulation [61]. Another spectral fitting package included in CIAO is the tcl-based Xspec [62, 63].

### 5.3 Bad pixels, good time intervals and point source removal

Before the actual data analysis can take place it is necessary to take care of bad pixels in the CCDs, radiative activity disturbing the observation, and point source removal.

The first step of the preparation is to locate the bad-pixel file among the primary files, and set up the system to use this file containing observation specific information about the CCD pixels.

The next issue is the bad events which origin in cosmic rays instead of in X-rays but produce similar signatures in the detectors. For ACIS all events are automatically assigned a grade according to the event detection pattern within a  $3 \times 3$  CCD pixel island and some events are rejected by the default pipe-line according to the shape and splitting of these pixel values. For observations of very faint sources there exist a “Very Faint” mode, which uses a  $5 \times 5$  pixel island to grade the events. This allows for an improved grade assessment of which events are probable cosmic rays and thus enabling a superior extraction of non X-ray events relative to the standard “Faint” mode [54]. If the data are observed in the Faint mode, the primary files provided by HEASARC are normally ready to use, but if the data are observed in the Very Faint mode or with a grating, the data need to be reprocessed from the secondary files to create new primary files following the instructions of the CIAO web page [55].

Thanks to the orbit of *Chandra* the periods of flaring particle background are rare compared to *XMM*, but they still have to be identified and excluded [54]. This is done separately for each chip by plotting the “light curve” which is the number of received photons as a function of time and cut away those time intervals where the number of received photons deviates more than  $3\sigma$  from the mean as shown in the left part of Fig. 16.

Point sources can also be removed during the data preparation. CIAO features three algorithms for point source identification: Wavelets, Voronoi tessellation, and sliding-cell search. I have used the wavelet algorithm since it is the most effective all-round point source identifier [54]. The point sources are assumed to have a Gaussian shape and are then identified on statistical basis. More information on the methods can be found in [55]. An example of the point sources identified by the wavelet algorithm for an observation of the cluster of galaxies A383, is shown

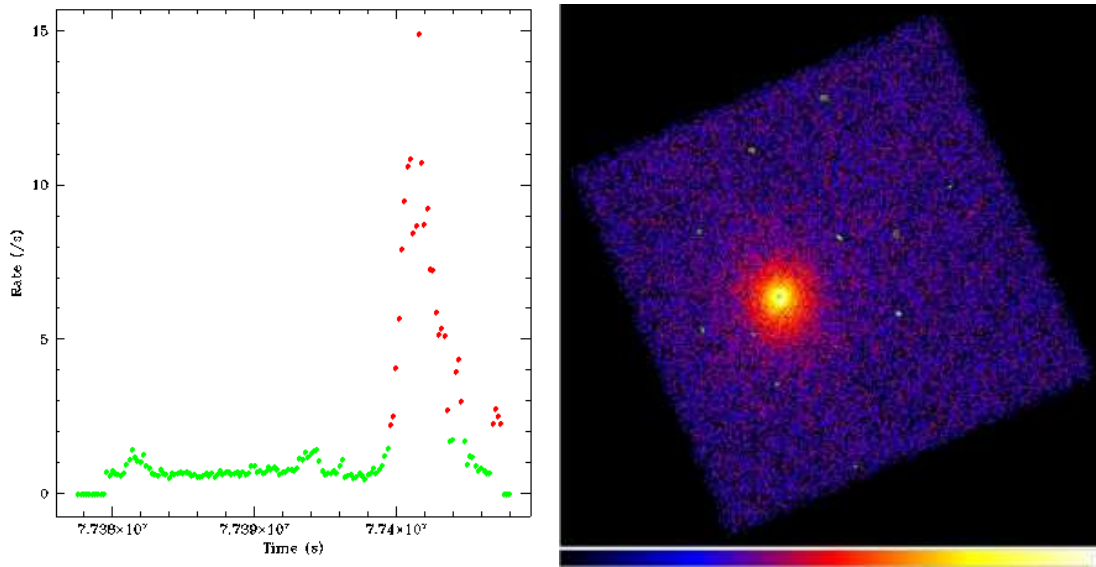


**Figure 16:** *Left:* An example of the lightcurve (number of received photons as a function of time) for the ACIS-S3 chip in a simulated observation. The points marked in red deviates more than  $3\sigma$  from the mean, and the time interval should be cut out [55]. *Right:* An observation of the cluster of galaxies A383 with the point sources found by wavelet detection marked by very small green spots.

in the right part of Fig. 16. If any point sources are removed, it is important to remove the same regions in a possible background data set (if applied).

## 5.4 Instrumental response

The energy and spatial distributions of the photons collected by the CCDs are not necessarily identical to the corresponding distributions of the incoming photons. This effect is caused by vignetting and the probability of an incoming photon to be detected by a given pixel in the CCD. Vignetting describes the variation in the effective photon collecting area of the telescopes as a function of photon energy and position relative to the optical axis of the telescope. The spatial part can be understood in terms of classical optics (in the case of no diffraction) by looking at Fig. 17: An incident wave will only be totally reflected from the mirror if the incident angle is less than the critical angle. If the incident angle is larger than the critical angle, the reflectivity decreases monotonically as a function of increasing angle and hence the effective photon collecting area decreases as a function of off-axis distance. One way to increase the effective area is to arrange several nearly cylindrical mirrors inside each other in a co-axial configuration as seen in Fig. 10. Vignetting is also energy dependent since the reflectivity of the high-

density materials used for mirror coating in general decrease with energy at X-ray frequencies.

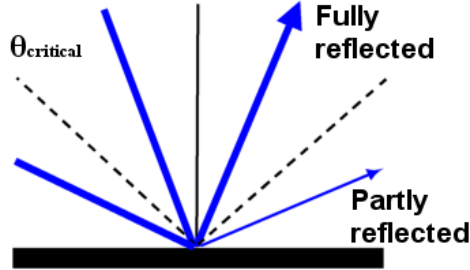


**Figure 17:** An incident wave will only be totally reflected from the mirror if the incident angle is less than a critical angle. If the incident angle is larger the reflectivity decreases monotonically as a function of increasing angle.

For imaging analysis the vignetting can be accounted for by using an exposure map, i. e. an image containing the effective exposure time at a given energy and detector position.

For spectra the vignetting can be accounted for by using two files to convert the observed photon energy distribution (in units of “normalized counts per instrument energy channel”) into an incident flux (in units of “photon energy (or number of photons) per area per time per energy”): A “redistribution matrix file”, *rmf*, which maps from instrument energy channel to incident photon energy i. e. converts between channel space and energy space; and an “ancillary response file”, *arf*, which accounts for the net effective area. As an example the *arf* file for an ACIS-S3 observations of the cluster of galaxies A383 is shown in Fig. 18.

## 5.5 Extracting spectra and instrumental response files

The regions for which the spectrum and background should be extracted, must be defined before the spectra can be extracted with the “*spec\_extract*” algorithm included in CIAO. Besides extracting the spectrum, it does also generate the *arf* and *rmf* files described in Sec. 5.4. The resulting extracted spectrum has been shown in Fig. 19 for the outer parts of the cluster A383. If nothing is subtracted as background, the spectrum includes contributions from the Cosmic X-ray Background (CXB), unresolved sources within the field of view, emission from the Milky Way halo, and instrumental effects apart from X-rays from the source.

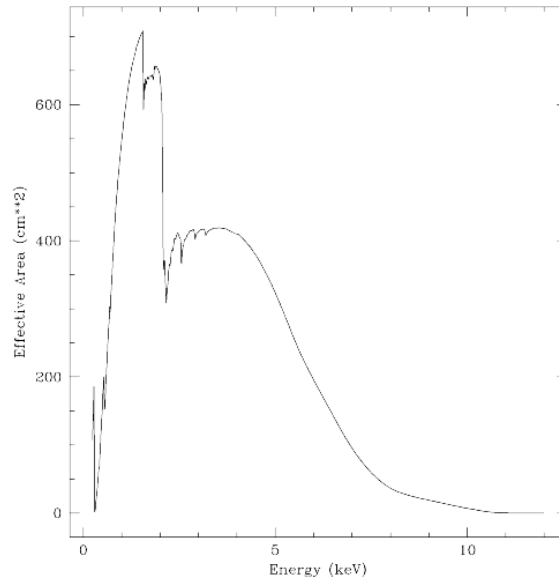


**Figure 18:** The net effective area of a *Chandra* ACIS-S3 observation of the cluster of galaxies A383 corrected for the ACIS quantum efficiency degradation.

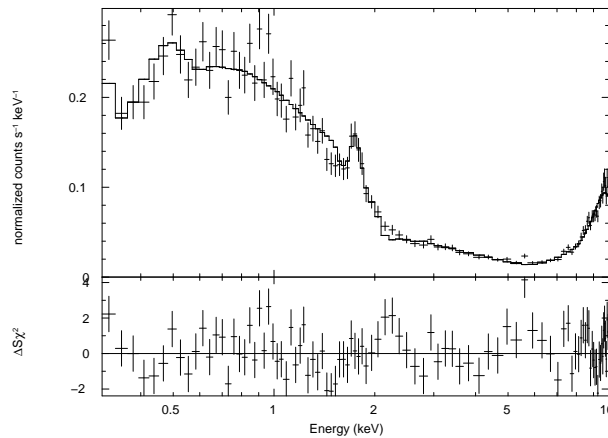


**Figure 19:** The spectrum of the outer parts of the cluster A383 fitted to a spectral model consisting of an exponential, a power law and two Gaussians.

## 5.6 Background subtraction

Background subtraction is a rather non-trivial task because the background consist of several components with a different dependence on energy and position, both of the detector and the sky. There are three possibilities for subtracting the background: using another part of the same observation, using blank sky data, or

using a model for the background [54].

If the spectrum is extracted from a region that does not cover all of the observation, another part of the observation can be used as background. The advantage is that the background will be from the right position of the sky at the right time, but the disadvantage is that the instrumental background does also depend on the position on the detector and the same region cannot be used both as background and source. To avoid this problem it is possible to use blank sky data which is a collection of observations of “X-ray empty” regions in the sky where there are no known X-ray sources. In this way the background can be taken from the right position on the detector, but there is no guarantee that the background of the blank sky data is similar to the background in the direction of the observed source at the given time [64]. Modelling the background is almost pure guessing, so neither does this provide a perfect method for background subtraction. Luckily we do not need to worry too much about the background subtractions in order to constrain decaying dark matter particles. We just include all the received flux in a very conservative upper limit on the flux.

The galactic halo is dark matter dominated and the observed mass of the halo (see Sec. 6.2) will contribute to the flux of possible decaying dark matter. We have estimated the mass of dark matter particles in the Milky Way halo (see Sec. 8.2) and their mean distance and included this mass as a possible flux source in the further calculations and model comparisons.

## 5.7 Determining the flux from spectral model comparison

For X-ray observations it is not possible to remove the instrumental effects (arf and rmf files) and compare the unfolded spectrum with a model spectrum in order to extract information about the observed object, because the instrumental response is not an analytical function. Instead a model is convolved with the instrumental effects before it is fitted to the spectrum in units of “normalized counts per instrument energy channel” and the free model parameters are determined using  $\chi^2$ -statistics. The incoming flux can then be calculated from the model. As long as we are only concerned about the flux and do not try to derive any other physical quantities such as temperature or redshift from the model, the type of the model does not matter as long as it fits the data well. Xspec contains a lot of pre-defined models, which can also be accessed from Sherpa.

## 6 Where to Look for Decaying Dark Matter

As the mixing angle between the sterile and active neutrinos is very small, the decays are very rare and to look for the emission line, we need to look at a region where the number of sterile neutrinos is very large. On the other hand, the flux we receive from a given source is inversely proportional to the distance squared (Eqn. 19) so the distance should not be too large. In this section I present four types of observations of nearby dark matter dense regions of the Universe suitable for a search for decaying dark matter: Clusters of galaxies, the Milky Way halo, dark matter blobs in clusters of galaxies and grating data.

### 6.1 Clusters of galaxies

In Sec. 1.4 it was discussed how the dark matter was first observed in clusters of galaxies, so clusters are an obvious place to look for decaying dark matter particles. Unfortunately the clusters emit a lot of X-ray themselves from hot gas between the galaxies. In Sec. 7 it is shown how the observational field of view can be optimised by only regarding the outskirts of a cluster in order to get rid of some of the unwanted X-rays from the gas. This method has been applied to the cluster A383 seen in Tab. 3.



<b>A383</b>	
RA (2000)	$02^{\text{h}}48^{\text{min}}06.00^{\text{sec}}$
DEC (2000)	$-03^{\circ}29'30.0''$
Redshift, $z^{A383}$	0.1883
Luminosity distance, $D_L^{A383}$	900 Mpc
Temperature, $T^{A383}$	$(4.8 \pm 0.1)$ keV
Radius, $R^{A383}$	800 kpc
Mass, $M^{A383}$	$(3.1 \pm 0.3) \cdot 10^{14} M_{\odot}$

**Table 3:** *Left:* The central  $(3 \text{ arcmin})^2$  of the cluster A383 observed in optical wavelengths with the Canada-France-Hawaii Telescope [65]. *Right:* A383 data [66] and coordinates [58].

### 6.2 The Milky Way halo

In our own neighbourhood we have a region that is dark matter dominated: The Milky Way halo. The left part of Tab. 4 displays the galaxy M101 which is believed to be quite similar to the Milky Way. For most galaxies the rotation curve of the stars are fairly flat as shown in the left part of Fig. 20 indicating that galaxies have a dark matter halo as sketched in the right part of Fig. 20. It is possible

to study the X-ray emission of the halo by observing in any given direction with no known X-ray sources. These observations are called “blank sky” observations and are usually used for background subtraction in observations of more distant objects. If the halo consist of radiatively decaying dark matter particles, a decay line should be visible in the blank sky spectrum. This possibility is investigated in Sec. 8.



### The Milky Way

Mass, $M^{MW}$	$(1.0) \cdot 10^{12} M_{\odot}$
Scale radius, $R_s^{MW}$	21 kpc
Concentration, $C^{MW}$	12

**Table 4:** *Left:* The Milky Way-like galaxy M101 observed with the Hubble Space Telescope [13]. *Right:* Milky Way data [67].

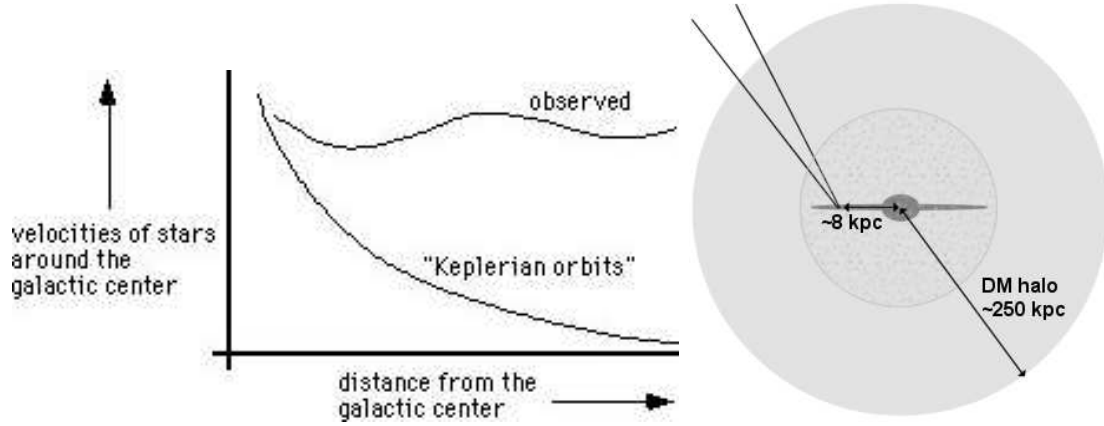


**Figure 20:** *Left:* The observed rotation curve of the Milky Way compared to the rotation curve we would observe if only the visible matter in the galaxy contributed to the Keplerian orbits. *Right:* A sketch of the Milky Way Halo demonstrating how we observe through the halo (not to scale.)

The best place to look for an emission line in the galactic halo, would be the dwarf galaxies accompanying the Milky Way because they are dark matter dominated and not very X-ray luminous [68, 69]. Unfortunately there are no X-ray observations of the Milky Way dwarf galaxies of sufficient exposure time available.

### 6.3 Dark matter blobs in clusters of galaxies

According to general relativity the space-time is curved by (large) masses and therefore the trajectory of light passing by large masses is bent. This is called gravitational lensing and can be exploited to map the mass distribution of foreground clusters along the line of sight to a distant bright light source. You distinguish between two different cases of gravitational lensing: The strong lensing where you get multiple image systems of a single bright background light source (normally a quasar) lensed by a foreground cluster and the weak lensing, where you analyse the weak distortions in the shape parameters of a galaxy population. The strong lensing is used to constrain the inner part of a cluster, where the weak lensing is used on larger scales.

The gravitational potential obtained from weak lensing compared to a *Chandra* X-ray image of the cluster of galaxies A520 shown in Fig. 21 reveals a difference between the matter distribution and the emission in a  $R \approx 200$  kpc region in the lower part of the image (in the yellow circle). The difference is not unique for A520 and these regions with high mass and low X-ray luminosity we have named “dark matter blobs.” As they contain lots of matter and are very X-ray faint, they are perfect for a search for decaying dark matter X-ray emission lines. In Sec. 9 the spectrum of the dark matter blob of A520 is analysed.



A520 blob	
RA (2000)	$04^{\text{h}}54^{\text{min}}19.00^{\text{sec}}$
DEC (2000)	$+02^{\circ}56'49.0''$
Redshift, $z^{\text{blob}}$	0.203
Luminosity distance, $D_L^{\text{blob}}$	980 Mpc
Temperature, $T^{\text{blob}}$	9.8 keV
Radius, $R^{\text{blob}}$	$\approx 200$ kpc
Mass of blob, $M^{\text{blob}}$	$3.16 \pm 1.27 \cdot 10^{13} M_{\odot}$

**Table 5:** *Left:* The central  $(2.83 \text{ arcmin})^2$  of the cluster A520 observed in optical wavelengths [70]. *Right:* A520 data [71] and coordinates [58].

### 6.4 Improving the resolution

When looking for a mono-energetic emission line hiding in an already line-full spectrum, the spectral resolution plays an important role. In Sec. 4.3 it was described how it is possible to improve the spatial resolution by deflecting the incoming X-ray photons in a grating, because their deflection angle depends sensitively on their energy. The cluster of galaxies A1835 has been observed with a grating and the extracted spectrum is analysed in Sec. 10.

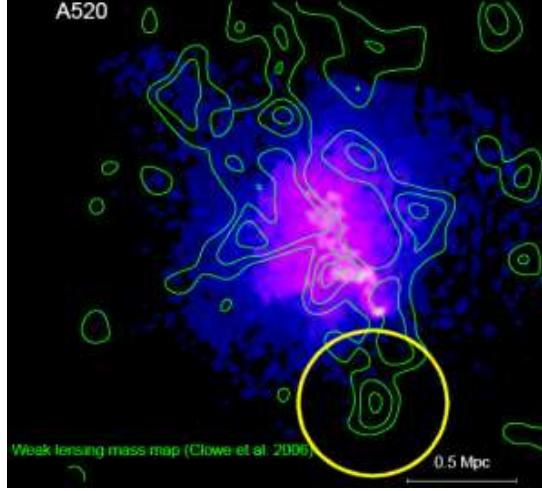
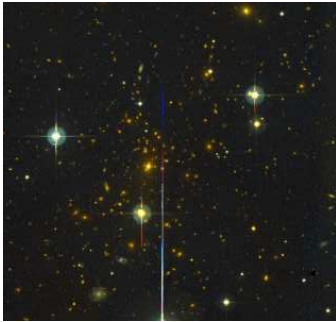


**Figure 21:** A *Chandra* X-ray image of A520 with the mass map derived from gravitational weak lensing overlaid. The dark matter blob is in the yellow circle [72].



### A1835

RA (2000)	$14^{\text{h}}01^{\text{m}}02.07^{\text{s}}$
DEC (2000)	$+02^{\circ}52'43.2''$
Redshift, $z^{A1835}$	0.252
Luminosity distance, $D_L^{A1835}$	1225 Mpc
Temperature, $T^{A1835}$	10 keV
Radius, $R^{A1835}$	800 kpc
Mass, $M^{A1835}$	$6.6 \cdot 10^{14} M_{\odot}$

**Table 6:** *Left:* The central  $(3 \text{ arcmin})^2$  of the cluster A1835 observed in optical wavelengths with the Canada-France-Hawaii Telescope [65]. *Right:* A1835 data [73, 74] and coordinates [58].

## 7 A383, A Cluster of Galaxies

In this section it is described how the signal to noise ratio can be improved by observing the outskirts of a cluster of galaxies, and the method is applied to the cluster A383.

### 7.1 Clusters of galaxies and their properties

Galaxies are not randomly distributed throughout the universe but instead most galaxies are found in collections called clusters (or groups if the number of members is less than  $\approx 50$ ). As far as known today clusters are the most massive bound systems in the universe that have reached a virial equilibrium [8]. Clusters generally have virial masses ranging from  $10^{13} M_{\odot}$  for groups up to a few  $10^{15} M_{\odot}$  for very rich clusters [8]. The matter of the galaxies does only account for a small part of a cluster. In between the galaxies is the intra-cluster medium (ICM), which contains a hot dilute gas emitting X-rays. The average temperature of the ICM is typically observed to be  $T \approx 0.3 - 15 \text{ keV}$  which corresponds to  $T \approx 10^7 \text{ K}$ .

### 7.2 Why A383 is a good cluster to observe

There are four important criteria to consider when selecting a cluster in which to look for a dark matter emission line. First of all it has to be observed and the data has to be accessible. The second criteria is that the distance to the cluster has preferably to be so that all of the cluster is contained within one *Chandra* pointing but not so far away that we receive too few photons to do statistical model fitting. For a cluster with a virial radius around  $R \approx 1000 \text{ kpc}$  the optimal distance is  $z \approx 0.15 - 0.25$ . The third criteria is that the cluster should be heavy in order to increase the mass within the field of view as the flux from decaying dark matter is proportional to the amount of dark matter (Eqn. 19). The last criteria to consider is the temperature of the cluster. The number of emission lines from a gas grows as the temperature falls so in order to reduce the number of lines in the spectrum originating in “standard” physical processes a relatively hot ( $T \approx 10 \text{ keV}$ ) cluster is preferred [75].

The cluster A383 is not very heavy nor very hot, as a mass of  $M^{A383} = 3.1 \cdot 10^{14} M_{\odot}$  [66] and a temperature of  $T^{A383} = 4.8 \text{ keV}$  [66] are typical average values for clusters. But it is observed with *Chandra* and with a redshift of  $z^{A383} = 0.1883$  [66] and an outer radius of  $R^{A383} \approx 800 \text{ kpc}$  it fulfils the first two requirements - even within the *Chandra* ACIS-S3 chip, and no cluster could be found that fulfilled all of the four criteria. The observation with observation identification 2321 consists of 19.76 ksec ACIS-S observations of A383. A longer observation time would increase the photon sensitivity.

### 7.3 Intra-cluster gas and the $\beta$ -model

The dominant baryonic matter component of a cluster is the hot intergalactic/intra-cluster gas [76]. A hot intra-cluster gas that is only supported against gravitational infall by its own pressure is described by the equation of hydrostatic equilibrium<sup>8</sup> which for spherical symmetry is given by [4]:

$$\frac{dP}{dr} = -\frac{GM_{tot}(< r)\rho_g(r)}{r^2}, \quad (55)$$

where  $P$  is the pressure of the gas,  $G$  is the gravitational constant,  $\rho_g(r)$  is the density of the gas, and  $M_{tot}(r)$  is the total mass inside a sphere of radius  $r$  including gas, stars, dark matter, spaceships, and what else hides in the universe.

The pressure of the gas is given by the perfect gas law:

$$P = \frac{\rho_g(r)T(r)}{\mu m_p}, \quad (56)$$

where  $T(r)$  is the temperature of the gas, and  $\mu$  is the mean molecular weight of the gas (not to be confused with the chemical potential,  $\mu_i$ ) in units of the proton mass,  $m_p$ . Combining Eqn. 55 and Eqn. 56 gives the total mass of everything in the cluster inside a given radius:

$$M(< r) = -\frac{T(r)}{G\mu m_p} r \left[ \frac{d \ln(\rho_g(r))}{d \ln(r)} + \frac{d \ln(T(r))}{d \ln(r)} \right]. \quad (57)$$

If the cluster is assumed to be isothermal and spherically symmetric, Eqn. 57 reduces to:

$$M_{tot}(< r) = -\frac{Tr}{G\mu m_p} \frac{d(\ln(\rho_g(r)))}{d(\ln(r))}, \quad (58)$$

where  $T$  is the characteristic temperature of the gas. Most clusters are not exactly spherical symmetric and consists of several components with different temperatures but comparisons between X-ray observations and simulations show that Eqn. 58 gives a good first order description of the average mass distribution despite the crude approximations. If the volume density of galaxies in a cluster follows a King profile [77, 78], then the density of an isothermal spherical gas cloud in hydrostatic equilibrium follows a  $\beta$ -profile [8]:

$$\rho_g(r) = \rho_0 \left(1 + (r/r_c)^2\right)^{-3\beta/2}, \quad (59)$$

where  $\rho_0$  is the gas density at  $b = 0$ ,  $r_c$  is the core radius defined as the radius at which the surface brightness is half its central value, and  $\beta$  describes the slope of the distribution at the radii  $r \gg r_c$ .

<sup>8</sup>The same equation describes the internal structure of a star where the inward force due to gravity is balanced by an outward force due to a pressure gradient.

The intensity of X-ray emission of a hot, tenuous, optically thin gas (which is a good description of ICM) scales as the square of the number density as all emission processes originate in collisions between two charged particles (electrons and ions) as for example bremsstrahlung. For the  $\beta$ -model the surface brightness as a function of the projected radius,  $b$ , is given by [8]:

$$S(b) = S_0 \left(1 + (b/r_c)^2\right)^{-3\beta+1/2}, \quad (60)$$

where  $S_0$  is the surface brightness at  $b = 0$ . The parameters  $\beta$ ,  $r_c$  are the same in Eqn. 59 and Eqn. 60 and can be found from fitting the observed surface brightness.

Even though the  $\beta$ -model is fairly simple and make some crude approximations 80% of all clusters are well fitted by it [8].

## 7.4 The NFW-profile

Another model for the distribution of dark matter haloes of galaxies and clusters, is the Navarro-Frenk-White (NFW) profile. As for the  $\beta$ -model the gas is assumed to be spherical symmetric and in hydrostatic equilibrium, so it is described by Eqn. 58. The generalized density distribution of the NFW-profile is given by [74]:

$$\rho_{DM}(x) = \frac{\rho_0}{x^\alpha(1+x^\gamma)^{(\beta-\alpha)/\gamma}}, \quad (61)$$

where  $x = r/r_s$ . The scale radius,  $r_s$ , is a free parameter. For a standard NFW-profile  $\alpha = 1.0$ ,  $\beta = 3.0$ , and  $\gamma = 1.0$ . The same values are adopted here. The density profile then becomes:

$$\rho_{DM}(x) = \frac{\rho_0}{x(1+x)^2}. \quad (62)$$

As the mass of a sphere is  $M(< r) = \int_0^r \rho_{DM}(r') 4\pi r'^2 dr'$ , the total mass inside  $r$  is given by integration [74]:

$$M_{tot}(< r) = 4\pi\rho_0 r_s^3 \left( \ln(1+x) - \frac{x}{1+x} \right) \quad (63)$$

In Fig. 22 the dashed line shows the NFW profile described above fitted to data points obtained for the cluster A1835 from X-ray analysis. The vertical solid line is the best fit scale radius,  $r_s$ , with the  $1\sigma$  values as the vertical dotted lines. The arrow marks the best fit scale radius for a fit to a more complicated model shown as the solid line, but as it is seen A1835 is almost as well fitted by the NFW-profile. The green square is the gravitational lensing mass [79]. In the lower part of Fig. 22 the gas mass fraction is shown.

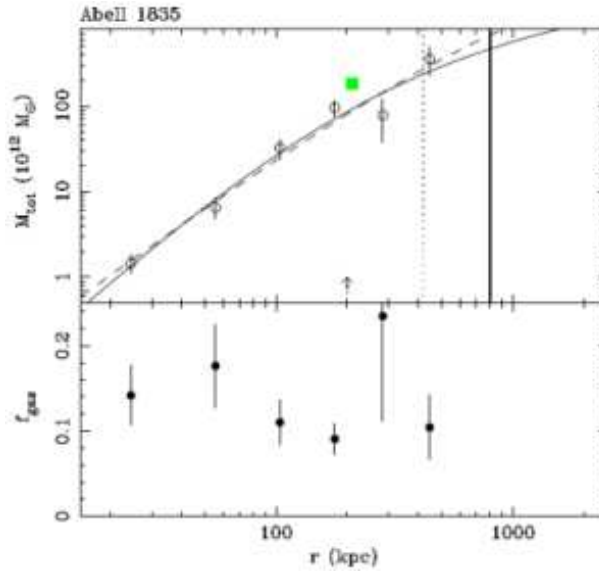


**Figure 22:** *Upper:* The density profile of A1835 fitted to a NFW-profile (dashed) and a more complicated model (solid). The vertical solid line is the best fit scale radius,  $r_s$ , for the NFW-profile with the  $1\sigma$  values as the vertical dotted lines. The arrow marks the best fit scale radius for the more complicated model. The green square is the gravitational lensing mass given by [79]. *Lower:* The gas mass fraction. [74].

## 7.5 Optimising the observational field of view

It is possible to optimize the ratio of the signal from decaying dark matter particles to noise (X-ray from ICM) by choosing the observation radius of a given cluster with care. The intensity of X-ray radiation from ICM is proportional to the ICM electron density squared because all emission processes origins in collisions between two charged particles. The intensity of X-ray radiation from decaying particles is directly proportional to the dark matter density; the more dark matter particles, the larger a probability that one will decay at a given time. As the ICM density and the dark matter density both depends on the radius, there exist an annulus around the cluster for which the ratio of signal to noise is maximal for a given dark matter distribution. This means that the ratio of signal to noise can be maximized by maximizing the ratio  $\Sigma(b)/S(b)$ , where  $\Sigma(b)$  is the mass per observed surface unit as a function of projected radius,  $b$ , and  $S(b)$  is the surface of brightness of the cluster in X-ray. If the density of the ICM is assumed to follow a  $\beta$ -profile,  $S(b)$  is given by Eqn. 60.

In order to calculate  $\Sigma(b)$  the distribution of all matter in the cluster (taken to

be equal to the mass of dark matter),  $\rho_{DM}$ , is needed [80]:

$$\Sigma(b) = \int_0^R \frac{\rho_{DM}(r)}{\sqrt{r^2 - b^2}} dr^2, \quad (64)$$

where the upper integration limit,  $R$ , is the chosen outer radius of the cluster.

The total mass inside a given radius,  $M_{DM}$ , can be calculated from Eqn. 67 for an ICM density distribution given by the  $\beta$ -profile (Eqn. 59):

$$M_{tot}(< r) = \frac{3\beta T}{G\mu m_p} \frac{r^3}{r^2 + r_c^2}, \quad (65)$$

The total density,  $\rho_{DM}$ , can then be found from:

$$M_{tot}(< r) = 4\pi \int_0^r \rho_{DM} r^2 dr. \quad (66)$$

In practice  $S(b)$  and  $\Sigma(b)$  are not observed at a single radius, but rather as a mass,  $M_{ann}$ , and a flux,  $F_{ann}$ , of an annulus of a certain width. The total mass and flux of an annulus with inner radius  $b_1$  and outer radius  $b_2$  are given by:

$$M_{ann} = \int_{b_1}^{b_2} 2\pi \Sigma(b) b db, \quad F_{ann} = \int_{b_1}^{b_2} 2\pi S(b) b db. \quad (67)$$

It is necessary to set some kind of criteria for selecting  $b_1$  and  $b_2$ . The first criterion is of course that they should both lie within the observational field of view and preferably within a single chip. Another criteria is that most of the ICM X-ray ‘‘noise’’ should be avoided but the annulus should still be fairly large in order to get enough photons to do statistical calculations. The values of  $b_1$  and  $b_2$  can be chosen from the values of the ratio of  $M_{ann}/F_{ann}$ . It was calculated in a tiny annulus of width a  $2\Delta b$  around the optimal radius,  $(b_{opt} - \Delta b, b_{opt} + \Delta b)$  and  $b_1$  and  $b_2$  were chosen so that the ratio of  $M_{ann}/F_{ann}$  becomes some fractional value of the ratio in the tiny annulus:

$$\frac{M_{ann}(b_{opt}, b_{opt} \pm b_{1,2})}{F_{ann}(b_{opt}, b_{opt} \pm b_{1,2})} = x_{1,2} \frac{M_{ann}(b_{opt} - \Delta b, b_{opt} + \Delta b)}{F_{ann}(b_{opt} - \Delta b, b_{opt} + \Delta b)} \quad (68)$$

where  $x_{1,2}$  is the fraction of the value in the tiny annulus for  $b_1$  and  $b_2$  respectively.

The angular extension of the annulus can be calculated from Eqn. 11.

$$\Delta\theta = \frac{\Delta b}{D_A} = \frac{(b_2 - b_1)(1 + z)^2}{D_L}. \quad (69)$$

## 7.6 The optimised field of view for A383

The ratio  $\Sigma(b)/S(b)$  as a function of  $b$  was determined numerically for a couple of clusters with an IDL routine. As input the routine takes the mass at a given radius,  $M(r_K) \pm \sigma_M$ ,  $r_K \pm \sigma_K$ ,  $r_c$ ,  $R$ ,  $\beta$ ,  $z$  and  $D_L$ . The input values were taken from Vikhlinin et al. [66]. As output it returns the optimal projected radius;  $b_{opt} \pm \sigma_b$ , the inner and outer radii of the annulus;  $b_1$ ,  $b_2$  and the mass of the annulus  $M_{ann}(b_1 < b < b_2) \pm \sigma_M$ . Fig. 23 shows  $S(b)$  (dotted),  $\Sigma(b)$  (dashed) and the ratio  $\Sigma(b)/S(b)$  (solid), scaled to their values at  $b = 0$  for the cluster A383. The general result was that  $b_{opt}$  lied in the outer half of the cluster at around 80% of the outer radius.

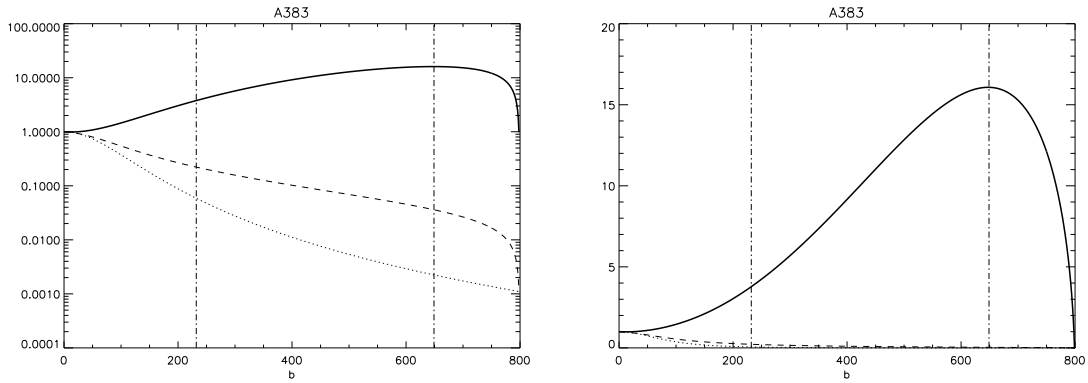


**Figure 23:**  $S(b)$  (dotted),  $\Sigma(b)$  (dashed) and the ratio  $\Sigma(b)/S(b)$  (solid), all scaled to their value at  $b = 0$  for A383. The optimal annulus is for  $b = (230 - 650)$  kpc =  $(1.3 - 3.5)$  arcmin. *Left:* Logarithmic scale. *Right:* Linear scale.

Input [66]		Output	
$r_K \pm \sigma_K$	$956 \pm 33$ kpc	$b_{opt}$	$648 \pm 1$ kpc
$M(r_K) \pm \sigma_M$	$3.1 \pm 0.3 \cdot 10^{14} M_{\odot}$	$b_1$	$232$ kpc = $1.3$ arcmin
$r_c$	$115.2$ kpc	$b_2$	$648$ kpc = $3.5$ arcmin
$R$	$800$ kpc	$M_{ann}(b_1 < b < b_2)$	$1.3 \pm 0.1 \cdot 10^{14} M_{\odot}$
$\beta$	$0.583$		
$z$	$0.1883$		
$D_L$	$903.5$ Mpc		

**Table 7:** The input and output values for the IDL routine determining the optimized observation annulus for A383.

The input and output values for A383 are given in Tab. 7. For A383  $b_{opt}$  almost corresponds to the outer edge of the *Chandra* ACIS-S3 chip. Hence it was

chosen as the outer radius of the annulus,  $b_2$ .  $b_1$  was chosen by setting  $x_1 = 0.5$  in Eqn. 68. The obtained values of  $b_1$  and  $b_2$  has been plotted as vertical lines on Fig. 23 (dot-dashed) and as the green circles in in Fig. 24. The mass of the annulus was determined to be  $M_{ann}^{A383} = 1.3 \pm 0.1 \cdot 10^{14} M_{\odot}$ .

The Milky Way halo contribution (described in Sec. 8) from the annulus of field of view is  $M_{halo}^{A383} = \pi(b_2 - b_1)^2 / (60 \cdot 360 \text{ arcmin})^2 M_{halo} = 3.3 \cdot 10^4 M_{\odot}$  with  $b_1$  and  $b_2$  given in arcmin.

Other values of  $x_1$  and  $x_2$  were tested. If e. g.  $x_1$  was chosen as  $x_1 = 0.75$  instead of 0.5 in order to improve the signal to noise ratio, the annulus becomes too small and the lack of photons becomes significant.

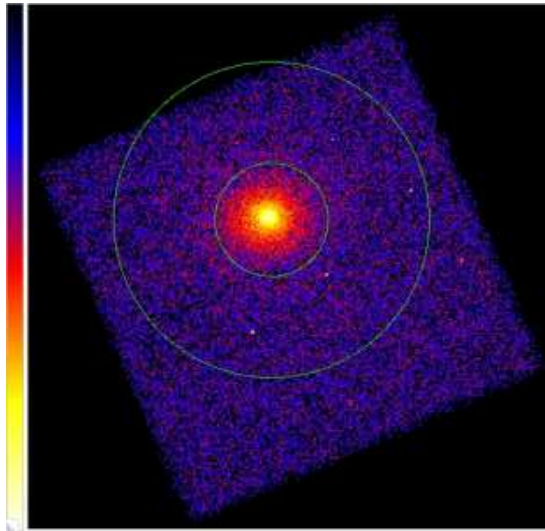


**Figure 24:** A383 observed with the *Chandra* ACIS-S3 chip and the optimal observation annulus. The ACIS-S3 chip is  $(8.1 \text{ arcmin})^2$ .

## 7.7 Uncertainty in optimal radius and mass of the annulus

The precision of the radii of the optimal annulus is not critical, as the annulus is only used for data selection and their uncertainties do not propagate to any final result. The critical uncertainty originating in the optimisation process, is that of the mass. In order to determine the uncertainty of the mass of the annulus the IDL routine calculates the mass of the annulus a 1000 times with different values of  $M(r_K)$  and  $r_K$  which clearly dominates the uncertainty in the mass estimate. The values are randomly picked from a Gaussian distribution of  $M(r_K)$  and  $r_K$  centred at the values given in [66] and a width of the given  $\sigma_M$  and  $\sigma_K$  respectively.

The total mass inside a given radius calculated from Eqn. 67 is a lower limit. The outer radius used as the upper integration limit in the integral defining the

surface density as a function of the projected radius (Eqn. 64) is taken to be either the radius, where the X-ray brightness is detected at more than  $3\sigma$  or the outer boundary of the *Chandra* field of view, whichever is smaller [66]. The actual outer radius of the cluster could actually be larger which would lead to an augmented density distribution and therefore result in a larger total mass of the annulus.

Recently the precision of the  $\beta$ -model has been investigated by Rasia et al. [81] who find that the  $\beta$ -model underestimates the cluster masses and the mass determined from Eqn. 67 certainly becomes a lower limit. This agrees with the fact that masses determined from gravitational lensing methods seem to be larger than X-ray determined masses.

### 7.8 Remark: Comparison to a modified $\beta$ -model

The model parameters from Vikhlinin et al. [66] are derived for an extended version of the  $\beta$ -model. It has been tested that using their parameters ( $\beta$ ,  $r_c$ ,  $R$ ) from the modified  $\beta$ -model in a non-modified  $\beta$ -model to determine the optimal radius gives optimal radii that only deviates about 5% from what is obtained using their full  $\beta$ -model. The conclusion is then to use a standard  $\beta$ -model, because it is simpler and  $b_{opt}$ ,  $b_1$  and  $b_2$  are only used for data selection.

### 7.9 Extracting spectrum of A383

The spectrum of A383 was extracted as described in Sec. 5 with the CIAO algorithm “spec\_extract” for the optimised annulus. The resulting spectrum is shown in Fig. 25. Over the interval  $E = 0.8 - 9.0$  keV it was fitted to a model consisting of an exponential, a powerlaw and two Gaussians with a reduced  $\chi^2 = 1.1$  for 226 degrees of freedom.

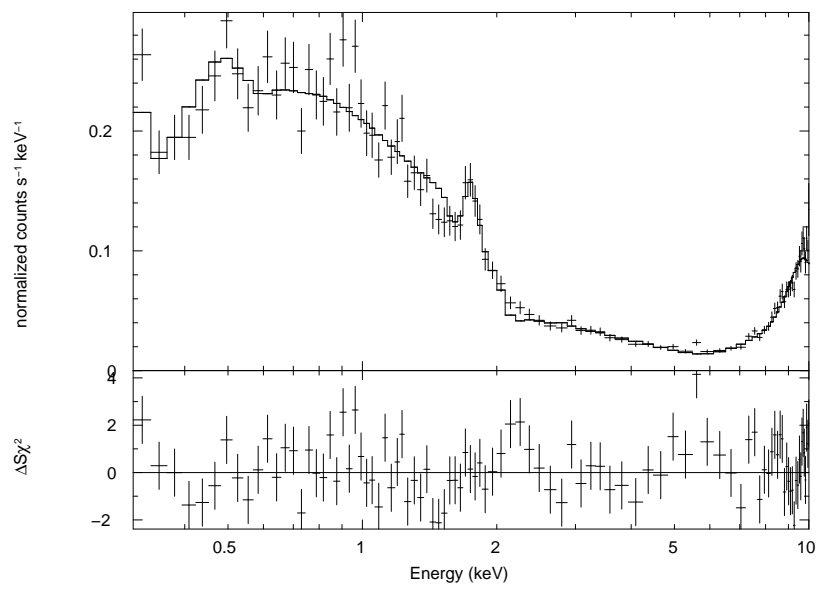


**Figure 25:** The raw spectrum of the optimised annulus of A383 fitted to a model consisting of an exponential, a powerlaw and two Gaussians.

## 8 The Milky Way Dark Matter Halo

The Milky Way halo is a nearby dark matter dense region suited for a search for decaying dark matter. In this section, the blank sky data are presented together with some characteristics of the Milky Way halo.

### 8.1 Blank sky data

As seen in Sec. 6.2 the Milky Way halo can be studied by analysing X-ray blank sky data. Blank sky data consist of many hours of observations of different regions of the sky with no known X-ray sources, that have been stacked. The ACIS-S3 part of the blank sky data set D2000-12-01 (Fig. 26), created during 2001, was analysed [64].

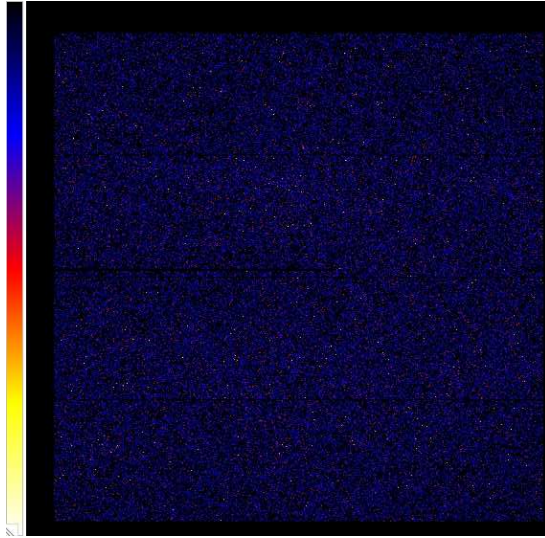


**Figure 26:** The ACIS-S3 blank sky observation from the *Chandra* blank sky data set D2000-12-01. No sources are clearly visible.

Sources identifiable by eye are already marked out in the creation of the blank sky data files, so no extra point source removal is needed. Also only good “non-flaring” time intervals have been used and all time stamps have been set to zero, so it is not possible to clean the light curve further [64]. The extracted spectrum is shown in Fig. 27 for  $E = (0.8 - 9.0)$  keV. A composite model consisting of a continuum of two power laws plus an exponential and with five Gaussians added at the energies of the most prominent lines, was fitted to the blank sky spectrum with a resulting reduced  $\chi^2 = 1.1$  for 540 degrees of freedom.

The background level of the ACIS-I chips is slightly lower than the background level of ACIS-S3 (see Fig. 35, [35]), but as we wanted to compare the blank sky

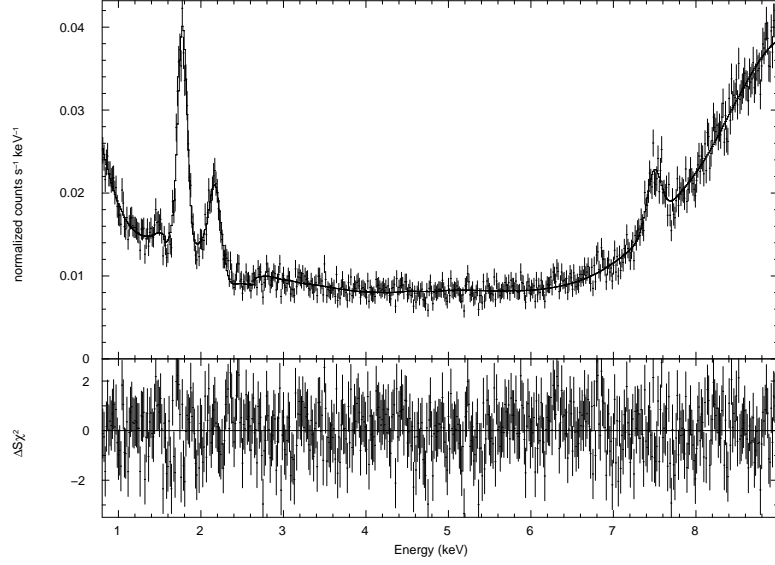


**Figure 27:** The blank sky spectrum of *Chandra* ACIS-S3 fitted to a model consisting of a two power laws, an exponential and five Gaussians.

spectrum with the spectrum of A383 observed with ACIS-S3 and look out for instrumental effects, it was decided to use blank sky data from the ACIS-S3 chip .

## 8.2 Observed halo mass and mean distance

The density distribution of the Milky Way is assumed to follow a NFW-profile which in the most general form is given by Eqn. 61:

$$\rho_{DM}(x) = \frac{\rho_0}{x^\alpha(1+x^\gamma)^{(\beta-\alpha)/\gamma}}, \quad (70)$$

where  $x = r/r_s$ . The standard values  $\alpha = 1.0$ ,  $\beta = 3.0$ , and  $\gamma = 1.0$  were adopted. It was tested that the total mass within the field of view does not depend sensitively on the values; varying the inner density slope,  $\alpha$ , from  $-1$  to zero or changing the outer density slope,  $\beta$ , between  $-3$  and  $-4$  changes the predicted mass by less than a factor of 2.

The total mass of the Milky Way halo was assumed to be  $M_{tot}^{halo} = 10^{12} M_\odot$  which is a rather conservative choice [67]. The scale radius and virial radius were taken to be  $r_s = 21$  kpc and  $r_{vir} = 256$  kpc respectively, and the solar distance  $R_\odot = 8$  kpc [67]. The average distance to the halo mass was determined to be

$D_L^{halo} = 0.035$  Mpc by integration of the density profile:

$$M_{tot}(< r) = \int_0^r \rho(r) 4\pi r^2 dr. \quad (71)$$

The fraction of the halo mass observed by the ACIS-S3 chip in the blank sky observations is  $M_{halo}^{blank} = (8.1 \text{ arcmin})^2 / (60 \cdot 360 \text{ arcmin})^2 = 1.4 \cdot 10^5 M_\odot$ .

## 9 The Dark Matter Blob of A520

The difference between the gravitational potential from weak lensing and an X-ray image reveals regions of large mass and low X-ray intensity. In this section the data analysis of one such region, called a dark matter blob, is discussed.

### 9.1 Extracting the spectrum of A520

The *Chandra* observation 4215 consists of 67.15 ksec observations of the cluster of galaxies A520 taken in the Very Faint mode described in Sec. 5.3. Before the data could be analysed, they had to be reprocessed in order to fully exploit the more precise event filtering of the Very Faint mode. The dark matter blob was identified with a circular region shown in red in Fig. 28 of radius  $r = 0.738$  arcmin and centre at the coordinates  $(RA, DEC) = (04^{\text{h}}54^{\text{m}}05.67^{\text{s}}, +02^{\circ}51'33.9'')$ . The two point sources within the region were removed manually. As seen by the red circles in Fig. 29 the dark matter blob is corresponding to a small group of very X-ray faint galaxies. The region is slightly shifted from the region with highest density because it has been defined from Fig. 21 and not from Fig. 29.

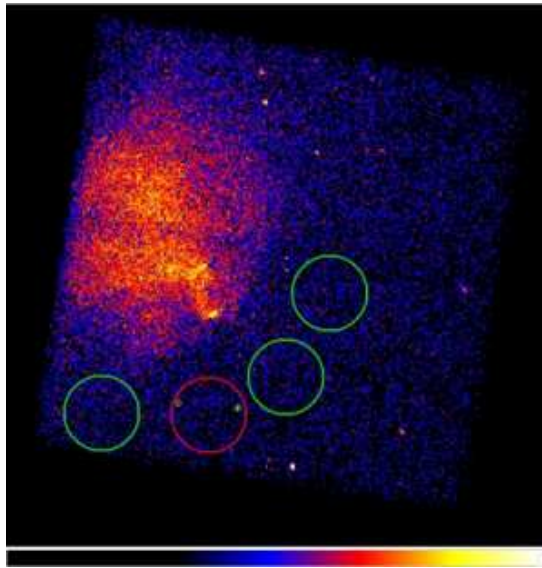


**Figure 28:** A520. The region in red is the dark matter blob for which the spectrum was extracted and the regions in green are the regions used for background subtraction. Compare to Fig. 21 or Fig. 29.

The extracted spectrum was fitted in the interval  $E = 0.3 - 9.0$  keV to a composite model of a power law and six Gaussians with a reduced  $\chi^2 = 1.2$  for 80 degrees of freedom. The spectrum and the fitted model are shown Fig. 30.

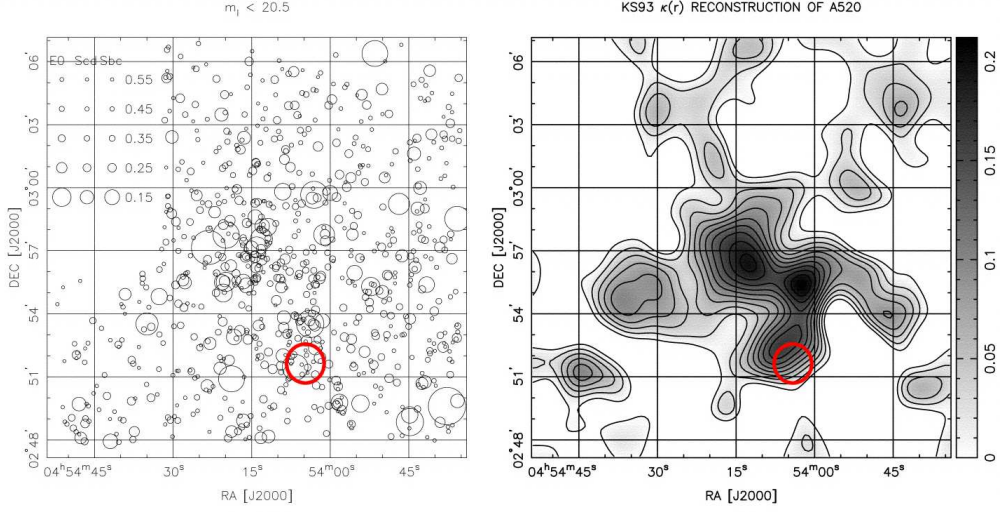


**Figure 29:** *Left:* The galaxies of A520. The size of the circle reflects the luminosity of the galaxy. The red circle is the region of the dark matter blob. *Right:* The surface mass density of A520 [82].

For A520 we tried to subtract the background in the form of some nearby regions with the same area but away from the dark matter blob. The spectrum subtracted the region to the left is shown in Fig. 31. The line feature just below 1 keV behaves like expected for a dark matter decay line. It shows up in the spectrum of a dark matter dense region (the blob) but not in the background from any of the nearby and less dark matter dense regions. However it is not a very significant effect. As seen in the right part of Fig. 31, the line does not show up in a similar spectrum from *XMM*.

## 9.2 The mass of the blob

The mass of the blob was determined from weak gravitational lensing by Håkon Dahle [83] to be  $M_{tot}^{blob} = 3.16 \pm 1.27 \cdot 10^{13} M_{\odot}$ . The halo contribution to the mass circular field of view is  $M_{halo}^{A520} = \pi r^2 / (60 \cdot 360 \text{ arcmin})^2 M_{halo} = 3.7 \cdot 10^3 M_{\odot}$  with  $r = 0.738 \text{ arcmin}$ .

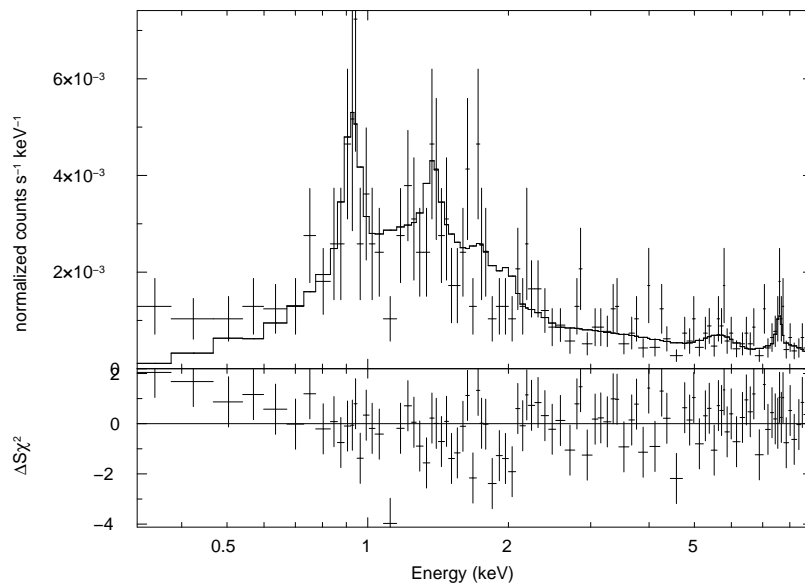


**Figure 30:** The spectrum of the A520 dark matter blob shown in Fig. 28 fitted to a model consisting of a power law and six Gaussians.

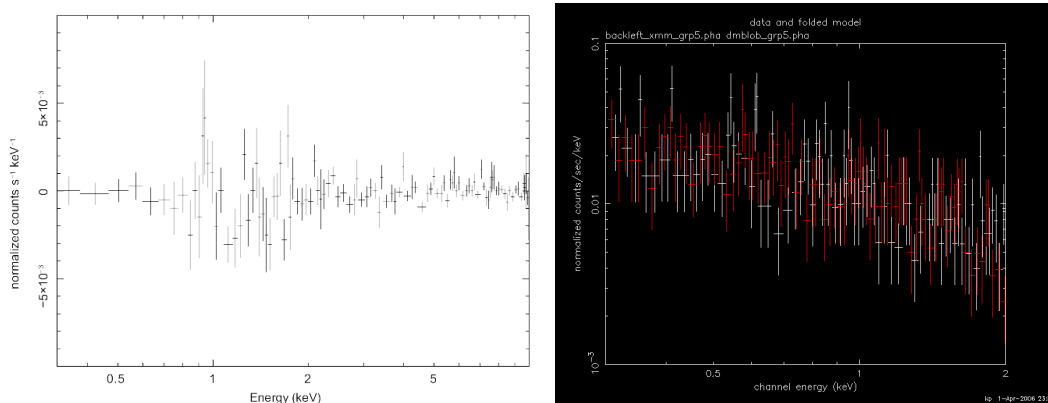


**Figure 31:** *Left:* The *Chandra* spectrum of the A520 dark matter blob subtracted the spectrum of the region to the left. *Right:* The *XMM* spectrum of the same region (white) and the background from the left region (red).

## 10 Grating Spectrum of A1835

The better the spectral resolution becomes, the better the chances of finding a specific emission line in the spectrum. The spectral resolution of *Chandra* can be significantly improved by employing a grating as described in Sec. 4.3. Unfortunately this method does only apply to bright point sources (or nearly point sources) as the spatial resolution of the arriving photons is lost, when they are deflected by the grating. Also it has to be a fairly bright source as some of the arriving photons are absorbed by the grating. In this section the data analysis of a grating spectrum of the cluster of galaxies A1835 is described.

### 10.1 The advantages of A1835

A1835 has a redshift of  $z^{1835} = 0.252$  which gives a luminosity distance of  $D_L = 1225$  Mpc [79, 84]. With an outer radius of  $R^{A1835} \approx 800$  kpc [73] it is reasonable to assume that all of the cluster mass lies inside the observational field of view of the 6 *Chandra* ACIS-S chips used in the observation 511. There are no other obvious mass sources in the field as seen in Fig. 32. This means that all of the observed flux can be taken to origin from A1835 and the Milky Way halo. The halo contribution is  $M_{halo}^{A1835} = 6 \cdot (8.1 \text{ arcmin} / (60 \cdot 360 \text{ arcmin}))^2 M_{halo} = 8.4 \cdot 10^5 M_{\odot}$  because there are six ACIS-S chips, each with an effective area of  $(8.1 \text{ arcmin})^2$ .

The mass distribution of A1835 has been investigated by Voigt and Fabian [74] who find that the cluster is well described by a standard NFW-profile (see Fig. 22). The total mass inside the full field of view has been calculated from Eqn. 63 with the best-fit parameters given in by Voigt and Fabian [74];  $r_s = 0.8_{-0.38}^{+1.59}$  and  $\rho_0 = 5.2 \pm 2.5 \cdot 10^{14} M_{\odot} / \text{Mpc}^3$ . This gives a total mass of  $M_{tot}^{A1835} = 6.6 \pm 2.7 \cdot 10^{14} M_{\odot}$  which is a mass in the heavier end of the cluster scale.

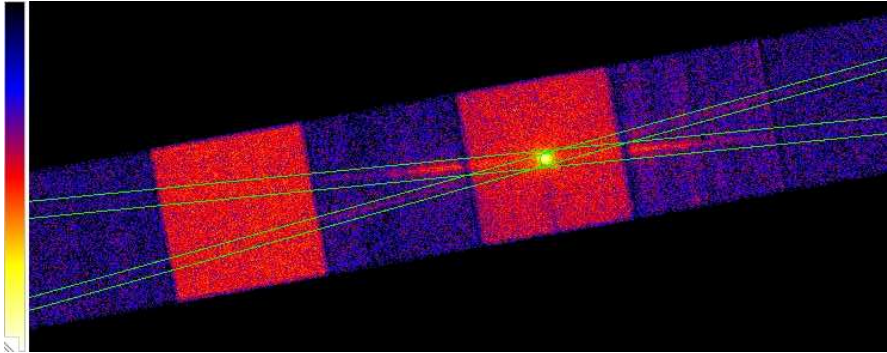


**Figure 32:** A1835 as observed with *Chandra*-HETG instrument. The green lines marks the deflected spectrum, and the circle is the zero order region.

## 10.2 Data treatment of A1835

The grating data of A1835 requires special treatment. The steps of the data analysis are briefly described here and for further details I will refer to the guide at the CIAO webpage [55].

Since the pipeline data treatment does not apply to grating spectra, it is necessary to reprocess the grating data manually. First the ACIS afterglow correction from the pipeline must be removed, because it is outdated and a better one is incorporated in CIAO. Then a new badpixel file is created and the data are reprocessed with the new badpixel file and the new afterglow correction applied. These first steps are not different from those of reprocessing normal data files. The next step is to locate the detector position of the zero order spectrum and the lines of deflected photons shown in Fig. 32. Then the data are reprocessed to a level2 file, which is in principle ready for light curve cleaning etc. If the ACIS-S4 chip was turned on during observations (which it is by default for grating observations), it is necessary to destreak the data from the chip in order to account for a defect in the serial readout of the chip causing “lines” in the image [55]. The *rmf* and *arf* files are created together with the spectrum and the data are split out in deflection orders before they can be regrouped and binned ready to be fitted to a spectral model.

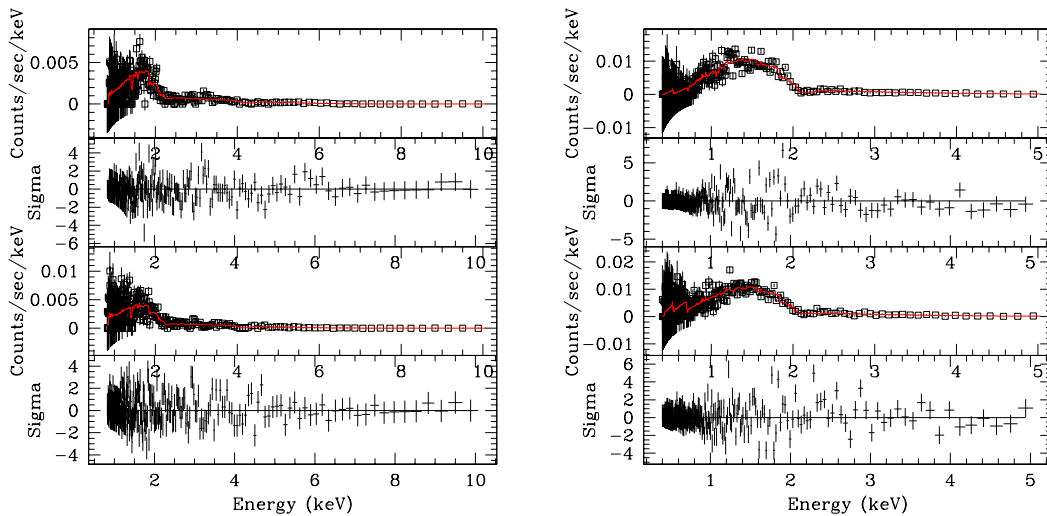


**Figure 33:** *Left:* The first order ACIS-HEG grating spectrum of A1835 with a fitted MEKAL model. *Right:* The first order ACIS-MEG grating spectrum of A1835 with a fitted MEKAL model.

The spectra of the first order deflection to both sides (called  $\pm 1$ ) are fitted simultaneously for the HEG and MEG data respectively. The model fitted to

the data is a MEKAL model [85], which is a plasma physics model describing the emission from a diffuse hot gas. The MEKAL model has the temperature, the metal abundance and the redshift as free parameters. The redshift was fixed at the known value and the parameter frozen before the model was fitted to the spectrum. The resulting fits shown in Fig. 33 have reduced  $\chi^2$  of  $\chi_{HEG}^2 = 1.2$  (683 degrees of freedom) for HEG and  $\chi_{MEG}^2 = 1.2$  (569 degrees of freedom) for MEG.

### 10.3 The zero order spectrum

The zero order spectrum consists of the photons that were not deflected by the grating and can be extracted from the zero order region by following the standard spectrum extraction procedure described in Sec. 5. For the observation 511, the zero order region (the green circle in Fig. 32) has a radius of 0.35 arcmin. The mass inside the field of view can be calculated from a NFW-profile (Eqn. 63) for the same parameters as in Sec. 10.1 giving a mass of  $M_{tot}^{zero} = 1.48 \cdot 10^{13} M_{\odot}$ . The halo contribution to mass inside the field of view is  $M_{halo}^{zero} = \pi(0.35 \text{ arcmin})^2 / (60 \cdot 360 \text{ arcmin})^2 M_{halo} = 8.2 \cdot 10^2 M_{\odot}$ .

Because it is a Very Faint mode observation, the background level is very low and the zero order spectrum is well fitted by a single MEKAL model with a reduced  $\chi^2 = 1.1$  for 594 degrees of freedom.

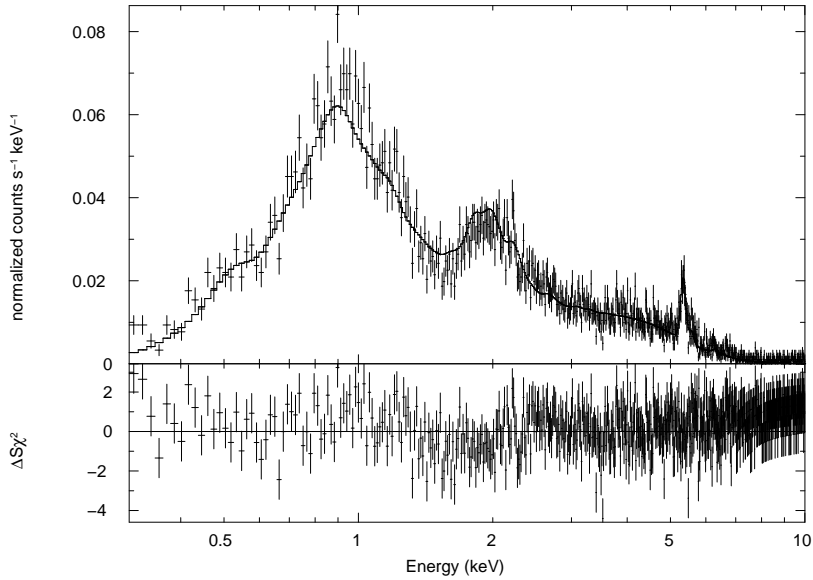


**Figure 34:** The zero order spectrum of A1835 with a fitted MEKAL model.

## 11 X-Ray Constraints on Sterile Neutrinos

With the spectra extracted from the different dark matter dense regions and fitted to models it is possible to determine the flux and constrain several parameters of the sterile neutrinos; the decay rate, the lifetime, the mass, the mixing angle and any additional entropy production.

### 11.1 Distinguishing between emission lines and spectral features

The extracted blank sky spectrum shown in the left part of Fig. 35 contains several very prominent line features. The right part of Fig. 35 shows the spectrum of a *Chandra* observation with the telescope stowed behind a lid and not pointing at the sky. As the lines are still visible, they must be of instrumental origin.

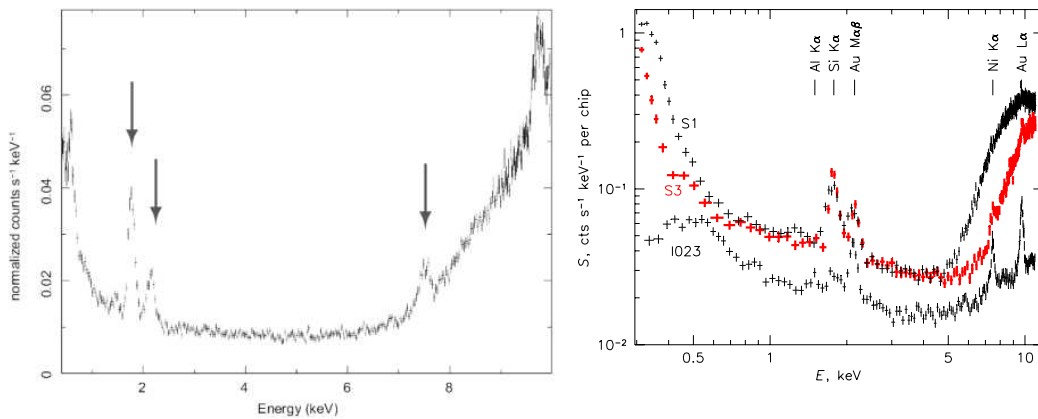


**Figure 35:** *Left:* The blank sky spectrum (see Sec. 8.1). *Right:* Energy spectra of the charged particle ACIS background with ACIS in the stowed position. Line features are due to fluorescence of material in the telescope and focal plane [35].

Most of the line features are identified since they originate from fluorescence of materials in the telescope and focal plane. However a decay line from dark matter could “hide” under one of these prominent features. In this case, the energy of the decay line will be redshifted by a factor of  $(1+z)$  in the spectrum of a dark matter region at a given redshift,  $z$ . To test for this, the blank sky spectrum was compared to those of the outskirts of the clusters A478 and A383 shown in Fig. 36. In the blank sky spectrum the line features at  $E_\gamma = 1.74$  keV,  $2.1 - 2.2$  keV, and  $7.47$  keV are identified as the Si  $K\alpha$ , the Au  $M\alpha\beta$  complex, and Ni  $K\alpha$  respectively.

For A487 with a redshift of  $z^{A478} = 0.0881$  [66], the lines would be redshifted to  $E_\gamma = 1.5$  keV, 1.8 keV, and 6.9 keV. As seen in the left part of Fig. 36 there are no obvious line features at these energies marked by the arrows. For A383 with  $z^{A383} = 0.1883$  [66], the lines would be redshifted to  $E_\gamma = 1.2$  keV, 1.7 keV, and 6.3 keV as shown in the right part of Fig. 36. There is a visible line at  $E_\gamma \approx 1.7$ , but this line is the original instrumental Si  $K\alpha$  line, so A383 is not suitable for checking whether there is an emission line hiding under the Au  $M\alpha\beta$  complex.

In the case where a moving line had been found in the spectra, it would not necessarily be an emission line from dark matter. It would probably origin in standard physical processes of the observed object as the redshifting of course applies to all emission lines.

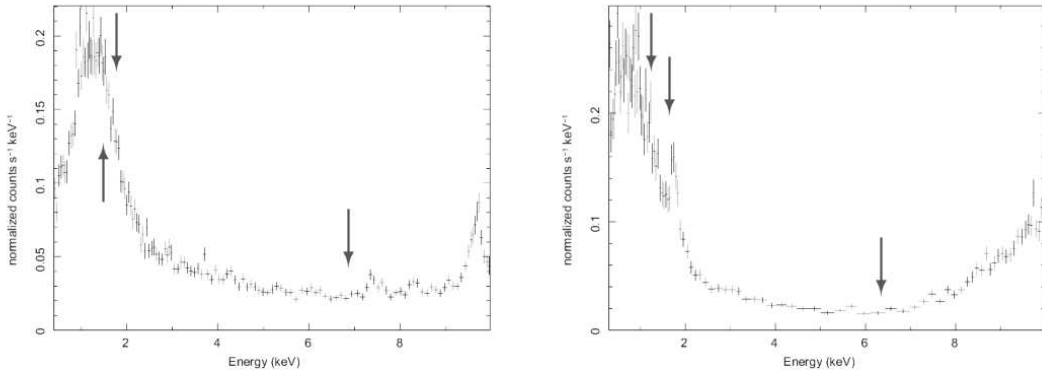


**Figure 36:** *Left:* The spectrum of the outer parts of A478 (only a fraction of the optimized annulus,  $b = 385 - 1150$  kpc) with the corresponding redshifted energies marked by arrows. *Right:* The spectrum of the outer parts of A383 ( $b = 230 - 650$  kpc) with the corresponding redshifted energies marked by the arrows.

## 11.2 A conservative upper mass limit from the total flux

The flux received by an X-ray observatory can be taken as an upper limit on the flux originating in decaying sterile neutrinos. The decay rate (Eqn. 20), the lifetime (Eqn. 14), and the branching ratio (Eqn. 16) can be combined with the expression for the mixing angle (Eqn. 46) and the proper conversion factors to give an upper limit for  $m_s$ :

$$\left(\frac{m_s}{\text{keV}}\right)^3 \lesssim 1.5 \cdot 10^{25} f(m_s) \left(\frac{A}{6.7 \cdot 10^{-8}}\right) \left(\frac{g_*}{15}\right)^{-3/2} \left(\frac{\Omega_{DM}}{0.26}\right)^{-1} \left(\frac{h}{0.71}\right)^{-2} \quad (72)$$

$$\times \left(\frac{F_{det}}{\text{erg/cm}^2/\text{sec}}\right) \left[\frac{(M_{fov}/M_\odot)}{(D_L/\text{Mpc})^2} + \frac{(M_{halo}/M_\odot)}{(D_{halo}/\text{Mpc})^2}\right]^{-1} \left(\frac{S}{1}\right)^{-1},$$

For the entire spectrum ( $E = 0.3 - 10$  keV) of the outer parts of A383, Eqn. 72 gives an upper limit of  $m_s \lesssim 20$  keV (for  $S = 1$ ) and similar results are obtained for the blank sky data and the dark matter blob of A520. The result is very conservative and robust since no background have been subtracted, no physical meaningful model is needed for the flux, and no information on the instrumental energy resolution is needed. Unfortunately this constraint is very close to the upper limit of the energy interval measurable by *Chandra* so it does not exclude very much.

### 11.3 Determining the emission line flux

As we are looking for a mono-energetic emission line it is not necessary to determine the flux from the entire energy interval. Instead it can be divided into a number of bins of a width comparable to the expected width of the emission line and the flux of each bin can be determined from a model describing the spectrum well from a statistical point of view. There are several ways to perform the division of the energy interval and the representation of the hypothetical mono-energetic emission line. The most conservative method is the “slice method” where the energy range of the spectrum is divided into bins of a width equal to the instrumental energy resolution ( $2\sigma$ ) and all of the X-ray flux in a particular bin (determined from the fitted model) is assumed to originate in decaying dark matter particles. Fig. 37 shows the blank sky spectrum fitted to a model with an energy “slice” at  $E_\gamma = 7.9 - 8.1$  keV. The slice method is very robust as it does not assume anything about the background, but regards all received flux as an upper limit for the flux from decaying dark matter even though the total flux is known to consist of several contributions; the CXB, the X-ray emission from the ICM, the Milky Way halo, and the instrumental background.

The fluxes obtained with the slice method are shown in Fig. 38 for A383 (solid yellow), the blank sky data (solid navy), the dark matter blob in A520 (solid green), and the grating spectrum of A1835 (solid red). It is clearly seen that the smallest fluxes are obtained for regions with very low X-ray background such as the blank sky data and the dark matter blob. By decreasing the bin-size, as done with grating spectrum of A1835, the flux per bin is also decreased.

Another method to determine the flux is to let a hypothetical mono-energetic emission line in the spectrum be represented by a Gaussian, centred at the line energy, with a width,  $\sigma$ , given by the instrumental spectral resolution, and with the maximum at the value of the model fitted to the broad-band spectrum. An example of such a Gaussian is shown in Fig. 37 at  $E_\gamma = 6.0$  keV. The flux determined by this Gaussian can be taken as an upper limit on the mono-energetic emission from decaying dark matter. As shown for the blank sky data in Fig. 39, the fluxes obtained by the two methods are very similar.

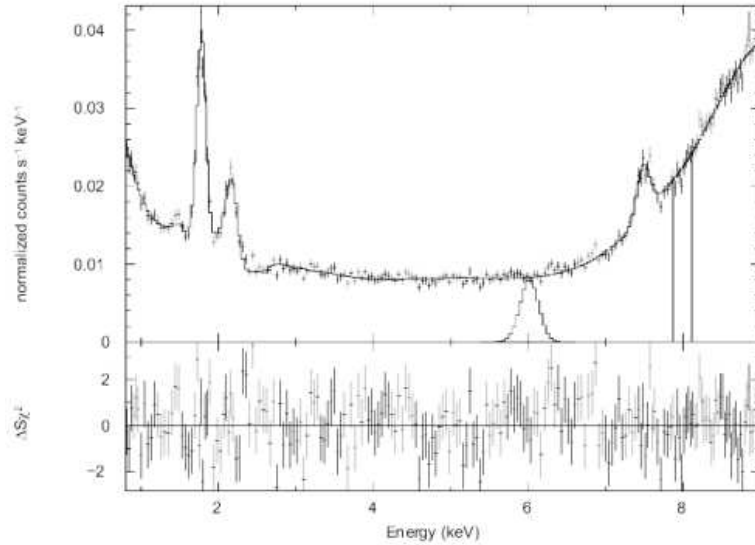


**Figure 37:** The blank sky spectrum fitted to two power laws, an exponential, and five Gaussians (reduced  $\chi^2 = 1.1$ ). At  $E_\gamma = (7.9 - 8.1)$  keV is shown a slice as used in the slice method, and at  $E_\gamma = 6.0$  keV is shown a Gaussian demonstrating the similar method.

The line broadening due to velocity dispersions in the observed dark matter halo is negligible compared to the spectral resolution of *Chandra* (even for grating spectra, Sec. 4.2). If it was not negligible, the width of the slice or the Gaussian should be determined by the broadening due to velocity dispersion and not by the instrumental spectral resolution.

The more photons received by *Chandra*, the more precisely the flux can be determined. The relative error on the flux determination is given by Xspec and Sherpa and for the relevant spectra it is of the order of  $\sigma_f/F_{det} \approx 0.1 - 0.2$  for models fitted with a reduced  $\chi^2$  of 1.1 – 1.4.

#### 11.4 A more model dependent limit on the flux

If the broad-band spectrum is fitted to a physical meaningful spectral model, e. g. the MEKAL model for clusters, it is possible to improve the upper limit of the flux by applying a “Gaussian method” where a hypothetical mono-energetic emission line in the spectrum is represented by a Gaussian, centred at the line energy, and with a width,  $\sigma$ , given by the instrumental spectral resolution (as before). This Gaussian is added to the previously fitted physical model and the composite model is again fitted to the data with the norm of the Gaussian as the only free

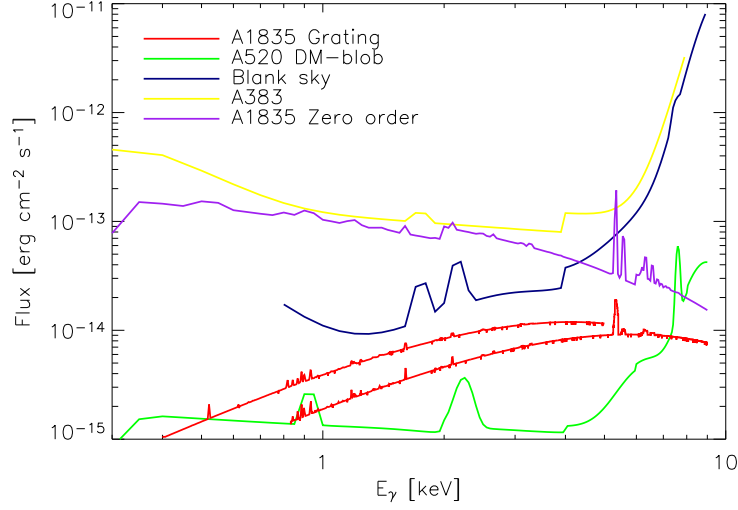


**Figure 38:** The fluxes obtained with the slice method for blank sky data (solid navy), A383 (solid yellow), A520 (solid green), A1835 grating (solid red), and A1835 zero order (solid purple).

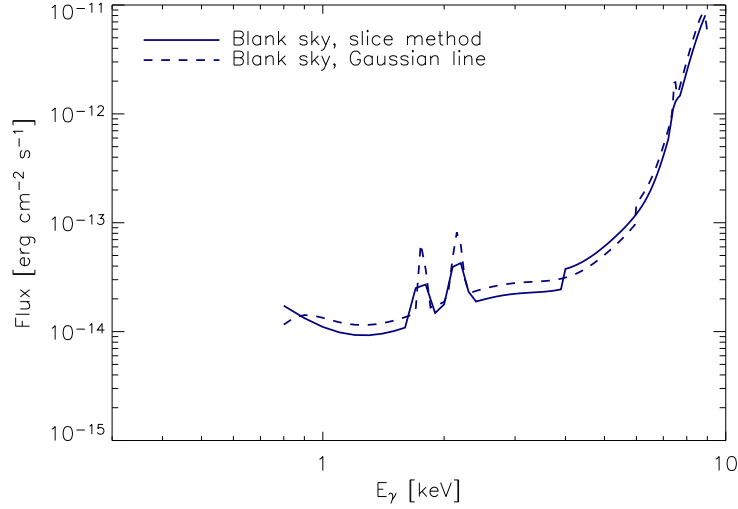


**Figure 39:** The flux obtained from the slice method (solid navy) and for the method with a Gaussian with maximum at the fitted base model (dashed navy) for the blank sky data.

parameter. The flux from the physical model is assumed to originate in standard physical processes, so the only flux, which could possibly originate in decaying

dark matter, is the flux between the physical model and the Gaussian<sup>9</sup>. Fig. 40 shows the flux from the Gaussian method applied to the grating spectrum of A1835 (solid blue) compared to the results obtained for the same data by the slice method (solid red).

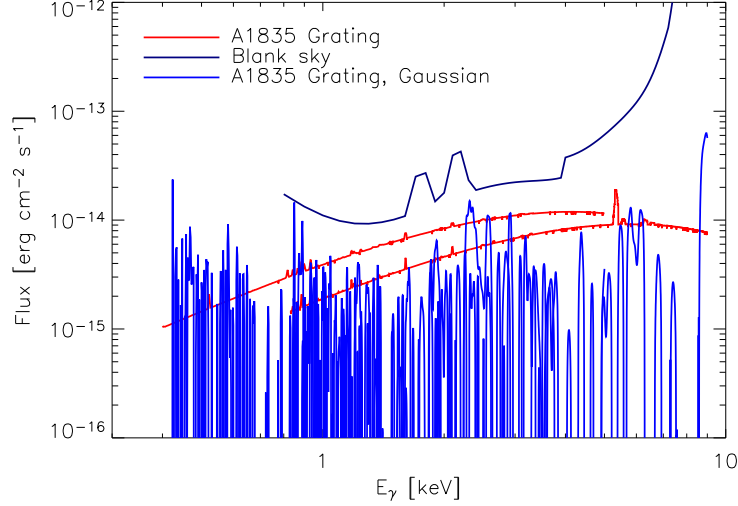


**Figure 40:** The fluxes obtained with the Gaussian method for A1835 grating (solid blue) compared to the fluxes obtained for the same data by the slice method (solid red).

There are small intervals where the flux observed by *Chandra* is zero, leading to a very low upper limit on the flux. Over most of the energy interval there is a quite good agreement between the slice method and the Gaussian method. The largest disagreement is for very low photon energies. It is due to the much higher instrumental background level (see the right part of Fig. 35) which makes it harder to fit the data well by the physical model at the low energies. Therefore it leaves room for a larger Gaussian within the data error bars when fitting the composite model.

In the following sections the flux limit has been obtained with the slice method, unless otherwise stated.

<sup>9</sup>The method is comparable to that of Boyarsky et al. [86] but not identical.

## 11.5 Constraining the decay rate of a dark matter particle

The observed upper limit of the flux can be used to set an upper limit on the radiative decay rate of a dark matter particle in the observed field of view (Eqn. 20):

$$\begin{aligned} \Gamma_\gamma &\lesssim 8\pi F_{det} \frac{D_L^2}{M_{fov}} \\ &= 1.34 \cdot 10^{-4} \left( \frac{F_{det}}{\text{erg/cm}^2/\text{sec}} \right) \left[ \frac{(M_{fov}/M_\odot)}{(D_L/\text{Mpc})^2} + \frac{(M_{halo}/M_\odot)}{(D_{halo}/\text{Mpc})^2} \right]^{-1}, \end{aligned} \quad (73)$$

Both the observed object and the Milky Way halo contribute to the mass within the field of view. The obtained constraints are shown in Fig. 41 for blank sky data (solid navy), A383 (solid yellow), A520 (solid green), A1835 grating (solid red), and A1835 zero order (solid purple).

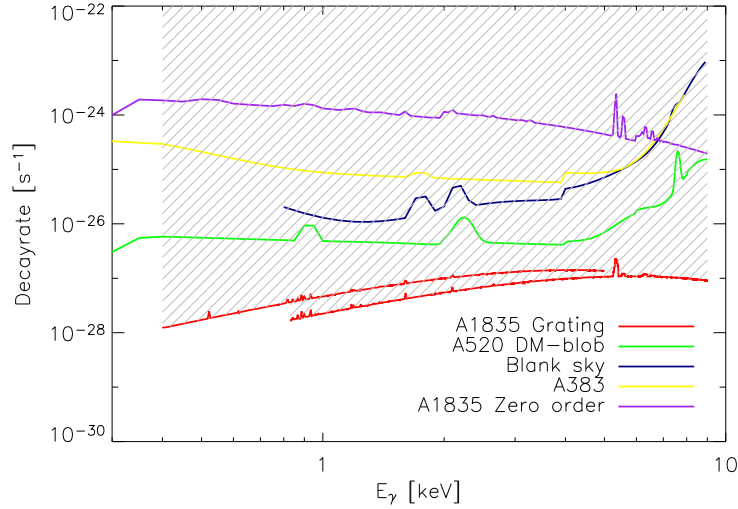


**Figure 41:** The constraints on the decay rate obtained with the slice method for blank sky data (solid navy), A383 (solid yellow), A520 (solid green), A1835 grating (solid red), and A1835 zero order (solid purple). The hatched region is excluded by Eqn. 73 applied to the A1835 grating data.

The fluxes are determined with an accuracy of  $\sigma_f/F_{det} \approx 0.1 - 0.2$ . The uncertainty in the distance and the mass are not uncorrelated, but they are both determined with an accuracy of  $\sigma_D/D_L \approx \sigma_M/M_{tot} \approx 0.1 - 0.3$ . The decay rate is directly proportional to the flux and the mass, but the dependency on distance is squared. Therefore the uncertainty of the distance dominates the total uncertainty of the decay rate. The values of the observed masses used to determine  $\Gamma_\gamma$  have all been chosen conservatively small and as  $\Gamma_\gamma \propto M_{fov}^{-1}$  the possibly larger masses

would just improve the obtained constraints. When all the uncertainties adds up, the uncertainty in the decay rate is still less than a factor of two and even though the result is not very precise, the order of magnitude is reliable.

The achieved upper limit on the decay rate is very general, as the only assumptions about the dark matter particle is that it has a radiative two-body decay.

The zero order spectrum of A1835 gives the weakest constraint on the decay rate confirming that observations of a full cluster is not the optimal method to constrain a decaying dark matter particle. If only the outer parts of a cluster is considered, as for A383, it is possible to gain an order of magnitude. The the grating spectrum of A1835 gives a constraint which is three to four orders of magnitude better than the zero order spectrum of A1835 even though the same cluster is observed. The improvement is due to the grating spectral resolution being approximately a factor of 50 better than the normal spectral resolution (Sec. 4.3).

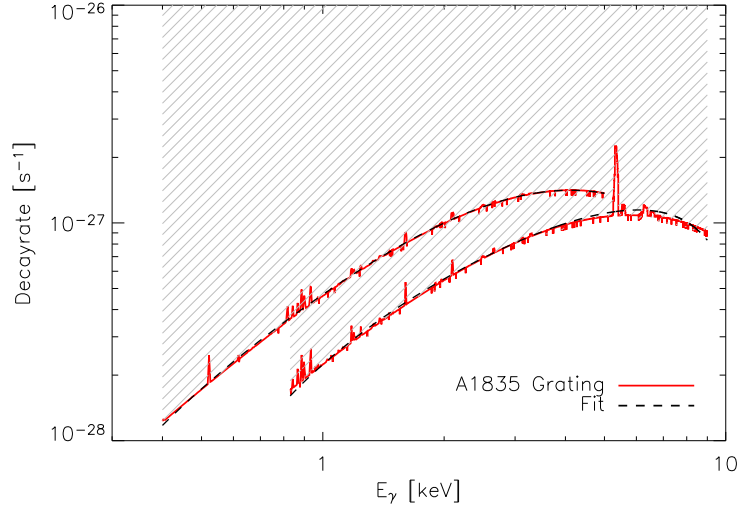


**Figure 42:** The decay rate constraint of the A1835 grating spectrum (solid red) fitted to a polynomial (dashed black) independently for HEG and MEG.

The decay rate constraints from the grating data of A1835 has been approximated by an analytical expression for HEG and MEG independently. As seen in Fig. 42 a second order polynomial describes the HEG constraints quite well, and a sixth order polynomial does the job for the MEG data:

$$\begin{aligned}
 \Gamma_{HEG} &= -1.78 \cdot 10^{-28} + 4.38 \cdot 10^{-28} E_{\gamma} - 3.61 \cdot 10^{-28} E_{\gamma}^2 \\
 \Gamma_{MEG} &= -7.08 \cdot 10^{-28} + 3.78 \cdot 10^{-28} E_{\gamma} + 2.91 \cdot 10^{-28} E_{\gamma}^2 \\
 &\quad -1.57 \cdot 10^{-28} E_{\gamma}^3 + 3.08 \cdot 10^{-29} E_{\gamma}^4 - 2.89 \cdot 10^{-30} E_{\gamma}^5 + 1.09 \cdot 10^{-31} E_{\gamma}^6
 \end{aligned} \tag{74}$$

## 11.6 Lifetime constraints and model confrontation

By using the branching ratio for the sterile neutrinos (Eqn. 16), the general dark matter X-ray constraints on the decay rate can be converted into constraints on the lifetime of the sterile neutrinos. The obtained constraints (shown in Fig. 43) can be compared to the  $\nu$ MSM model predictions for the lifetime (Eqn. 14) and mixing angle (the analytical solution, Eqn. 46) combined:

$$\begin{aligned} \tau_{model} = & 8.8 \cdot 10^{26} \text{ sec} \cdot f(m_s) \left( \frac{A}{6.7 \cdot 10^{-8}} \right)^{-1} \left( \frac{\Omega_{DM}}{0.26} \right)^{-1} \\ & \times \left( \frac{h}{0.71} \right)^{-2} \left( \frac{S}{1} \right)^{-1} \left( \frac{g_*}{15} \right)^{-3/2} \left( \frac{2E_\gamma}{\text{keV}} \right)^{-3}. \end{aligned} \quad (75)$$

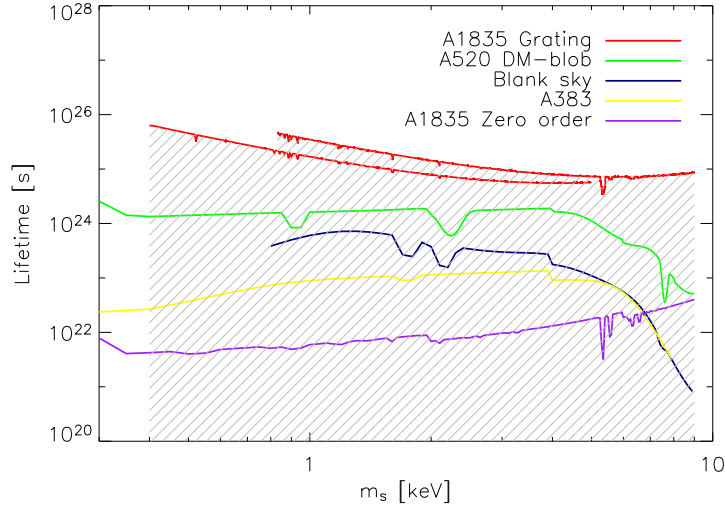


**Figure 43:** The constraints on the lifetime obtained with the slice method for blank sky data (solid navy), A383 (solid yellow), A520 (solid green), A1835 grating (solid red), and A1835 zero order (solid purple) as a function of mass.

In Fig. 44 the  $\nu$ MSM model predictions for several values of  $g_*$  and  $S$  (black) has been plotted on top of the constraints from the grating spectrum of A1835 (solid red). Even though  $S$  has been predicted to lie between 1 and 100 [25, 26] values down to  $S = 0.2$  are included. This is done as a conservative approach accounting for all uncertainties of the models and the experimental constraints on the decay rate. The numerical uncertainty of Eqn. 75 is dominated by the uncertainty of the value of  $g_*(T_{produced})$ . As described in Sec. 3.1  $g_*$  is usually chosen between 10 and 20. In Fig. 44 Eqn. 75 is plotted for  $g_* = 10 - 20$  (black

hatched). It is seen that even though the difference is not very large, there is a difference of approximately a factor of two between these two outer limits. When comparing the lifetime calculated with the analytical solution of the Boltzman equation (Eqn. 46, black hatched) to the more complicated numerical solution including effects from the quark-hadron phase transition and other production mechanism at  $T_{QCD} = 170 \text{ keV}$  (Eqn. 49, solid orange), it is seen that for the considered mass range, the solutions are almost identical, and the mean difference lies in the chosen value of  $g_*$ . The conclusion is that both the theoretical model prediction of the lifetime and the observational constraint are only accurate within a factor of two, which in the most conservative case are accounted for by choosing  $S = 0.2$ .

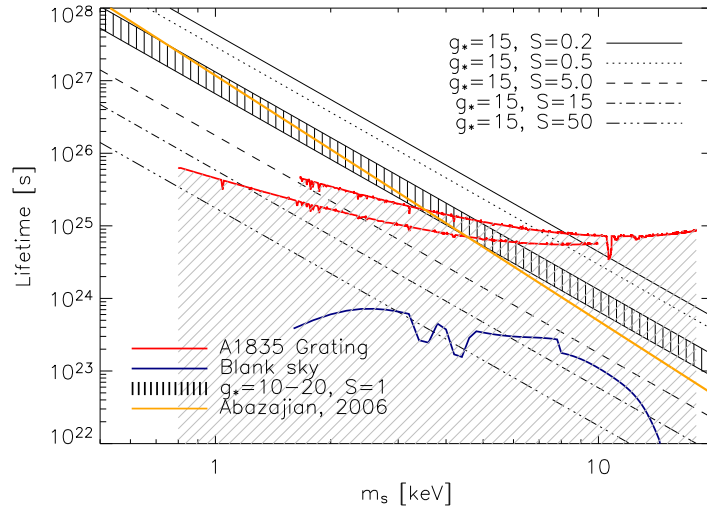


**Figure 44:** The blank sky (solid navy) and A1835 grating (solid red) constraints on the lifetime compared to the  $\nu$ MSM model predictions of Eqn. 75 for sterile neutrinos for several values of  $g_*$  and  $S$  (black), and the numerical model prediction of Abazajian [40] from Eqn. 49 (solid orange).

From the right part of Fig. 44 it is seen that the values of  $S \gtrsim 20$  are excluded, and for the most conservative choice of  $S = 0.2$ , an upper limit of the mass of the sterile neutrino is  $m_s \lesssim 8 \text{ keV}$ . For  $S = 1$  the limit becomes  $m_s \lesssim 3.5 \text{ keV}$ , and for  $S = 15$ ,  $m_s \lesssim 1.1$ .

If there are several dark matter components and the sterile neutrinos only contribute to a fraction of the total amount of dark matter, the upper mass limit changes. The change is shown as a function of fraction in Fig. 45 for the conservative choice of  $S = 0.2$  (solid red) and the standard choice of  $S = 1.0$  (dashed red) for the HEG grating spectrum of A1835. The lower the fraction of dark matter,

the weaker becomes the upper limit of the mass.

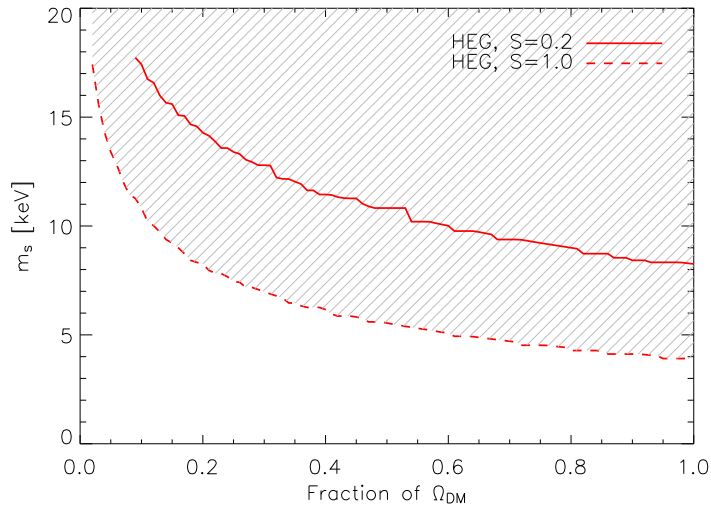


**Figure 45:** The mass limit as a function of the fraction of dark matter consisting of sterile neutrinos for  $S = 0.2$  (solid red) and  $S = 1.0$  (dashed red) for the HEG grating spectrum of A1835.

## 11.7 Constraining S

By comparing the lifetime constraints with the  $\nu$ MSM model predictions for several values of  $S$  (the right part of Fig. 43), it is possible to constrain the  $m_s - S$  parameter space as shown in Fig. 46 for the X-ray constraints presented in this report. It is seen that the general tendency is an exclusion of large values of  $S$  ( $S \gtrsim 20$ ) and large masses ( $m_s \gtrsim 10$  keV).

## 11.8 The $\sin^2(2\theta) - m_s$ parameter space

Constraints on the sterile neutrinos are often displayed in the  $\sin^2(2\theta) - m_s$  parameter space. Combining the decay rate (Eqn. 20) and the lifetime (Eqn. 14) with the branching ratio (Eqn. 16) the mass can be expressed as a function of the mixing angle without having to assume anything about the behaviour of the sterile neutrinos in the early Universe:

$$\sin^2(2\theta) \lesssim \sec^{-1} f(m_s) \left( \frac{F_{det}}{\text{erg/cm}^2/\text{sec}} \right) \times \left[ \frac{(M_{fov}/M_\odot)}{(D_L/\text{Mpc})^2} + \frac{(M_{halo}/M_\odot)}{(D_{halo}/\text{Mpc})^2} \right]^{-1} \left( \frac{m_s}{\text{keV}} \right)^{-5}. \quad (76)$$

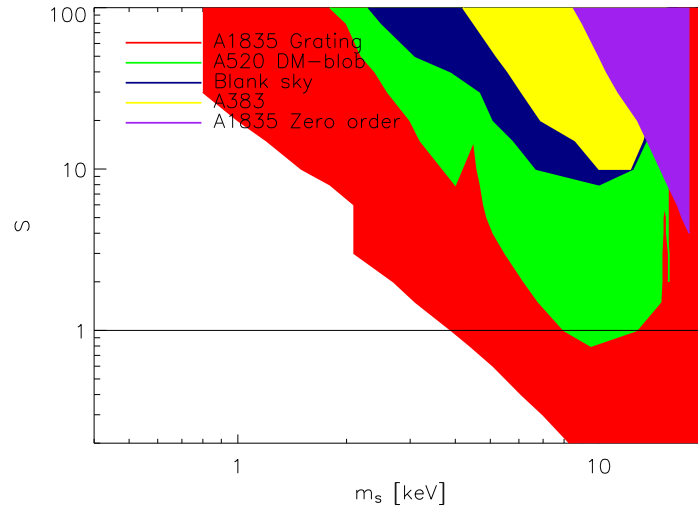


**Figure 46:** The  $m_s - S$  parameter space excluded by X-ray observations of blank sky data (navy), A383 (yellow), A520 (green), A1835 grating (red), and A1835 zero order (purple).

In Fig. 47 are shown the constraints presented in this report in the  $\sin^2(2\theta) - m_s$  parameter space. It is seen that large masses and large mixing angles are excluded. The uncertainty of the constraints is dominated by the uncertainty of mass and distance, and lies within a factor of two.

## 11.9 Improving the results

The uncertainties are dominated by those of the masses and especially by those of the distances. More precise mass and distance measurements would increase the quality of the constraints, but they would not change the quantitative conclusions very much.

The accuracy of the flux determination could be increased by stacking X-ray observations from different regions in order to improve statistics. Or, as mentioned in Sec. 6.2, X-ray observations of the dwarf galaxies within the Milky Way dark matter halo such as Draco or Ursa Minor could improve the constraints as the dwarf galaxies are believed to be dark matter dominated and X-ray faint [69]. None of these improvements would change the conclusions of the constraints significantly.

The constraints could be improved by observations at lower and especially higher energies than covered by the sensitivity of *Chandra*. The statistical errors and the flux determination can be improved by observations of longer exposure time.

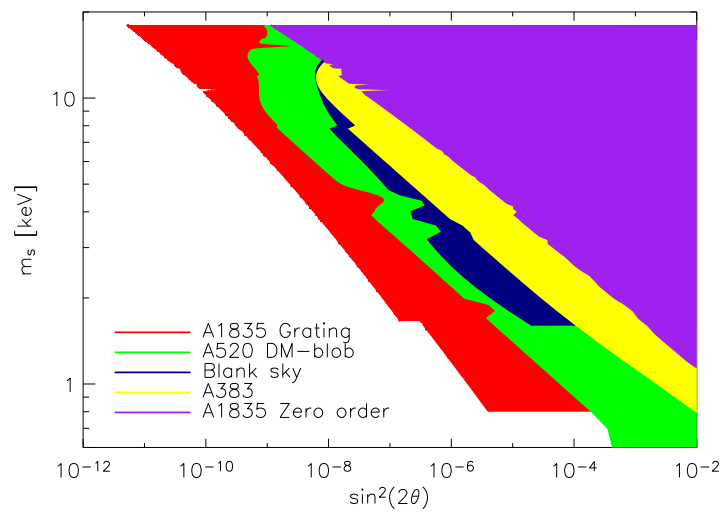


**Figure 47:** The  $\sin^2(2\theta) - m$  parameter space constrained from X-ray observations of the blank sky (navy), A383 (yellow), A520 (green), A1835 grating (red), and A1835 zero order (purple).

## 12 Comparison to Other Constraints

There are several constraints published on the sterile neutrinos both from X-ray and from independent methods of which the most important ones are presented briefly in this section. The results presented in the literature are often displayed in the  $\sin^2(2\theta) - m_s$  parameter space for sterile neutrinos of the Majorana type. As all the constraints presented in Sec. 11 are for Dirac type sterile neutrinos, they have to be converted to Majorana type constraints. As discussed in Sec. 2.4, Majorana particles are by definition their own antiparticles, and therefore they decay twice as fast. Constraints obtained for a Dirac particle on the  $\sin^2(2\theta) - m_s$  parameter space, are twice as restrictive when converted to constraints on Majorana sterile neutrinos.

### 12.1 The Tremaine-Gunn bound

Liouville's theorem, stating that the phase space density is conserved along particle trajectories in a collisionless fluid, provides a fundamental constraint on the clustering of warm particles [11, 68]. Studies of the available phase space for dark matter domination in dwarf galaxies by Tremaine and Gunn [68] leads to a very strong constraint on the mass of any dark matter particle. This limit of  $m \gtrsim 0.5 \text{ keV}$  is called the Tremaine-Gunn bound [87] and is plotted in black in the following figures.

### 12.2 Diffuse X-ray background

There are many different X-ray constraints on sterile neutrinos in the literature. In the following a brief outline of some of the recent results is given. Boyarsky et al. [88] searched for spectral cut-off features in the CXB from *XMM* (0.5 – 12.0 keV) and NASA's HEAO-1 (High Energy Astrophysics Observatory, 3.0 – 60.0 keV) observations. The resulting constraint in the  $\sin^2(2\theta) - m_s$  parameter space follows the trend:

$$\sin^2(2\theta) \lesssim 1 \cdot 10^{-5} \left( \frac{\Omega_{DM}}{0.26} \right)^{-1} \left( \frac{m_s}{\text{keV}} \right)^{-5}. \quad (77)$$

It is plotted in Fig. 48 in grey.

*XMM* observations of the clusters of galaxies Virgo and Coma was studied by Boyarsky et al. [86] who obtained the following constraint:

$$\sin^2(2\theta) \lesssim 7.74 \cdot 10^{-5} \left( \frac{m_s}{\text{keV}} \right)^{-5.43}, \quad (78)$$

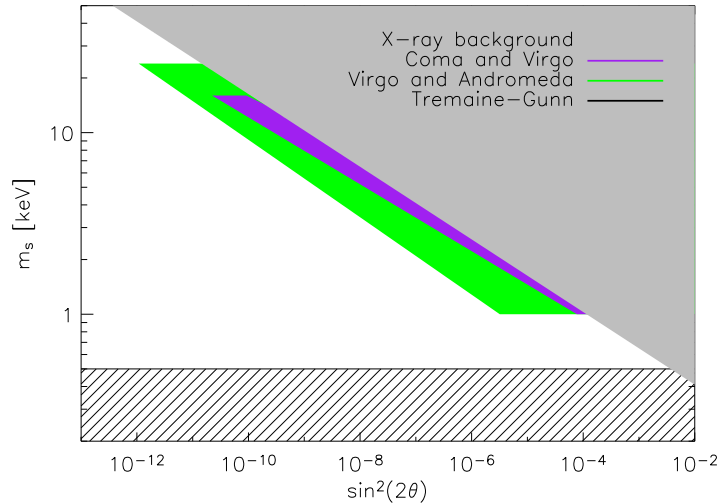


**Figure 48:** Constraints in the  $\sin^2(2\theta) - m$  parameter space for Majorana type sterile neutrinos from X-ray observations: CXB (grey) [88], the clusters Coma and Virgo (purple) [86], the galaxies Virgo and Andromeda (green) [90], and the Tremaine-Gunn bound (horizontal black) [68, 87].

which is plotted in Fig. 48 in purple. This constraint is not as conservative and robust as the similar results for clusters of galaxies presented in Sec. 11. The spectrum was modelled by a constructed composite model composed from elements chosen with physical arguments (continuum and emission lines) but in order for the model to fit the data. The base model was fitted to the data and then a Gaussian was added with increasing norm until the fit of the base model plus the Gaussian (to the data) was disturbed by a predefined value of  $\chi^2$ . The flux with a possible dark matter emission line origin was then determined from the difference between the base model and the Gaussian. The non-robustness lies within the modelling of the broad-band base model of the spectrum. When it was composed, all emission lines were modelled and a hypothetical mono-energetic emission line from decaying dark matter may already have been included in the base model, especially in the situation where the line has an energy close to the energy of instrumental or standard physical line features in the spectrum.

The sterile neutrinos were also constrained from cluster observations by Abazajian et al. [89], but the flux was underestimated by a factor of two and their strong claim on the upper mass limit is not reliable [86].

An independent analysis of *XMM* observations of the Milky Way halo by Boyarsky et al. [69] came to qualitatively the same conclusions as the blank sky constraints presented in Sec. 11 (and in [1]).

An analysis of galactic dark matter halos was performed by Watson et al. [90] using *XMM* observations of the galaxies Andromeda and Virgo (M87, the central galaxy in the Virgo cluster of galaxies). A hypothetical mono-energetic emission line was represented by a Gaussian with the line energy determined by the mass and the norm determined by the theoretically expected flux at that particular mass for a given value of  $\sin^2(2\theta)$ . For each value of the mass, the flux expected from the Gaussian as a function of increasing  $\sin^2(2\theta)$  was compared to the observed spectrum at the corresponding photon energy. The values of the mass and the mixing angle were fixed when the expected flux exceeded the observed flux by  $4\sigma$ . They obtained the following constraint:

$$\sin^2(2\theta) \lesssim 3.2 \cdot 10^{-6} \left( \frac{m_s}{\text{keV}} \right)^{-4.69}, \quad (79)$$

which is plotted in Fig. 48 in green.

### 12.3 The Lyman- $\alpha$ forest

All the X-ray constraints provide upper limits on the mass of the sterile neutrino, but lower limits on the mass also exist (which are more specific than the Tremaine-Gunn bound). As described in Sec. 1.5 the mass of a dark matter particle will influence the structure formation in the Universe, and different dark matter scenarios will lead to a difference in the structures observed today: A too light dark matter particle would erase all structures at small scales where a too heavy dark matter particle would yield too much structure. A map of the structure is an X-ray independent method to constrain the mass of a dark matter particle from below. A map of the clustering of hydrogen can be obtained from the Lyman- $\alpha$  forest (Ly- $\alpha$ ). The Ly- $\alpha$  emission line is the spectral line originating in a transition between the two lowest energy states of the hydrogen atom ( $n = 2, n = 1$ ). Ly- $\alpha$  light emitted from very bright distant sources (usually quasars) will pass through hydrogen clouds, where it will be absorbed by the atoms. The excited atoms will eventually re-emit the photons over the entire solid angle. Therefore we observe an absorption at the Ly- $\alpha$  line energy corresponding to the redshift of the hydrogen cloud. The Ly- $\alpha$  absorption lines from clouds at different distances will be redshifted by different amounts leading to a “forest” of Ly- $\alpha$  lines in the quasar spectra (see Fig. 49). The dark matter density distribution is assumed to follow that of the gas down to the scale, where the gas becomes pressure supported.

The matter power spectrum is defined as the mean square amplitude of the Fourier components of the density fluctuation field i. e. it describes the density fluctuations. The power spectrum can be modelled as a function of the mass and interactions of a given dark matter particle by numerical simulations and can be compared to the observed mass distribution to constrain the mass of the particle.

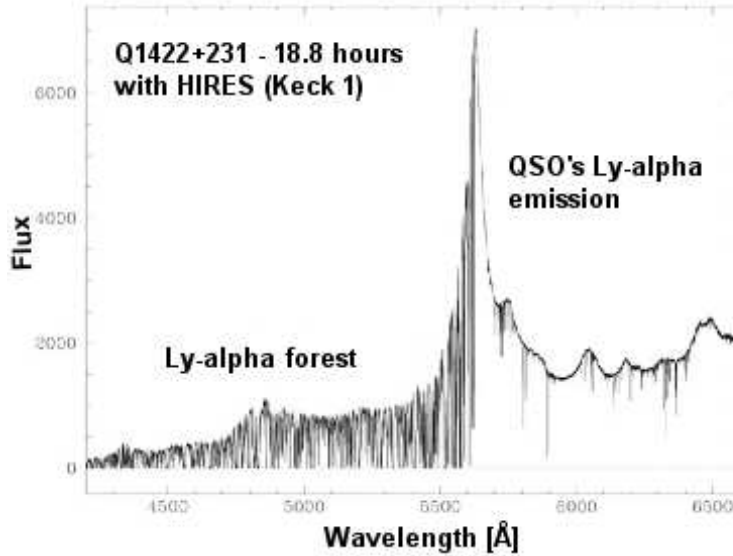


**Figure 49:** A spectrum of the quasar Q1422+231 observed with the Keck 1 Telescope. The peak around  $5600\text{\AA}$  is the Ly- $\alpha$  emission from the quasar and for shorter wavelengths the absorption line forest is clearly visible [92].

The drawback of the method is, that it is indirect as it only probes the macroscopic clustering signatures of a dark matter particle. Furthermore it requires interpretation of simulations at their resolution limit [46, 91].

Narayana et al. [93] compared the flux power spectrum (defined similarly to the matter power spectrum) and flux probability distribution of a small sample of “low redshift high resolution” quasar absorption spectra to the matter power spectrum obtained from numerical dark matter simulations assuming a linear relation between the two power spectra. In this way they were able to constrain the mass of any WDM particle (produced in thermal equilibrium) to be  $m \gtrsim 0.75\text{ keV}$ . Later the limit was improved to  $m_s \gtrsim 2.0\text{ keV}$  for sterile neutrinos by Viel et al. [94] by using the linear dark matter power spectrum inferred from two large samples of “low redshift high resolution” quasar absorption spectra and state-of-the-art hydrodynamical simulations combined with CMB data from WMAP.

A recent analysis of a large sample of “medium redshift low resolution” quasar absorption spectra by Seljak et al. [95] came to the surprising result  $m_s \gtrsim 14\text{ keV}$ , later confirmed by Viel et al. [96], who performed an independent analysis and modelling of the same data set to obtain a limit of  $m_s \gtrsim 10\text{ keV}$ .

In the following figures the Ly- $\alpha$  constraints are plotted in cyan and blue.

## 12.4 All constraints

In Fig. 50 the exclusions in the  $m_s - S$  parameter space are shown for the Tremaine-Gunn bound (horizontal black), the Ly- $\alpha$  bound of  $m_s \gtrsim 2.0$  keV [94] (vertical blue), the Ly- $\alpha$  bound of  $m_s \gtrsim 14$  keV [95] (diagonal cyan), and the grating spectrum of A1835 (solid red). (Remember  $m_s S^{1/3} \propto \text{const}$ , Eqn. 47). It is seen that if all constraints are applied, there is no parameter space left open for masses in the 0 – 20 keV range and  $S = 0.2 - 100$ .

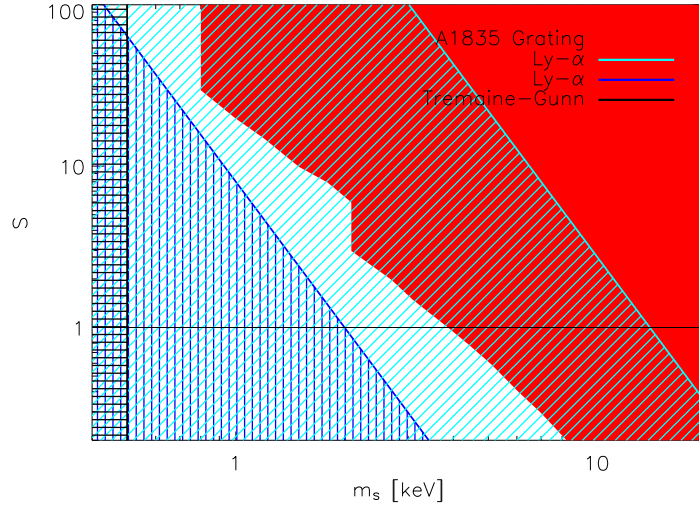


**Figure 50:** The constraints in the  $m - S$  parameter space of the Tremaine-Gunn bound (horizontal black), the Ly- $\alpha$  of [94] (vertical blue), the Ly- $\alpha$  of [95] (diagonal cyan), and the grating spectrum of A1835 (solid red).

In Fig. 51 the excluded areas in the  $m - \sin^2(2\theta)$  parameter space are shown for the Tremaine-Gunn bound (horizontal black), the Ly- $\alpha$  bound of  $m_s \gtrsim 2.0$  keV [94] (vertical blue), the Ly- $\alpha$  bound of  $m_s \gtrsim 14$  keV [95] (diagonal cyan), the CXB (solid grey) [88], the clusters of galaxies Virgo and Coma (solid purple) [86], the galaxies of Virgo (M87) and Andromeda (solid green) [90], and the grating spectrum of A1835 (solid red). It is seen that the A1835 grating spectrum constraint is among the best X-ray constraints, even though it is very conservative and robust. There is not much room left in the parameter space, if all the constraints are applied. Only very small mixing angles  $\sin^2(2\theta) \lesssim 10^{-11}$  and large masses  $m_s \gtrsim 14$  keV are allowed.

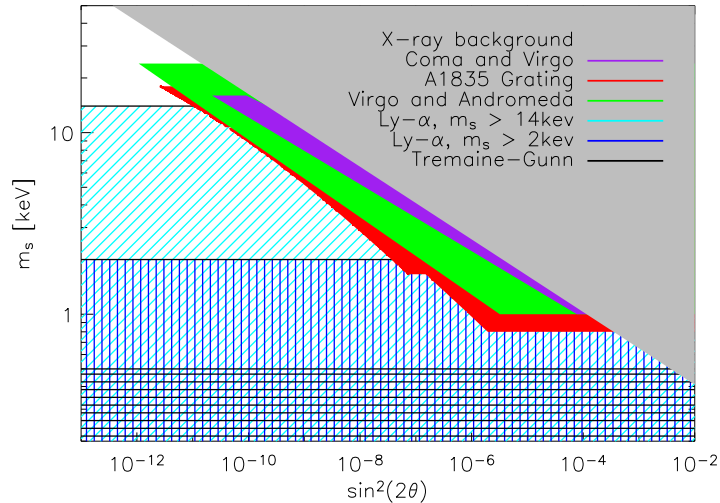


**Figure 51:** The areas excluded in the  $m - \sin^2(2\theta)$  parameter space by the Tremaine-Gunn bound (horizontal black), the Ly- $\alpha$  bound of [94] (diagonal blue), the Ly- $\alpha$  bound of [95] (diagonal cyan), the CXB (solid grey) [88], the clusters of galaxies Virgo and Coma (solid purple) [86], the galaxies of Virgo (M87) and Andromeda (solid green) [90], and the grating spectrum of A1835 (solid red).

## 12.5 Pulsar kicks and early star synthesizing

The observed peculiar velocities of pulsars, can be explained by an asymmetrical emission of sterile neutrinos, called pulsar kicks [16, 33, 97]. The region in the  $m - \sin^2(2\theta)$  parameter space allowing for pulsar kicks to be explained by the dark matter sterile neutrino of  $\nu$ MSM corresponds approximately to the region excluded by the X-ray observations of the Virgo and Andromeda galaxies and by the A1835 grating data [33, 46]. However the for the pulsar kick velocities to be explained by sterile neutrinos does not require an extension of the standard model by three sterile neutrinos, but can do with one or two. The uncertainties of the constraints taken into regard, the region allowing for pulsar kicks is not entirely excluded, but neither does the requirement of the two problems being solved by the same sterile neutrino contribute to confirm or reject the dark matter sterile neutrino.

The sterile neutrino needed to explain the synthesizing of the early star formation is the same as for the dark matter [98]. However there are disagreements on the effect of the decaying sterile neutrinos on the collapsing hydrogen clouds in the early Universe [99, 100].

## 13 Other Dark Matter Candidates

From the discussion in Sec. 12.4 we see that the parameter space left for a sterile neutrino in the simplest  $\nu$ MSM model including the entropy  $S$  is very small and the sterile neutrino is not a favoured dark matter candidate. Some of the constraints obtained in the work presented here, e. g. the decay rate, are very general and not related to the theory of sterile neutrinos, so the constraints can be transferred directly to other dark matter candidates with a radiative decay in the energy range  $E_\gamma = 0.3 - 10.0$  keV.

### 13.1 Higgs-like bosons and axions

Higgs-like bosons and axions have been speculated to be the dark matter, but so far their interactions beside gravity have not been predicted to a level, where it can be constrained experimentally. A large effort is put into the discovery of the Higgs boson at the LHC (CERN) and the results might give a hint of whether the Higgs or a Higgs-like boson is a viable dark matter candidate.

### 13.2 Super-symmetric particles

Super-symmetry is a symmetry between fermions (particles with spin 1/2) and bosons (particles with integer spin). Super-symmetric extensions of the standard model (SUSY) dictates the existence of a super-partner to every particle in the standard model (all the particles of the standard model are summarized in Fig. 5). These super-partners provides naturally a number of particles for the dark matter candidature such as: sneutrinos, axinos, gravitinos, photinos, neutralinos etc.

Probably the best SUSY candidate is the lightest of the SUSY particles which is either the neutralino or the gravitino (depending on the exact model). It is predicted to be stable electrically neutral Majorana fermion with a mass,  $m_\chi$ , in the range between some GeV and some TeV which is considerably heavier than the sterile neutrino and renders it a CDM candidate.

It is possible to constrain the neutralino with particle accelerator experiments and a lower limit  $m_\chi \gtrsim 30$  GeV was provided by LEP [101]. An indirect search for decay product effects from a decaying neutralino by several experiments seems to favour a mass below  $\approx 100$  GeV [102]. The neutralino will also have decay channels with a  $\gamma$ -ray signature, which have not yet been found.

The lightest super-symmetric particle in the simplest SUSY models are predicted to be experimentally verifiable when LHC finishes. If they are found at LHC, the work of demonstrating that they are really the dark matter still remains.

None of the proposed candidates lies in the mass range probed by X-rays, so the constraints presented in Sec. 11 does not give any helpful constraints.

## 14 Summary

The sterile neutrino, or non-weakly interacting right-handed neutrino, is a warm dark matter candidate proposed to solve the structure formation problems of the CDM scenario. It is participating in the flavour-mass eigenstate oscillations of the active standard model neutrinos, and thereby it is allowed to decay radiatively under the emission of a photon with an energy ( $E_\gamma = m_s/2$ ) predicted to lie in the X-ray range.

The radiative decay rate ( $\Gamma_\gamma$ ), the lifetime ( $\tau$ ), the mass ( $m_s$ ), the mixing angle ( $\sin^2(2\theta)$ ), and any additional entropy release after the production of the sterile neutrinos ( $S$ ) can be constrained from X-ray observations of dark matter dense regions. The *Chandra* observations of the Milky Way halo (blank sky data), the outskirts of the galaxy cluster A383, the dark matter blob in the cluster A520, and the grating observations of the cluster A1835 all have been analysed. The obtained constraints are valid for the observed photon energy range  $E_\gamma = 0.3 - 10.0$  keV.

Several steps were taken to improve the obtained results. Compared to observations of a full cluster the signal to noise ratio of a radiatively decaying dark matter particle is improved by an order of magnitude by observing only the outskirts of a cluster. By using high energy resolution data from *Chandra* grating observations, the constraints on the decay rate and lifetime was improved by a factor of  $\approx 100$  compared to previously published results from observations of entire clusters. Due to the improvement of energy resolution, the grating data provides the best of the acquired constraints even though the signal to noise ratio decreases when including the central part of the cluster in the observations.

A very conservative and robust upper limit on the mass of  $m_s \lesssim 8$  keV is obtained for all mixing angles under the assumption of absolutely no additional entropy release ( $S = 0.2$ ). This upper mass limit can be strengthened to  $m_s \lesssim 3.5$  keV by allowing for a small amount of entropy release after the sterile neutrinos have been produced ( $S \approx 1 - 2$ ) and thereby diluting their distribution.

If the sterile neutrinos are mainly produced by other processes not related to active-sterile neutrino oscillations, no constraints on the lifetime and mass can be derived from the conditions of the early Universe. The presented results of the radiative decay rate are very general and can be applied to all dark matter candidates with a two-body radiative decay photon energy in the interval  $E_\gamma = 0.3 - 10.0$  keV independently of production mechanism.

The obtained constraints were compared to several of the X-ray constraints in the  $\sin^2(2\theta) - m_s$  parameter space found in the literature. The constraints presented in this report are very conservative and are still among the best upper limit constraints on  $\sin^2(2\theta)$  for  $m_s = 0.8 - 20$  keV. The  $\sin^2(2\theta) - m_s$  parameter space can also be constrained from structure formation in the Universe by analyses of Ly- $\alpha$  and CMB data. If all constraints are combined, the only parameter space

left open is for  $m_s \gtrsim 14 \text{ keV}$ ,  $\sin^2(2\theta) \lesssim 10^{-11}$  and no additional entropy release.

No signature of the sterile neutrinos has been found, and even though “not found” is not the same as “not existing”, the combined constraints of X-ray, Ly- $\alpha$ , and CMB point towards the non-existence of a keV-mass dark matter sterile neutrino.



# A Appendix

## A.1 Abbreviations and Acronyms

Abbreviations	Explanation
Axxxx	Abell xxxx
ACIS	Advanced Charge-Coupled Device Imaging Spectrometer
arf	ancillary response file, X-ray analysis
CCD	Charge-Coupled Device
CDM	Cold Dark Matter
CERN	European Organization for Nuclear Research, Conseil Européene pour la Recherche Nucleaire, <a href="http://www.cern.ch">http://www.cern.ch</a>
CIAO	Chandra Interactive Analysis of Observations, <a href="http://cxc.harvard.edu/ciao">http://cxc.harvard.edu/ciao</a>
<i>Chandra</i>	Just a name, <a href="http://chandra.harvard.edu">http://chandra.harvard.edu</a>
CMB	Cosmic Microwave Background
CP	Charge and Parity
CXB	Cosmic X-ray Background
DM	Dark Matter
DET	DETECTED
ESA	European Space Agency <a href="http://www.esa.int">http://www.esa.int</a>
FOV	Field Of View
HDM	Hot Dark Matter
HEAO-1	High Energy Astrophysics Observatory 1, NASA
HEASARC	High Energy Astrophysics Science Archive Research Centre <a href="http://heasarc.gsfc.nasa.gov">http://heasarc.gsfc.nasa.gov</a>
HEG	High Energy Grating, <i>Chandra</i>
HETG	High Energy Transmission Grating, <i>Chandra</i>
HRC	High Resolution Camera, <i>Chandra</i>
HRMA	High Resolution Mirror Assembly, <i>Chandra</i>
ICM	Intra-Cluster Medium
IDL	Interactive Data Language
LEP	Large Electron-Positron Collider at CERN
LHC	Large Hadron Collider at CERN
Ly $\alpha$	Lyman- $\alpha$
MEKAL	Mewe-Kaastra-Liedahl model for emission from hot diffuse gas
MSM	Minimal Standard Model (of particle physics) <i>To be continued on the following page...</i>

... Continued from the previous page

<b>Abbreviations</b>	<b>Explanation</b>
NASA	National Aeronautics and Space Administration
NFW	Navarro-Frenk-White
QCD	Quantum Chromo Dynamics, strong interaction theory
rmf	redistribution matrix file, X-ray analysis
SDSS	Sloan Digital Sky Survey, <a href="http://www.sdss.org">http://www.sdss.org</a>
Sherpa	<a href="http://cxc.harvard.edu/sherpa">http://cxc.harvard.edu/sherpa</a>
SUSY	SUper SYmmetric (extension of the standard model)
WDM	Warm Dark Matter
<i>XMM</i>	X-ray Multi-Mirror, <a href="http://sci.esa.int/xmm">http://sci.esa.int/xmm</a>
Xspec	<a href="http://heasarc.nasa.gov/docs/xanadu/xspec">http://heasarc.nasa.gov/docs/xanadu/xspec</a>
$\nu$ MSM	Neutrino extension of the Minimal Standard Model

## A.2 Rewriting the Boltzmann equation

The Boltzmann equation:

$$\left( \frac{\partial}{\partial t} - pH(t) \frac{\partial}{\partial p} \right) f(p) = I_{coll}, \quad (80)$$

can be rewritten in terms of  $x = a(t)$  MeV and  $y = E \cdot a(t) = p \cdot a(t)$ . Using the notations  $f = f(x, y)$ ,  $a = a(t)$ ,  $H = \dot{a}/a = \dot{x}/x = H(t)$  the following derivatives are calculated:

$$\begin{aligned} \frac{\partial y}{\partial t} &= \frac{\partial p}{\partial t} a + \frac{\partial a}{\partial t} p = 0 + \dot{a} p, \\ \frac{\partial y}{\partial x} &= \text{MeV} \frac{\partial a}{\partial t} = \dot{a} \text{MeV}, \\ \frac{\partial y}{\partial p} &= a, \\ \frac{\partial f}{\partial p} &= \frac{\partial f}{\partial x} \frac{\partial x}{\partial p} + \frac{\partial f}{\partial y} \frac{\partial y}{\partial p} = 0 + \frac{\partial f}{\partial y} a \\ &\Leftrightarrow \\ \frac{\partial f}{\partial y} &= \frac{1}{a} \frac{\partial f}{\partial p}. \end{aligned} \quad (81)$$

The derivatives can be inserted in the left hand side of the Boltzmann equation (Eqn. 31):

$$\begin{aligned} \frac{\partial f}{\partial t} - pH \frac{\partial f}{\partial p} &= \frac{\partial f}{\partial x} \frac{\partial x}{\partial t} + \frac{\partial f}{\partial y} \frac{\partial y}{\partial t} - pH \frac{\partial f}{\partial p} \\ &= \frac{\partial f}{\partial x} \dot{x} \frac{x}{x} + \frac{\partial f}{\partial p} \frac{\dot{a}}{a} p - pH \frac{\partial f}{\partial p} \\ &= Hx \frac{\partial f}{\partial x}, \end{aligned} \quad (83)$$

Now the approximated Boltzmann equation in terms of  $x$  and  $y$  looks like [31]:

$$xH \frac{\partial}{\partial x} f = I_{coll}. \quad (84)$$

### **A.3 Sterile neutrinos in the Milky Way: Observational constraints**

A part of the work presented in this report was published in the article:

S. Riemer-Sorensen, S. H. Hansen and K. Pedersen,  
*“Sterile neutrinos in the Milky Way: Observational constraints,”*  
*Astrophys. J.* **664**, L33 (2006),  
[arXiv:astro-ph/0603661]

## References

- [1] S. Riemer-Sorensen, S. H. Hansen and K. Pedersen, *Astrophys. J.* **664**, L33 (2006), [arXiv:astro-ph/0603661].
- [2] M. Maggiore, “A Modern Introduction to Quantum Field Theory”, First Edition, Oxford University Press, 2005.
- [3] A. G. Riess *et al.* [Supernova Search Team Collaboration] 1998, *Astron. J.* **116**, 1009 (1998), [arXiv:astro-ph/9805201].
- [4] B. Ryden, “Introduction to Cosmology,” First Edition, Addison Wesley 2002.
- [5] J. Lesgourgues, Lecture notes for the Summer Students Program of CERN (2002-2005), [arXiv:astro-ph/0409426].
- [6] D. N. Spergel *et al.*, [arXiv:astro-ph/0603449].
- [7] The WMAP homepage, <http://map.gsfc.nasa.gov/index.html>.
- [8] M. Arnaud 2005, [arXiv:astro-ph/0508159].
- [9] The Coma cluster, [astrosun.tn.cornell.edu/courses/astro201/coma.htm](http://astrosun.tn.cornell.edu/courses/astro201/coma.htm).
- [10] B. Moore, S. Ghigna, F. Governato, G. Lake, T. Quinn, J. Stadel and P. Tozzi, *ApJ*, 524, L19, [arXiv:astro-ph/9907411].
- [11] P. Bode, J. P. Ostriker and N. Turok, *Astrophys. J.* **556**, 93 (2001), [arXiv:astro-ph/0010389].
- [12] R. A. Swaters, B. F. Madore, F. C. V. Bosch and M. Balcells, *Astrophys. J.* **583**, 732 (2003), [arXiv:astro-ph/0210152].
- [13] The Hubble Space Telescope web page, <http://hubblesite.org>.
- [14] S. Dodelson and L. M. Widrow, *Phys. Rev. Lett.* **72**, 17 (1994), [arXiv:hep-ph/9303287].
- [15] A. Kusenko and G. Segre, *Phys. Lett. B* **396**, 197 (1997), [arXiv:hep-ph/9701311].
- [16] G. M. Fuller, A. Kusenko, I. Mocioiu and S. Pascoli, *Phys. Rev. D* **68**, 103002 (2003), [arXiv:astro-ph/0307267].

- [17] P. L. Biermann and A. Kusenko, Phys. Rev. Lett. **96**, 091301 (2006), [arXiv:astro-ph/0601004].
- [18] T. Asaka and M. Shaposhnikov, Phys. Lett. B **620**, 17 (2005), [arXiv:hep-ph/0505013].
- [19] Particle Data Group, “Particle Physics Booklet, 2004”, <http://pdg.lbl.gov>
- [20] Particle Adventures, <http://www.particleadventure.org>.
- [21] F. Halzen and A. D. Martin, “Quarks and Leptons - An Introductory Course in Modern Particle Physics”, Second Edition, John Wiley & Sons, 1984.
- [22] J. Lesgourgues and S. Pastor 2006, [arXiv:astro-ph/0603494].
- [23] CERNs homepage, <http://cern.ch>.
- [24] T. Asaka, S. Blanchet and M. Shaposhnikov, Phys. Lett. B **631**, 151 (2005), [arXiv:hep-ph/0503065].
- [25] T. Asaka, A. Kusenko and M. Shaposhnikov 2006, [arXiv:hep-ph/0602150].
- [26] M. Shaposhnikov and I. Tkachev 2006, [arXiv:hep-ph/0604236].
- [27] M. Shaposhnikov, [arXiv:hep-ph/0605047].
- [28] T. Asaka, M. Laine and M. Shaposhnikov, [arXiv:hep-ph/0605209].
- [29] B. Kayser 2001, [arXiv:hep-ph/0104147].
- [30] V. D. Barger, R. J. N. Phillips and S. Sarkar 1995, Phys. Lett. B **352**, 365 (1995), [Erratum-ibid. B **356**, 617 (1995)], [arXiv:hep-ph/9503295].
- [31] A. D. Dolgov, S. H. Hansen, G. Raffelt and D. V. Semikoz 2000, Nucl. Phys. B590, 562, [arXiv:hep-ph/0008138].
- [32] P. B. Pal and L. Wolfenstein, Phys. Rev. D **25**, 766 (1982).
- [33] A. Kusenko, Int. J. Mod. Phys. D **13**, 2065 (2004), [arXiv:astro-ph/0409521].
- [34] D. W. Sciama, MNRAS, 198, 1P, 1982.
- [35] The Chandra Proposers’ Observatory Guide, ver. 8.0, Dec. 2005, <http://cxc.harvard.edu/proposer/POG/html/>.

- [36] C. Kittel and H. Kroemer, “Thermal Physics”, Second Edition, W. H. Freeman and Company, 2002.
- [37] L. Bergström and A. Goobar, “Cosmology and Particle Astrophysics”, Second Edition, Springer 2003.
- [38] E. W. Kolb and M. S. Turner, “The Early Universe”, Second Edition, Addison Wesley, 1990.
- [39] C. Nygaard, H. H. Dalsgaard and S. Riemer-Sørensen, “High  $p_T$  Suppression In Ultrarelativistic Heavy Ion Collisions”, bachelor project, University of Copenhagen, 2004.
- [40] K. Abazajian, Phys. Rev. D **73**, 063506 (2006), [arXiv:astro-ph/0511630].
- [41] A. D. Dolgov and S. H. Hansen 2002 Astropart. Phys., 16, 339, [arXiv:hep-ph/0009083].
- [42] F. W. Stecker, Phys. Rev. Lett. **45**, 1460 (1980).
- [43] R. Kimble, S. Bowyer and P. Jakobsen, Phys. Rev. Lett. **46**, 80 (1981).
- [44] M. R. Spiegel and J. Liu, “Mathematical Handbook of Formulas and Tables”, Second Edition, Schaum’s Outline Series, 1999.
- [45] A. D. Dolgov 2002, Phys. Rept. 370, 333, [arXiv:hep-ph/0202122].
- [46] K. Abazajian and S. M. Koushiappas, [arXiv:astro-ph/0605271].
- [47] X. D. Shi and G. M. Fuller, Phys. Rev. Lett. **82**, 2832 (1999), [arXiv:astro-ph/9810076].
- [48] T. Asaka et al, 2006, in preparation.
- [49] D. Semikoz et al. 2006, in preparation
- [50] K. N. Abazajian and G. M. Fuller, Phys. Rev. D **66**, 023526 (2002), [arXiv:astro-ph/0204293].
- [51] The *XMM* Users Hand Book, [http://xmm.vilspa.esa.es/external/xmm\\_user\\_support/documentation/uhb/index.html](http://xmm.vilspa.esa.es/external/xmm_user_support/documentation/uhb/index.html).
- [52] The *Chandra* web page, <http://chandra.harvard.edu/>.
- [53] G. P. Smith, J. P. Kneib, H. Ebeling, O. Czoske and I. Smail 2000, [arXiv:astro-ph/0008315].

- [54] Jesper Rasmussens PhD Thesis, <http://www.astro.ku.dk/~jr/publ/thesis.pdf>.
- [55] The CIAO webpage, <http://cxc.harvard.edu/ciao/>. For this work CIAO version 3.3.0.1 has been used with CALDB version 3.2.2.
- [56] The *Chandra* grating web page, [http://space.mit.edu/CSR/hetg\\_info.html](http://space.mit.edu/CSR/hetg_info.html).
- [57] CIAO thread “Grouping a Grating Spectrum”, [http://cxc.harvard.edu/ciao/threads/spectra\\_grouping/](http://cxc.harvard.edu/ciao/threads/spectra_grouping/).
- [58] HEASARC data archive, <http://heasarc.gsfc.nasa.gov/docs/archive.html>.
- [59] Jesper Rasmussens webpage on *Chandra* data analysis, <http://www.astro.ku.dk/~jr/chandra>
- [60] The S-Lang Library Information Page, <http://www.s-lang.org>.
- [61] P. E. Freeman, S. Doe, A. Siemiginowska 2001, SPIE Proceedings, Vol. 4477, p.76, 2001, <http://cxc.harvard.edu/sherpa>.
- [62] The Tcl Developer Xchange, <http://www.tcl.tk>.
- [63] K. A. Arnaud 1996, XSPEC version 12.2.1, Astronomical Data Analysis Software and Systems V, ASP Conf. Series volume 101.
- [64] Maxim Markevitchs archive of blank sky data, <http://cxc.harvard.edu/contrib/maxim>.
- [65] The Canada-France-Hawaii Telescope, <http://www.cfht.hawaii.edu/Science/Astros/Imageofweek/ciw280800.html>, image courtesy of J.P. Kneib & O. Czoske.
- [66] A. Vikhlinin, A. Kravtsov, W. Forman, C. Jones, M. Markevitch, S. S. Murray and L. Van Speybroeck 2005, *Astrophys. J.* **640**, 691 (2006), [arXiv:astro-ph/0507092].
- [67] A. Klypin, H. Zhao and R. S. Somerville, *ApJ*, 573, 597, [arXiv:astro-ph/0110390].
- [68] S. Tremaine and J. E. Gunn, *Phys. Rev. Lett.* **42**, 407 (1979),
- [69] A. Boyarsky, A. Neronov, O. Ruchayskiy, M. Shaposhnikov and I. Tkachev, [arXiv:astro-ph/0603660].

- [70] NASA Sky View, <http://skys.gsfc.nasa.gov/cgi-bin/titlepage.pl>.
- [71] H. Ebeling *et al.*, MNRAS, 301, 881 (1998), [arXiv:astro-ph/9812394].
- [72] Maxim Markevitch talk at the workshop SNAC 06 in Crans-Montana, Switzerland, march 2006.
- [73] R. W. Schmidt, S. W. Allen and A. C. Fabian, Mon. Not. Roy. Astron. Soc. **327**, 1057 (2001), [arXiv:astro-ph/0107311].
- [74] L. M. Voigt and A. C. Fabian 2006, [arXiv:astro-ph/0602373].
- [75] C. L. Sarazin, “X-ray Emission from Clusters of Galaxies,” Cambridge University Press 1988, at the time of writing available at: <http://nedwww.ipac.caltech.edu/level5/March02/Sarazin/frames.html>
- [76] M. Fukugita, C. J. Hogan and P. J. E. Peebles 1998, Astrophys. J. **503**, 518 (1998), [arXiv:astro-ph/9712020].
- [77] I. R. King 1972, Astrophys. J. **174**, L123 (1972).
- [78] J. Binney and M. Merrifield, “Galactic astronomy,” First Edition, Princeton University Press, 1998.
- [79] S. W. Allen, 1998, MNRAS, 296, 392, [arXiv:astro-ph/9710217].
- [80] H. Karttunen, P. Kröger, H. Oja, M. Poutanen, and K. J. Donner, “Fundamental Astronomy,” Third Revised and Enlarged Edition, Springer 2000.
- [81] E. Rasia *et al.* 2006, [arXiv:astro-ph/0602434].
- [82] H. Dahle, N. Kaiser, J. R. Irgens, P. B. Lilje, S. J. Maddox 2002, Astrophys. J. Supplement **139**, 313-368 (2002).
- [83] Private communication with Håkon Dahle, Institute of Theoretical Astrophysics, University of Oslo, [hdahle@astro.uio.no](mailto:hdahle@astro.uio.no). The used method is described in H. Dahle (2000), [astro-ph/0009393].
- [84] The Cosmological Calculator, [http://www.astro.ku.dk/avo/ccc/ccc\\_v2\\_frameset.html](http://www.astro.ku.dk/avo/ccc/ccc_v2_frameset.html).
- [85] R. Mewe, E. H. B. M. Gronenschild, G. H. J. van der Oord, 1985, A&As, 62, 197.
- [86] A. Boyarsky, A. Neronov, O. Ruchayskiy and M. Shaposhnikov 2006a, [arXiv:astro-ph/0603368].

- [87] D. N. C. Lin and S. M. Faber, *Astrophys. J.* **266**, L21 (1983).
- [88] A. Boyarsky, A. Neronov, O. Ruchayskiy and M. Shaposhnikov, [arXiv:astro-ph/0512509].
- [89] K. Abazajian, G. M. Fuller and W. H. Tucker, *Astrophys. J.* **562**, 593 (2001), [arXiv:astro-ph/0106002].
- [90] C. R. Watson, J. F. Beacom, H. Yuksel and T. P. Walker, [arXiv:astro-ph/0605424].
- [91] K. Abazajian, *Phys. Rev. D* **73**, 063513 (2006), [arXiv:astro-ph/0512631].
- [92] J. Cohns webpage on theoretical cosmology, <http://astro.berkeley.edu/~jcohn/tcosmo.html>.
- [93] V. K. Narayanan, D. N. Spergel, R. Dave and C. P. Ma, [arXiv:astro-ph/0005095].
- [94] M. Viel, J. Lesgourgues, M. G. Haehnelt, S. Matarrese and A. Riotto, *Phys. Rev. D* **71**, 063534 (2005), [arXiv:astro-ph/0501562].
- [95] U. Seljak, A. Makarov, P. McDonald and H. Trac, [arXiv:astro-ph/0602430].
- [96] M. Viel, J. Lesgourgues, M. G. Haehnelt, S. Matarrese and A. Riotto, [arXiv:astro-ph/0605706].
- [97] A. Kusenko and G. Segre, *Phys. Rev. D* **59**, 061302 (1999), [arXiv:astro-ph/9811144].
- [98] J. Stasielak, P. L. Biermann and A. Kusenko, [arXiv:astro-ph/0606435].
- [99] E. Ripamonti, M. Mapelli and A. Ferrara, [arXiv:astro-ph/0606483].
- [100] E. Ripamonti, M. Mapelli and A. Ferrara, [arXiv:astro-ph/0606482].
- [101] J. A. De Freitas Pacheco and S. Peirani, *Grav. Cosmol.* **11**, 169 (2005) [arXiv:astro-ph/0503380].
- [102] F. Donato, N. Fornengo, D. Maurin and P. Salati, *Phys. Rev. D* **69**, 063501 (2004) [arXiv:astro-ph/0306207].